

### Analytical and Numerical Aspects of Tomography

by

Dimitra Kyriakopoulou MSc

A thesis submitted in conformity with the requirements

for the degree of Doctor of Philosophy

Department of Mathematics

Faculty of Mathematical & Physical Sciences

University College London

I, Author Name, confirm that the work presented in this thesis is my own. Where information has been derived from other sources, I confirm that this has been indicated in the work.

### **Abstract**

The Boundary Control (BC) Method was originally formulated with respect to hyperbolic inverse problems. We extend this powerful method to elliptic and parabolic problems. In particular, by considering Boundary Value Problems as edge problems, we extend the functional analytic version of BC from commutative C\* algebras to noncommutative ones, through the use of a suitably chosen pseudodifferential calculus for singular manifolds. We then apply this extended BC to the open Calderón conjecture, presenting a multitude of cases where the uniqueness argument holds. Via the pseudodifferential calculus extension to higher singularities by an iteration process, the extended BC is applied to the reconstruction of a Riemannian polyhedron. We also showed that for the standard (hyperbolic) BC the interface and corner detection of a Riemannian polyhedron can be achieved by introducing appropriate notions from physics (e.g. waveguides and 4-wave-mixing).

For Electrical Impedance Tomography, i.e., for the 2D case of the Calderón problem, a novel algorithm is constructed that is simpler and faster compared to the well-known D-bar method, which is based on Complex Geometric Optics solutions.

The following algorithms are implemented in the tomographic, extensively used library, Software for Tomographic Image Reconstruction (STIR): two 2D Positron Emission Tomography (PET), two 2D Single Photon Emission Computed Tomography (SPECT), and one 3D PET. These algorithms serve as templates for how to include in the library analytic reconstruction algorithms, without the need to extensively study the library. The PET algorithms constitute strong alternatives to STIR's existing filtered back-projection PET algorithms in terms of image quality and/or speed, while the SPECT algorithms are the first of their kind within the

Abstract 4

library.

## **Impact Statement**

This thesis focuses on analytical and numerical aspects of tomography. In particular, it advances the understanding of aspects of the solution of the Calderón problem, and introduces practical improvements in medical imaging through algorithmic development and contributions to widely-used software.

An important contribution is the delineation of the path towards the unification of inverse boundary value problems (IBVPs). This is achieved by extending the applicability of the BC Method beyond hyperbolic problems to elliptic and parabolic ones. Unifying the BC Method will have important implications in several fields, including physics, engineering, and importantly in medical imaging where inverse BVPs play a critical role.

The extended BC Method is applied to the Calderón problem, a central inverse problem that has been under study for more than 40 years. In particular, it proves uniqueness for several specific cases. These results are directly relevant to electrical impedance tomography (EIT), since the 2D Calderón problem provides the mathematical foundation of EIT.

In addition to its focus on tomography, the thesis also applies the extended BC Method to the reconstruction of Riemannian polyhedra. This work broadens the range of problems that can be addressed applying the extended BC method, namely, it includes geometries with higher singularities. Importantly, in this work concepts from physics are incorporated into the standard hyperbolic BC problem-solving. This interdisciplinary approach, by showing how physical ideas can be integrated into mathematical frameworks, opens the way to potential applications in areas such as non-destructive testing and underwater fiber optics, where the detection and

manipulation of wave patterns is critical.

This thesis also introduces a novel algorithm for 2D EIT. This algorithm appears to be faster and simpler than the widely used D-bar method. The enhanced speed of this algorithm makes it well-suited for real-time applications in clinical settings, where quick and accurate imaging is essential.

Further practical contributions of this research include the implementation of five tomographic algorithms in the Software for Tomographic Image Reconstruction (STIR) library. STIR is widely recognized and used in the medical imaging community. Thus, the inclusion of two algorithms for 2D Positron Emission Tomography (PET), two algorithms for 2D Single Photon Emission Computed Tomography (SPECT), and one algorithms for 3D PET algorithm improves the library's capabilities. Some of these new algorithms offer better image quality and faster processing times compared to existing methods. Importantly, they also serve as a clear template for including analytic reconstruction algorithms in the library, helping to advance the library's ongoing contributions to medical imaging. STIR's importance, underscored by its 2017 Rotblat Prize by *Physics in Medicine & Biology* (PMB), suggests that these additions will be valuable for both researchers and clinicians working with tomographic imaging.

In summary, this thesis involves high level mathematical work of direct practical significance. In particular, it has the potential to impact a range of fields, from tomography to non-destructive testing and fiber optics.

# Acknowledgements

Professor Yaroslav Kurylev's presence permeates the thesis, even though he did not directly participate in the results presented here. It's not only his transformative contributions to the Boundary Control (BC) method (he is the founder of its geometric version and dedicated much of his life to researching it). But also, his courageous decision to add a geometric dimension to the BC method provides an important example of extending the frameworks within which BC can be studied. This was the inspiration for the thesis's exploration of BC in the context of pseudodifferential operators (PDOs) (combining analytic, geometric, and algebraic approaches).

Although not physically present, Professor Kurylev, a genuinely good and virtuous person, is always with me, serving as the voice of my mathematical conscience. He provides a constant source of motivation, inspiring me to improve, so that I can connect with him on a transcendent level.

The thesis's first supervisor, Professor Athanassios S. Fokas, is a historic figure in mathematics; among his many contributions, the *Fokas method*, succeeds in bringing to differential operators the advantages typically associated with pseudodifferential operators (incorporating global information into local manipulations). Professor Fokas is a virtuous person who uses his power to help others. His intellectual pursuits are motivated by a desire to contribute to improving the human condition through two key aims: advancing science and raising human consciousness to higher levels by enhancing the creative and spiritual aspect of human nature. As a result, the full impact of being supervised by Professor Fokas cannot be fully captured in this thesis. The evolution of mathematical thoughts he has generated in me will continue to unfold and, hopefully, become evident in future works. Professor

Fokas is, and will always be, both an inspiration and a driving force for my growth as a person and a mathematician.

The thesis's second supervisor, Professor Kris Thielemans, a world- renowned computer scientist, is the maintainer of the well-known tomographic reconstruction library STIR. Professor Thielemans exemplifies both extraordinary programming expertise and genuine kindness. The STIR-related work in the thesis reflects not only the invaluable knowledge he imparted on me, but also the encouragement I felt through his patient guidance, overlooking the fact I was not a programmer. Being supervised by Professor Thielemans will have a lasting impact on me: his kindness will be a source of strength, his expertise has deepened my understanding of the STIR library's potential as a crucial tool for tomographic research, and his influence will inspire me not to shy away from programming aspects of mathematical projects, despite the challenges they may pose to me as a mathematician.

Professor Matti Lassas gave me the opportunity to become a visiting researcher at the University of Helsinki. There, I experienced the critical influence of the Finnish Inverse Problems Society, which places great value on kindness, integrity, collaboration, and free thinking. My stay in Finland was a decisively impactful educational experience, and also provided me with the opportunity to meet individuals who are both nice persons and powerful scientists. I would like to thank especially, Professor Matti Lassas, Professor Gunther Uhlmann, Professor Lauri Oksanen, and Professor Mikko Salo.

I will do everything in my power to be a virtuous person and a dedicated mathematician, so that in the long run, I may prove myself a worthy recipient of the kindness and guidance I have received from my teachers.

Finally, I am deeply grateful to my parents and my brother for their tremendous support.



# **Contents**

1	Intr	oductor	ry Material	15
2 Extension o			of Boundary Control method to elliptic and parabolic prob	-
	lems	s, and it	s application to the Calderon problem	20
	2.1	Introd	uction	20
	2.2	Quick	Overview on Pseudodifferential Operators on Manifolds with	
		Edges		24
	2.3	Proofs	on BC method extensions	32
		2.3.1	Proof on BC for elliptic problems	32
		2.3.2	Proof on BC for parabolic problems	46
	2.4	The Ca	alderon Problem	47
		2.4.1	Proof of Theorem 2.1.3	47
3	Poly	hedral	reconstruction via Boundary Control method	55
	3.1	Introd	uction	55
	3.2	Recon	struction of an Elliptic Riemannian Polyhedron	57
		3.2.1	Algebra description	57
		3.2.2	Proof of Theorem 3.1.1	59
	3.3 Interface and vertex detection conditions for Polyhedron		ce and vertex detection conditions for Polyhedron	60
		3.3.1	Prerequisite facts	60
		3.3.2	Electromagnetic waves in isotropic dielectric media	61
		3.3.3	Electromagnetic waves in anisotropic non-linear media	66
		3.3.4	Acoustic waves in fluid media	67

4	Elec	trical i	mpedance tomography revisited	<b>7</b> 0	
	4.1	A sim	ple re-derivation of the basic equations of EIT	71	
	4.2	Using	the equation for $u_z$	73	
	4.3	Direct	Constraints	75	
	4.4	$\Omega$ arbi	trary bounded domain, i.e. not restricted to unit disk	76	
	4.5	Appen	dices	78	
		4.5.1	Appendix I (verification of (4.22))	78	
		4.5.2	Appendix II (verification of (4.30))	78	
		4.5.3	Appendix III (Verification of (4.31))	80	
		4.5.4	Appendix IV (Verification of (4.33))	80	
5	Imp	lement	ation of two 2D PET analytic reconstruction algorithms in	l	
	STI	R and t	heir performance evaluation	82	
	5.1	Prereq	uisites	83	
		5.1.1	2D Geometry	83	
		5.1.2	Direct Fourier Method	84	
	5.2	2D Gr	idding algorithm (GRD2D)	85	
		5.2.1	Implementation details of <i>Step 2</i>	89	
		5.2.2	Further notes on (STIR) implementation	89	
	5.3	Spline	Reconstruction Technique (SRT2D) algorithm	90	
		5.3.1	Mathematical formulation and algorithm steps	90	
		5.3.2	Symmetries	92	
		5.3.3	STIR implementation improvements	95	
	5.4	Comp	arison of algorithms	99	
		5.4.1	Phantom and data creation	99	
		5.4.2	Image Quality Metrics	99	
		5.4.3	Computational complexity	104	
6	Implementation of two 2D SPECT analytic reconstruction algorithms in				
	STI	R and t	heir performance evaluation	105	
	6.1	Prereq	uisites	106	

Contents	11
Contents	11

		6.1.1	Formulation of the problem 106	
		6.1.2	SPECT scanner description and assumptions 107	
	6.2	Kunya	nsky's SPECT Algorithm (KSA2D)	
		6.2.1	Mathematical formulation of the reconstruction formula 107	
		6.2.2	The algorithm steps and a few implementation comments 108	
		6.2.3	Notes on STIR implementation	
	6.3	Spline	Reconstruction Technique (SRT2DSPECT)	
		6.3.1	Mathematical formulation and algorithm steps of SRT2DSPECT111	
		6.3.2	Speeding up techniques, filtering, and further aspects of the	
			STIR implementation	
	6.4	Compa	arison of algorithms	
		6.4.1	Phantom and creation of data	
		6.4.2	Image Quality Metrics	
		6.4.3	Computational Complexity	
_	Imn	lomonto	ation of a 3D PET analytic reconstruction algorithm in STIR	
7				
7	_		·	
7	and	its perf	formance evaluation 123	
7	_	its perf	·	
7	and	its perf	formance evaluation 123	
7	and	<b>its perf</b> Prereq	formance evaluation 123 uisites	
7	and	its perf Prereq 7.1.1 7.1.2	tormance evaluation 123 uisites	
7	<b>and</b> 7.1	Prereq 7.1.1 7.1.2 3D Dir	tormance evaluation 123 uisites	
7	<b>and</b> 7.1	Prereq 7.1.1 7.1.2 3D Dir	tormance evaluation 123 uisites	
7	<b>and</b> 7.1	its perf Prereq 7.1.1 7.1.2 3D Dir 7.2.1 7.2.2	tormance evaluation 123 uisites	
7	and 7.1 7.2	its perf Prereq 7.1.1 7.1.2 3D Dir 7.2.1 7.2.2	tormance evaluation 123  uisites	
7	and 7.1 7.2	its perf Prereq 7.1.1 7.1.2 3D Dir 7.2.1 7.2.2 3D Dir	tormance evaluation 123  uisites	
7	and 7.1 7.2	its perf Prereq 7.1.1 7.1.2 3D Dir 7.2.1 7.2.2 3D Dir 7.3.1	tormance evaluation 123  uisites	
7	and 7.1 7.2	its perf Prereq 7.1.1 7.1.2 3D Din 7.2.1 7.2.2 3D Din 7.3.1 7.3.2 7.3.3	tuisites	
7	and 7.1 7.2 7.3	its perf Prereq 7.1.1 7.1.2 3D Din 7.2.1 7.2.2 3D Din 7.3.1 7.3.2 7.3.3	tuisites	
7	and 7.1 7.2 7.3	its perf Prereq 7.1.1 7.1.2 3D Dir 7.2.1 7.2.2 3D Dir 7.3.1 7.3.2 7.3.3 'Artific	puisites	

	Contents	12
7.5.1	Phantom and data creation	142
7.5.2	Image Quality Metrics	143
7.5.3	Complexity of DFM3D versus FBP3DRP	144
Bibliography		146

# **List of Figures**

5.1	o regular grid, * samples provided by projection slice theorem 85
5.2	Symmetries
5.3	Zoom
5.4	Hoffmann brain phantom
5.5	Reconstructed images of FBP2D, GRD2D, and SRT2D with a 0.1
	Poisson noise scaling factor
6.1	Hilbert transform of sinc(x): precise value vs. numerical value with
	Marple's method (which we use) vs. Kunyansky's method 109
6.2	Symmetries
6.3	XCAT cardiac phantom
6.4	Reconstructed images of KSA2D, OSSPS, and SRT2DSPECT with
	a 0.01 Poisson noise scaling factor
7.1	Standard (grey) and rotated coordinate systems
7.2	LORs (in red) for $\theta = \theta_1$ , $\alpha = -0.5$ , $\phi = 0$ and various tangential
	positions, xz-axis in blue
7.3	dashed line: segment 0 ( $\theta = 0$ ), solid line: segment -2 ( $\theta > 0$ ) 131
7.4	The figure on the left depicts the samples provided by the Projection-
	slice theorem, and the one on the right the uniform grid upon which
	the samples must be interpolated
7.5	LORs for segment 2, solid line: measured, dashed line: missing 137
7.6	No missing data case
7.7	Artificial vs. real scanner

	List of Figures	14
7.8	Brainweb brain phantom	142
7.9	Reconstructed images of DFM3D and FBP3DRP with a 0.1 Poisson	
	noise scaling factor	143

### Chapter 1

# **Introductory Material**

The thesis comprises six Chapters on the analytical and numerical aspects of tomography.

In Chapter 2 we work on the Boundary Control (BC) method, which uses boundary measurements to reconstruct a domain's internal structure. It analyzes how boundary controls, like signals, propagate within the domain, establishing a relationship between inputs and outputs that encodes system information. A key step is coordinatization, where internal points are assigned coordinates based on boundary-induced signals, effectively "coding" the domain. This data is then used to construct a model that replicates the original system, allowing the domain to be reconstructed and solving the inverse problem by converting boundary measurements into an accurate internal representation. For different types of hyperbolic problems, BC method uses distinct coordinatization techniques, each tailored to the nature of the problem at hand. For example, hyperbolic inverse problems such as those on graphs employ Dirac measures, where a pointwise, highly analytic approach is suitable [1]. For more geometrically focused problems, like those on Riemannian manifolds in acoustic or electrodynamic systems, semigeodesic coordinates are used, relying on the travel times of waves through geodesics [2], [3], [4]. In dynamical inverse problems, often found in geophysical applications, the boundary distance function is utilized, focusing on the geometric relationship between boundary points and internal distances [5], [6]. In more complex hyperbolic systems like elasticity or electrodynamics, wave nests are used to capture intricate wave behaviors through a combination of geometric and operator-theoretic techniques [7], [8]. Although BC has been applied to the "hyperbolization" of the Calderon problem by the transformation of the conductivity equation to the Schrödinger equation [9], [10], the most direct application of BC to elliptic problems, which I am aware of, is for the 2D Laplace-Beltrami operator; there, coordinatization is determined by the spectrum of an algebra of states, which is analytic and algebraic in nature [11].

Hence the different methods of BC coordinatization exhibit analytic, geometric, and sometimes algebraic characteristics. Aiming at a more unified approach, pseudodifferential operators (PDOs) immediately come to mind, as they inherently merge these three aspects—analytic, geometric, and algebraic—by their very nature. PDOs provide a framework that can capture both local analytic properties and the global geometric structure of a problem in an algebraic framework. This suggests that the spectrum of a PDO could serve as a universal method of coordinatization, potentially unifying these various approaches. By doing so, the need for distinct techniques tailored to specific types of problems could be reduced, as the PDO-based approach could, in theory, apply to a broad range of systems, bridging the gap between analytic and geometric methods. To work on BC with PDOs, we reduce inverse boundary value problem (IBVP) to pseudodifferential edge problems; then the PDO algebra's principal symbols naturally comprise of interior and edge symbols. This decomposition allows for direct isometric isomorphisms between them. Consequently, the PDOs provide a natural connection between the function spaces and the geometry of the manifold, ensuring density and compatibility between the algebraic structures and geometric configurations.

Historically, one of the challenges in applying the BC method to elliptic problems has been the tendency to "hyperbolize" these problems introducing extra complexity. In particular, given that elliptic problems, unlike hyperbolic ones, do not require time-reversal techniques, BC finds a more natural and direct application to elliptic problems through PDOs, where the need for time-reverse engineering is eliminated. Building on this, we explore the extension of the BC method to parabolic problems, which can often be reduced to elliptic problems. By viewing BC through

the framework of PDOs, it becomes apparent that this approach has the potential to serve as a unifying method for inverse boundary value problems across hyperbolic, elliptic, and parabolic types. In this light, further study of the PDO-based version of BC is necessary to understand the full extent to which it can unify these methods. Finally, when applying these insights to the Calderón problem, we uncover a broad range of spaces in which the uniqueness argument holds. This result underlines that, as the information encoded within a PDO is significantly enhanced, providing not only information about the function spaces but also about the underlying manifolds themselves, BC through PDOs is a powerful and flexibile tool for solving inverse boundary value problems across diverse spaces and systems.

In Chapter 3, we build on the methodology from Chapter 2 and apply it to a more complex class of problems involving manifolds with higher singularities, i.e. not just edge problems, specifically focusing on the reconstruction of a Riemannian polyhedron. For the hyperbolic case, we demonstrate how physical principles can provide us with criteria for the detection of interfaces and vertices, allowing us to use the standard hyperbolic Boundary Control (BC) method handling each compartment independently and proceeding in an iterative fashion. In particular, for the case of electromagnetic waves we observe that there exists an analogue to Snell's Law, for perpendicular incidence, which is what we need as we work with geodesics. We use this to form an edge detection criterion, and further combining it with waveguide theory, a vertex detection criterion. Additionally, in the context of the Z-scan technique, we introduce a criterion for detecting lattice points using a four-wave solution. For the case of acoustic waves, we extend the analysis further, using reflection and transmission coefficients to detect interfaces. The identification of corners in this scenario relies on acoustic waveguides and directional couplers, similar to their electromagnetic counterparts. By applying the principles of wave propagation and coupling, we can create a unified approach that encompasses both electromagnetic and acoustic waves, providing a comprehensive framework for detecting singularities and reconstructing polyhedra in various physical settings.

In Chapter 4, a novel algorithm is developed for 2D Electrical Impedance To-

mography (EIT), providing a computationally efficient alternative to the well-known D-bar method using Complex Geometric Optics (CGO) solutions. Both algorithms rely on the transformation of the conductivity equation to the Schrödinger equation and are inspired by inverse scattering theory. However, the existing algorithm using CGO solutions introduces complex frequencies and essentially 'hyperbolizes' the problem, i.e. mimics aspects of hyperbolic problems, which is a hallmark of CGO solutions and leads to additional computational complexity. In contrast, the novel algorithm retains the elliptic nature of the problem, resulting in a simpler, more direct and computationally efficient approach. Additionally, the novel algorithm is designed for arbitrary domains, whereas the CGO-based algorithm can theoretically be extended to more complex domains, but practically it is best suited for circular or simply connected domains due to the reliance on symmetry and the Fourier-based approach. We are in the process of completing our numerical implementation.

Chapters 5 to 7 contain the implementations in STIR of two 2D Positron Emission Tomography (PET) algorithms, two 2D Single Photon Emission Computed Tomography (SPECT) algorithms, and one 3D PET algorithm, respectively. These implementations serve as templates for how to include analytic reconstruction algorithms in the library without requiring an extensive study of the library itself. This is particularly evident in the case of the "artificial scanner" used to handle missing data in the 3D implementation; STIR's equivalent process is limited to use with Filtered Backprojection (FBP) because its forward projection process relies on the symmetries specific to FBP. The artificial scanner works for standard fully 3D sinograms, i.e., with unit differences in axial positions for consecutive segments (increasing up to the middle segment and decreasing afterward), and also for sinograms where there is a jump in the axial positions in the middle segment. While these types of data are created by STIR, if the artificial scanner is extended to non-full sinograms, it could potentially be implemented as a separate class in STIR.

The first implementation of 2D PET in STIR was part of my master's thesis, which also included identifying relevant symmetries of the algorithm. However, now an enhanced version of the code is produced with new features, and also up-

dated to be compatible with the current version of STIR. The code files for all five algorithms can be found in my Github account: [https://git2hub.com/Dimitra-Kyriakopoulou](https://git2hub.com/Dimitra-Kyriakopoulou). It includes two repositories: SRT2D (public) and REP (private); the former has been forked from STIR's repository, while the latter is a clone of STIR. For SRT2D repository, which contains the implementation for SRT 2D PET and SPECT, a pull request (https://github.com/UCL/STIR/pull/1420) was submitted, and 9 out of 9 tests were successful (Pre-commit check, Codacy Static Code Analysis, Continuous Integration (CI) via Appveyor, and the 6 subtests of Build and ctest and recon\_test\_pack CI), as visible when logged into Github. The REP repository will be made public, and a pull request will be submitted once the test processes are complete. So far, 8 out of 9 tests have been successful. We are currently working on changes needed to pass the macOS-latest-gcc11-cuda0-Debug-pp=OFF-ROOT=OFF subtest in Build and ctest and recon\_test\_pack CI.

### **Chapter 2**

# Extension of Boundary Control method to elliptic and parabolic problems, and its application to the Calderon problem

We show that Boundary Control method, a method for hyperbolic inverse problems, is also capable of dealing directly with certain classes of elliptic and parabolic Inverse Boundary Value Problems; thus pointing towards Boundary Control method potentially constituting a means of unification of Inverse Boundary Value Problems. As an application we show that the Calderon problem can be dealt with directly via Boundary Control method, i.e. without reduction of the elliptic problem to a 'hyperbolized' problem.

### 2.1 Introduction

Manifolds with smooth boundary form a subcategory of manifolds with edge [12]. Hence, Bernard Wolfgang Schulze studied elliptic Boundary Value Problems (BVPs) of Shapiro– Lopatinskii (SL) type ([13],[14],[15],[16]) in the framework of Boutet de Monvel's algebra of BVPs with the transmission property at the boundary [17]. Ellipticity refers to an analogue of Shapiro– Lopatinskii conditions, i.e., a bijectivity condition for an operator-valued principal symbol structure which contains also trace

and potential operators with respect to the edge, a substitute of the former boundary. Later Schulze [12] created the Toeplitz analogue algebra of BVPs unifying conditions of SL- and global projection (GP)- elliptic type (especially APS-conditions in the sense of Atiyah, Patodi, and Singer -[18], [19], [20]); ellipticity in this context is equivalent with the Fredholm properties in the respective scales of spaces (standard Sobolev spaces in the SL case, spaces of Hardy type in the GP case).

Reducing inverse elliptic and parabolic BVPs to edge problems, we will study how Boundary Control (BC) method can be applied to them. BC method, originating from M. G. Krein's work on 1-dimensional inverse scattering theory ([21], [22]), contrasts with Gel'fand-Levitan and Marchenko's fundamental methods through its utilization of the wave equation's finite propagation speed. Krein's approach, while initially not evident due to its frequency domain formulation, was later clarified by Blagovestchenskii's time-domain analysis, highlighting its hyperbolic nature through a Volterra-type equation for unknown functions ([23]). This advancement was essential for the method's multi-dimensional extension by Belishev [24], with its geometric aspects further detailed by Belishev and Kurylev [25], also noted in [26]. Additionally, the BC method's capability to assess the inner product of boundary-induced waves, traced back to Blagovestchenskii ([27]), was extended to multidimensional contexts ([28]), underscoring the method's non-perturbative and inherently hyperbolic characteristics [29].

The BC-method integrates control and systems theory, asymptotic methods, functional analysis, and operator theory with partial differential equations, indicating its interdisciplinary strength. It has established significant links with Banach algebras ([30], [31]), non-commutative geometry ([32], [33], [34]), and functional models of linear operators ([35], [36]), underscoring the method's comprehensive applicability and depth [37].

Linking the BC method with noncommutative algebra enables its application to elliptic and parabolic problems, suggesting its potential as a unifying solution for Inverse Boundary Value Problems (BVPs). Noncommutative analysis, focused on quantizing observables within arbitrary Poisson brackets, aims to identify operators

 $A_1, \ldots, A_m$  that express the problem's operator through a rich system of relations. This approach allows solving by expressing solutions as functions of these operators, where noncommutative analysis outlines conditions for this method and provides formulas for symbol composition laws. This reduction simplifies the approach to asymptotic problems, making noncommutative analysis particularly effective for various asymptotics. It outperforms wave-packet transform methods in handling simultaneous asymptotics, proving useful in constructing parametrices on manifolds with singularities, applying to asymptotics in weighted function spaces, such as power-law weighted Sobolev spaces near degeneration points [38].

We extend the BC method to noncommutative algebras, paralleling the commutative  $C^*$ -algebra approach [37], employing Gelfand representation. In particular, the work by Heunen et al. [39], [40] introduces a topos-theoretic framework that redefines the Gelfand spectrum for noncommutative C\*-algebras and leading to an explicit Gelfand transform. By constructing a sheaf topos over the poset of commutative subalgebras, their approach introduces an internal Gelfand spectrum that integrates noncommutative algebraic structures with a generalized notion of space. This innovative perspective not only provides a bridge between noncommutative and commutative theories but also leads to the formulation of an external spectrum, enabling a geometrical interpretation of noncommutative spaces analogous to classical manifolds. Selecting an appropriate  $C^*$  algebra  $\mathcal{C}$  for pseudodifferential operators' symbols on manifolds  $\mathcal{M}$ , we can choose the spectrum of  $\mathcal{C}$  as the coordinatization method of the manifold, similarly to [37]. For this purpose, [40] not only adapts the concept of Dirac measures to noncommutative settings but also showcases how the algebra's genericity, i.e. its (topologized) spectrum being homeomorphic to the manifold, emerges from the seamless topological integration of  $\mathcal{M}$  with the external spectrum of the algebra.

Hence, in this paper, we prove the following theorems, whose proofs are the topics of Sections 2.3.1 and 2.3.2, respectively:

**Theorem 2.1.1.** The BC method can be used to directly prove uniqueness arguments for inverse elliptic BVPs.

**Theorem 2.1.2.** The BC method can be used to directly prove uniqueness arguments for inverse Volterra parabolic BVPs.

Led by the insights provided by the previous two theorems, we propose the following conjecture as a topic worthy of further investigation:

**Conjecture 2.1.1.** The BC method potentially unifies inverse BVPs of all types, namely hyperbolic, elliptic, and parabolic.

Finally, based on 2.1.1, we demonstrate that the Calderón problem can be studied directly via the Boundary Control method without reducing the elliptic problem to a hyperbolized problem [41].

We now proceed to state the Calderón problem [42] for a compact smooth Riemannian manifold  $\mathcal{M}$  of arbitrary dimension  $n \geq 2$ . The direct problem is as follows:

$$\nabla \cdot \sigma(x) \nabla u(x) = 0, \quad x \in X$$
  
 
$$u(x) = f(x), \qquad x \in \partial X,$$
 (2.1)

where the domain  $X \subseteq \mathbb{R}^n$  (with  $n \ge 2$ ) is bounded and possesses a smooth boundary denoted as  $\partial X$ . The term  $\sigma(x)$  refers to the conductivity coefficient, assumed to be smoothly varying across X, and f(x) designates the given Dirichlet boundary condition for our problem. For a smooth function f, it has a unique smooth classical solution  $u = u^f(x)$ .

The transformation from Dirichlet to Neumann data, also known as the voltageto-current mapping, is described by:

$$\begin{cases}
\Lambda: H^{\frac{1}{2}}(\partial X) \to H^{-\frac{1}{2}}(\partial X), \\
f(x) \mapsto \Lambda_{\sigma}[f](x) = \sigma(x) \frac{\partial u}{\partial v}(x),
\end{cases} (2.2)$$

where  $(\cdot)_{\nu}$  denotes the outward normal derivative. The Calderón problem involves deducing the conductivity coefficient,  $\sigma$ , by utilizing the data from the Dirichlet-to-Neumann map.

The uniqueness argument for the inverse problem is defined as follows:

**Theorem 2.1.3.** Assume  $\sigma \neq 0$ , and consider the edge problem corresponding to the BVP 2.1. Assuming two locally flat near the boundary manifolds  $\mathcal{M}_i$ , i=1,2, with the same boundary and the same boundary data  $\Lambda$ , the manifolds are isometrically isomorphic for  $\gamma \neq \frac{1}{2}, \frac{3}{2}$ , where  $\gamma$  is the weight factor in the spaces of the edge-degenerate operators.

# 2.2 Quick Overview on Pseudodifferential Operators on Manifolds with Edges

Construction of admissible algebras in manifolds with singularities [43]. A singular manifold  $(M^o, \mathcal{D})$  is defined by its differential operators' behavior, where  $M^o$  is a smooth manifold and  $\mathcal{D}$  an algebra of differential operators. These operators are standard in  $M^o$  but adhere to specific constraints near singular points, ensuring the algebra  $\mathcal{D}$  within any compact subset  $U \in M^o$  aligns with all differential operators having smooth coefficients on  $M^o$  [38, 44]. This framework facilitates handling differential equations on manifolds with singularities, focusing on operator behavior rather than the manifold's embedding or metric properties. The distinction among singular manifolds sharing the same  $M^o$  lies in the differential operators' limits at the manifold's infinite regions, as outlined in [44].

Algebras of differential operators on manifolds with cone and edge singularities. [43], primarily Section 1.1.2. The algebra  $\mathcal{D}$  for differential operators on manifolds with singularities or edges is generated by  $C^{\infty}(M)$  and a space V of vector fields, where V and F, a function space, have inclusions with respect to smooth functions and vector fields on  $M^{\circ}$ . By embedding  $M^{\circ}$  into a compact manifold M and extension of a non-degenerate Riemannian metric  $d\rho^2$  from  $M^{\circ}$  to M, V is then characterized via its dual space V' based on an F-valued inner product, making V = V'. This construction uniquely defines  $\mathcal{D}$ , which then ties manifolds to two categories; with conical singularities or edges, depending on the operator type.

Symbols for cone-degenerate differential operators. [43], Section 1.2.6. The principal symbol, analogous to that in smooth manifolds, emerges within the structure of the differential operator algebra  $\mathcal{D}$ , organized by order into a hierarchy  $\mathcal{D}_k$ .

2.2. Quick Overview on Pseudodifferential Operators on Manifolds with Edges 25

This organization leads to a graded algebra gr  $\mathcal{D} = \bigoplus_{j=0}^{\infty} \mathcal{D}_j/\mathcal{D}_{j-1}$ , with  $\mathcal{D}_{-1} = \{0\}$ . For an operator D of order k, its principal symbol  $\Sigma(D) = \Sigma_k(D)$  is identified through projection to  $\operatorname{gr}_k \mathcal{D}$ . In smooth contexts, this symbol functions over the cotangent bundle  $T^*M$ , guiding from space M to  $T^*M$ . The transition, or microlocalization, especially for manifolds with conical singularities, lacks a clear phase space definition, prompting a two-stage process to navigate potential complexities.

Stage 1. Localization. [43]. Functions in  $C^{\infty}(\mathcal{M})$ , constant on the boundary, are a subalgebra in the differential operator algebra  $\mathcal{D}$ , exhibiting a commutation relation indicative of a  $C^{\infty}(\mathcal{M})$ -module structure in the associated graded algebra  $\operatorname{gr}\mathcal{D}$ . Symbol spaces  $\Sigma_{kx}$  localize the symbol order k to a point x on  $\mathcal{M}$ . The set of local representatives of an operator D in  $\mathcal{D}_k$ , denoted  $\sigma_x(D)$ , uniquely determines D's principal symbol. These local representatives can be conveniently described via a scaling procedure related to the metric's induced local scaling transformations  $g_{\lambda}$  around point x. This leads to defining the scaled operator  $D_x$  by the limit of scaled operations on D, with the limit interpreted in terms of pointwise convergence. This limit exists for any D in  $\mathcal{D}_m$  and establishes a bijective, multiplicative correspondence between  $\sigma_x(D)$  and  $D_x$ . This localizes each operator D to a family of operators  $D_x$ , representing D's class in  $\operatorname{gr}_m \mathcal{D}$  on the space  $K_x$ , adjusted for interior points and the conical point specifically.

Stage 2. Microlocalization. [43]. For each interior point x, the constant-coefficients operator  $D_x$  on  $T_xM$  leads to the polynomial  $P_m(0, \xi)$  via Fourier transform, representing D's principal symbol in  $T^*M$ 's fiber over x. This symbol,  $\sigma(D)$ , extends to a smooth function across  $T^*\mathcal{M}$ , defining the *interior symbol*. Conversely, at the conical point,  $D_x$  lacks translation invariance, precluding microlocalization, and is directly termed the *cone symbol*,  $\sigma_c(D)$ , preserving the distinct treatments for interior and conical points in symbol analysis.

Symbols for edge-degenerate differential operators.[43]. The algebra  $\mathcal{D}$  of edge-degenerate differential operators is filtered by operator order, defining symbols within  $\operatorname{gr} \mathcal{D} = \bigoplus_{m=0}^{\infty} \mathcal{D}_m/\mathcal{D}_{m-1}$ . The principal symbol of an operator  $P \in \mathcal{D}_m$  is its image in  $\mathcal{D}_m/\mathcal{D}_{m-1}$ . This principal symbol, detailed for edge-degenerate operators,

2.2. Quick Overview on Pseudodifferential Operators on Manifolds with Edges 26 combines the *interior symbol* and the *edge symbol*. The interior symbol,  $\sigma(D)$ , derived from the classical symbol  $\sigma_{clas}(D)$ , extends smoothly to  $T^*\mathcal{M}$ . The edge symbol,  $\sigma_{\wedge}(D)(x, \xi)$ , represented in local coordinates, forms a well-defined operator family on  $K_{\Omega_x}$ , parameterized by  $T^*X$  points. The compatibility condition ensures the interior and edge symbols of  $D \in \mathcal{D}_m$  satisfy  $\sigma(\sigma_{\wedge}(D)) = \sigma_{\partial}(D)$ , integral to symbol definitions for edge-degenerate differential operators on manifolds with edges. This setup indicates that M acts as the stretched manifold of  $\mathcal{M}$ .

Algebras of pseudodifferential operators on manifolds with cone and edge singularities. The task involves extending the algebra  $\mathcal{D}_k(M)$  to  $PS\mathcal{D}_k(M)$ , including pseudodifferential operators, with emphasis on handling singular points on  $\mathcal{M}$ . The approach is local, constructing these operators in coordinate charts and integrating them across the manifold using partitions of unity, similar to conventional pseudodifferential operator theory [45]. Special focus is on constructing admissible pseudodifferential operators near singularities, extending symbol classes beyond polynomials via noncommutative analysis [38].

STEP 1. Function spaces. The algebra for pseudodifferential operators is defined within a scale of Hilbert spaces, essential for ensuring the operators act in function spaces suitable for singular elliptic differential operators [38]. These spaces must align with solutions of differential equations, with the choice proven critical for theoretical integrity [44], [38]. Specifically, within  $\mathcal{M}$ 's interior, these function spaces match traditional Sobolev spaces, while near singularities, the spaces adapt to the singularity type, differentiated into cone-degenerate and edge-degenerate categories [43].

Function spaces for cone-degenerate operators. [43], Section 2.1.1. Weighted Sobolev spaces  $H^{s,\gamma}(\mathcal{M})$  are tailored for cone-degenerate elliptic operators, incorporating solutions of homogeneous equations and exhibiting a norm invariance property near singularities [43]. These spaces match ordinary Sobolev spaces in  $\mathcal{M}$ 's interior and adapt to singularity types near conical points. The norm calculation for  $H^{s,\gamma}(\mathcal{M})$  relies on functions near singularities, transitioning to the model cone  $K = K_{\Omega}$  for a global group action. The weighted Sobolev space norm combines standard Sobolev

2.2. Quick Overview on Pseudodifferential Operators on Manifolds with Edges 27 norms and localized norms near singularities, forming a scale of Hilbert spaces invariant under specific transformations [43]. Cone-degenerate differential operators maintain continuity within these spaces, ensuring operator applicability across different Sobolev scales [43].

Function spaces for edge-degenerate operators. [43], Section 2.1.1. In studying edge-degenerate operators, we define function spaces that accommodate the operators' behavior near and away from the manifold's edge, ensuring coherence across these regions. For the cone  $K_{\Omega}$ , we integrate usual Sobolev spaces at infinity with weighted Sobolev spaces near the vertex, employing a partition of unity for seamless transitioning. This approach creates the space  $\mathcal{K}^{s,\gamma}(K_{\Omega})$ , blending local and global function norms ([46]). Abstract wedge spaces  $\mathcal{W}^s(\mathbb{R}^n, H)$  extend this concept to manifold edges, adapting through Fourier transform methods and scaling by a strongly continuous operator group  $\kappa_{\lambda}$ , leading to the specific space  $\mathcal{W}^{s,\gamma}(W)$  for an infinite wedge. This construction is then applied to the entire manifold  $\mathcal{M}$ , forming  $\mathcal{W}^{s,\gamma}(\mathcal{M})$  which integrates edge behavior with the manifold's bulk properties. An edge-degenerate differential operator D operates continuously within these constructed spaces, confirming the adequacy of the spaces  $\mathcal{W}^{s,\gamma}(\mathcal{M})$  for hosting solutions to edge-degenerate differential equations [43].

STEP 2. Symbols. Describe the admissible class of symbols. [38]. For applications in noncommutative analysis, the symbol class  $S^{\infty}(\mathbb{R}^n)$  is optimal. Yet, in the context of pseudodifferential operators, symbols typically have uniform dependence on spatial variables without infinite growth. Symbols that do exhibit growth are not bounded within the relevant spaces, nor are they part of the algebra, a fact that applies to manifolds with singularities too. To facilitate analysis of such operator algebras and symbol classes, the approach to functions of noncommuting operators is expanded to include operator-valued symbols.

Symbols for cone-degenerate pseudodifferential operators.[43], Section 3.4.1. On a manifold  $\mathcal{M}$  with conical singularities, the principal symbol of a cone-degenerate pseudodifferential operator D combines the interior symbol  $\sigma(D)$  and the cone symbol  $\sigma_c(D)$ . The interior symbol, a function on the stretched cotangent

bundle  $T_0^*\mathcal{M}$ , is homogeneous of order m in the fibers. The cone symbol, defined through the concept of conormal symbols, is an mth-order pseudodifferential operator with parameter p on the base  $\Omega$  of the cone, continuous in weighted Sobolev spaces. Compatibility between interior and cone symbols is required for them to form a principal symbol, indicated when the principal symbol of the cone symbol matches the restriction of the interior symbol to  $\partial T_0^*\mathcal{M}$ . This framework accommodates the analysis of pseudodifferential operators on manifolds with singularities, encapsulating both local and global operator characteristics [47], [43].

Symbols for cone-degenerate pseudodifferential operators.[43], Section 3.4.1. On a manifold  $\mathcal{M}$  with conical singularities, the principal symbol of a cone-degenerate pseudodifferential operator D combines the interior symbol  $\sigma(D)$  and the cone symbol  $\sigma_c(D)$ . The interior symbol  $\sigma = \sigma(y, \eta)$  is a function on the stretched cotangent bundle  $T_0^*\mathcal{M}$ , homogeneous of order m in the fibers. Cone symbols are defined via conormal symbols, which are mth-order pseudodifferential operators on the manifold  $\Omega$  with a specific parameter. These symbols, when associated with a conormal symbol, form the cone symbol  $\sigma_c$ , operating in weighted Sobolev spaces on the infinite cone  $K_{\Omega}$ . Compatibility between  $\sigma$  and  $\sigma_c$  ensures that they form principal symbols of the operator D, characterized by a shared boundary symbol  $\sigma_{\partial}$  [47].

Symbols for edge-degenerate pseudodifferential operators. [43], Section 3.4.2. For compact manifolds  $\mathcal{M}$  with an edge X and a cone base  $\Omega$ , the principal symbols of edge-degenerate operators consist of interior symbols  $\sigma$  and edge symbols  $\sigma_{\wedge}$ . Interior symbols are homogeneous functions on the stretched cotangent bundle, while edge symbols represent families of differential or pseudodifferential operators on  $K_{\Omega}$ , parameterized by  $T_0^*X$  and acting in  $\mathcal{K}^{s,\gamma}(K_{\Omega})$ . Edge symbols incorporate conditions for twisted homogeneity, continuity, almost compact fiber variation, and are defined in both local neighborhoods of the cone vertex and its exterior. The compatibility between interior symbols and cone symbols ensures the principal symbol's coherence. Edge symbols, represented by the formula  $\sigma_c = r^{-m} \sigma_c \left( i r \frac{\partial}{\partial r} \right)$ , are continuous in weighted Sobolev spaces, signifying the structured approach in defining operator

2.2. Quick Overview on Pseudodifferential Operators on Manifolds with Edges 29 families for edge-degenerate pseudodifferential operators on manifolds with singular edges.

### STEP 3. Quantization

Quantization on manifolds with cones. [43], Section 3.4.1. In order to thus associate a pseudodifferential operator in weighted Sobolev spaces on on  $\mathcal{M}$  to each principal symbol, we introduce negligible operators, which are compact in D:  $H^{s,\gamma}(\mathcal{M}) \to H^{s-m,\gamma-m}(\mathcal{M})$ , and continuous for  $D: H^{s,\gamma}(\mathcal{M}) \to H^{s-m+1,\gamma-m}(\mathcal{M})$ . We then construct a pseudodifferential operator D of order m and weight  $\gamma$  with principal symbol  $\bullet$  to be continuous in these spaces, its definition modulo negligible operators. These operators, denoted by  $\Psi^m_{\gamma}(M)$ , have well-defined principal symbols, and the principal symbol  $\bullet(D)$ , uniquely characterizes each  $D \in \Psi^m_{\gamma}(M)$ . The compactness of it within  $\Psi^m_{\gamma}(M)$  signals its location in the space of negligible operators  $I^m_{\gamma}$ .

Quantization on manifolds with edges. [43], Section 3.4.3. Operators of order m on the compact manifold  $\mathcal{M}$  with edges are defined as those extendable to continuous from  $\mathcal{W}^{s,\gamma}(\mathcal{M})$  to  $\mathcal{W}^{s-m,\gamma-m}(\mathcal{M})$  for every  $s \in \mathbb{R}$ . These are called *negligible operators* when compactly-mapped between these spaces and are included in  $J\operatorname{Op}\gamma^m(\mathcal{M})$ . The pseudodifferential operators of order m and weight  $\gamma$  have unique principal symbols, which can be written down as composed of interior symbol  $\sigma \in C^{\infty}(T0^*\mathcal{M})$  and edge symbol  $\sigma_{\wedge}$ . These symbols need to satisfy compatibility condition. Then they can be together quantized, and the obtained pair  $(\sigma, \sigma_{\wedge})$  is unique for each operator P. This ensures that the operator is precisely defined from its principal symbol within the framework of weighted Sobolev spaces on a compact manifold with edges. The resulting pseudodifferential operators' algebra is denoted by  $PSD_{\gamma}^m(\mathcal{M})$ .

STEP 4. Algebra formation. We study whether the symbols of the aforementioned pseudodifferential operators form an algebra. In [43], the algebra of principal symbols for zero-order pseudodifferential operators ( $\psi$ DOs) (the general case follows by order reduction) is defined within a Hilbert space  $\mathcal{H}$ , emphasizing the role of a symbol mapping  $\sigma$  that distinguishes operators by their association to the ideal

 $\mathcal{K}$  of compact operators. This setup yields a monomorphism  $\tilde{\sigma}$  of the Calkin algebra into a unital topological algebra S, alongside a linear mapping Q serving as the right inverse of  $\sigma$ , facilitating quantization. Essentially, S represents the algebra of (principal) symbols for  $\tilde{\mathcal{A}}$ , making it isomorphic to the corresponding Calkin algebra, which is a  $C^*$  algebra.

**Edge problems**. [43], Chapter 6. In the theory of operators on manifolds with edges, boundary value problems are a specific instance where the edge acts as the boundary and the cone simplifies to  $\mathbb{R}_+$ , representing the inner normal [46]. Addressing elliptic problems on these manifolds involves modifying the problem to ensure the edge symbol becomes invertible, often through the inclusion of boundary and coboundary operators in a matrix operator setup. This adaptation, rooted in the physical context of boundary conditions in Fredholm problems, may not always be feasible due to potential topological constraints akin to the Atiyah-Bott obstruction in boundary value problem theory.

Edge boundary and coboundary operators. [43], Section 6.1.2. In addressing Fredholm problems for operators on manifolds with edges, matrix operators incorporating edge boundary and coboundary conditions are essential. These operators, organized in a  $2 \times 2$  matrix format, integrate pseudodifferential operators with specific edge-focused components. This approach, critical for ellipticity and parabolicity studies, involves operators that are defined modulo negligible ones, aiming for operators that are compact and continuous across specified weighted Sobolev spaces [43]. The framework extends to defining both edge boundary and coboundary symbols as pseudodifferential operators on X, emphasizing their compact and continuous nature in adapted Sobolev spaces, ensuring the operators are finely tuned to the edge's properties. This method underscores a comprehensive strategy for handling complex operator conditions on manifolds with edges.

The calculus of edge morphisms. [43], Section 6.1.3. Defining edge boundary and coboundary operators within a framework for operators on manifolds with edges, [43] introduces a comprehensive classification of operators as morphisms of order m and weight  $\gamma$ . These morphisms, formed in a matrix operator setup

2.2. Quick Overview on Pseudodifferential Operators on Manifolds with Edges 31 combining pseudodifferential, boundary, and coboundary components, allow for the representation of complex boundary conditions integral to Fredholm problems. Key to this formalism is the concept of principal symbols for these morphisms, encapsulating both the interior symbol of the operator A and an operator family forming the edge symbol, characterized by continuity and compactness properties in weighted Sobolev spaces. This structure underpins the analytical approach to elliptic problems on manifolds with edges, emphasizing compatibility conditions essential for morphism definition and the subsequent mathematical treatment of boundary phenomena.

### Inverse elliptic BVPs via BC method

Ellipticity and finiteness theorems

Ellipticity and finiteness theorems for degenerate  $\psi$ DOs. [43], Section 3.5.1. and Section 3.5.4. In the degenerate  $\psi$ DO algebra  $\mathcal{A}$  constructed by [43], an operator A is termed elliptic if its symbol  $\sigma(A)$  is invertible in the symbol algebra S. The main result of elliptic theory, the finiteness theorem, asserts that an operator is Fredholm if its symbol is invertible. This theorem applies to cone-degenerate and edge-degenerate  $\psi$ DOs on manifolds with conical singularities and edges, respectively, defining ellipticity through the invertibility of operators' symbols and stating that elliptic operators are Fredholm, with their kernel, cokernel, and index remaining constant across different smoothness levels.

Ellipticity and finiteness theorems for edge problems. [43], Section 6.1.4. For a morphism A within the degenerate  $\psi DO$  algebra  $\mathcal{A}$ , [43] defines it as elliptic if its interior symbol is invertible across the entire cotangent bundle  $T_0^*\mathcal{M}$  and its edge symbol is invertible on  $T_0^*X$ . Such elliptic morphisms are Fredholm across all considered spaces, maintaining constant kernel, cokernel, and index regardless of smoothness level s. Additionally, an elliptic morphism is uniquely identified by its principal symbol modulo negligible operators, underlining the pivotal role of the symbol in determining ellipticity and Fredholm properties.

The obstruction to ellipticity. [43], Section 6.2. For an operator *A* on a manifold with an edge, constructing an elliptic edge problem requires adding boundary

operators B, coboundary operators C, and a pseudodifferential operator D on the edge. The solvability of such a problem hinges on the interior ellipticity of A and a Fredholm condition on its edge symbol, as detailed in [43]. The crux is that for A to be part of an elliptic edge problem, its edge symbol's index must vanish in a specific K-theory element, influenced solely by A's interior symbol.

**Inverse parabolic BVPs via BC method**. [48]. In the complex upper half-plane  $\mathbb{H}$ , we explore symbol spaces  $S^{\mu;\ell}(\mathbb{R}^n \times \mathbb{R}^q; E, \tilde{E})$  composed of smooth, bounded functions from  $\mathbb{R}^n \times \mathbb{R}^q$  into  $\mathcal{L}(E, \tilde{E})$ , where E and  $\tilde{E}$  are Hilbert spaces. These spaces, equipped with a topology defined by a seminorm system, include symbols that are (anisotropic) homogeneous of degree  $\mu$ . We also define the space of symbols of infinite order,  $S^{-\infty}(\mathbb{R}^n \times \mathbb{R}^q; E, \tilde{E})$ , and extend these definitions to symbols dependent on spatial variables. Furthermore, classical symbols  $S_{\rm cl}^{\mu;\ell}(\mathbb{R}^n \times \mathbb{R}^q; E, \tilde{E})$ comprise a subset characterized by an asymptotic sum of homogeneous components. Similarly, for the Volterra property in symbols, we define  $S_V^{\mu;\ell}(\mathbb{R}^n \times \mathbb{H}; E, \tilde{E})$  emphasizing operators analytically extendable into the complex plane's interior, alongside corresponding definitions for pseudodifferential operators. Parabolic symbols and operators within this framework are distinguished by their parameter-dependent ellipticity. This detailed symbolic structure underpins the analysis of operators on manifolds, particularly emphasizing the treatment of elliptic and parabolic types in various contexts. Essential to this theory is the notion of parabolicity for operators in manifolds with edges, as encapsulated in [13], where both the interior symbol's parabolic nature and the edge symbol's invertibility criterion play crucial roles.

### 2.3 Proofs on BC method extensions

### **2.3.1** Proof on BC for elliptic problems

### 2.3.1.1 Facts to be used in the proof

All definitions/facts included in the following itemized lists are from [43].

Graded Algebra and Principal Symbol

- [D0] For a manifold  $\mathcal{M}$  with a  $C^{\infty}$  structure densely defined on a subset  $\mathcal{M}^{\circ}$ , the algebra  $Diff(\mathcal{M}^{\circ})$  includes all differential operators with smooth coefficients on  $\mathcal{M}^{\circ}$ . A subalgebra  $\mathcal{D} \subset Diff(\mathcal{M}^{\circ})$  is defined by selecting operators based on their behavior near the singularity set  $\mathcal{M} \setminus \mathcal{M}^{\circ}$ , emphasizing the algebra's responsiveness to the manifold's singular and non-singular regions.
- [D1] We define  $\mathcal{D}$  with an order-based filtration:  $\{0\} = \mathcal{D}_{-1} \subset \mathcal{D}_0 \subset \mathcal{D}_1 \subset \cdots$ . This leads to the formation of the associated graded algebra gr  $\mathcal{D} = \bigoplus_{j=0}^{\infty} \mathcal{D}_j / \mathcal{D}_{j-1}$ , where  $\operatorname{gr}_k \mathcal{D}$  isolates symbols of operators precisely of order k, thus segregating different order effects.
- [D2] The principal symbol of an operator D in  $\mathcal{D}_k$ , noted as  $\Sigma_k(D)$ , abstracts the operator's highest-order impact by projecting D to  $\operatorname{gr}_k \mathcal{D}$  through the map  $\Sigma_k : \mathcal{D}_k \to \operatorname{gr}_k \mathcal{D}$ . This operation discards lower-order influences, highlighting the core action of D.
- [D3] Globally, utilizing a partition of unity to "glue" these local correspondences together, while carefully selecting invertible pseudodifferential operators to circumvent topological obstructions, allows for the extension of local algebraic and geometric properties of  $\mathcal{D}$  across the entire manifold  $\mathcal{M}$ .

### Localization of Principal Symbol and Monomorphism

- [L0] Let the stretched manifold M be a compactification and extension of the singular space  $\mathcal{M}$ , which "stretches" over the singular points of  $\mathcal{M}$ , effectively smoothing out the singularities. The subspace  $C^{\infty}(\mathcal{M}) \subset C^{\infty}(M)$  acts as a natural subalgebra within  $\mathcal{D}$ , with the commutation relation  $[C^{\infty}(\mathcal{M}), \mathcal{D}_k] \subset \mathcal{D}_{k-1}$  indicating that  $C^{\infty}(\mathcal{M})$  effectively operates on the graded algebra  $\operatorname{gr} \mathcal{D}$ , rendering each  $\operatorname{gr}_k \mathcal{D}$  a  $C^{\infty}(\mathcal{M})$ -module, where the left and right actions coincide.
- [L1] Localization at a point  $x \in \mathcal{M}$  targets the action of  $\mathcal{D}$ 's operators at x. This process uses the maximal ideal  $I_x \subset C^{\infty}(\mathcal{M})$ , comprised of functions zero at x, to adapt the algebra to local considerations.

- [L2] Through localization, each operator D's principal symbol,  $\Sigma_k(D)$ , is represented at x by  $\sigma_x(D)$ , determined via  $\Sigma_{kx} = \operatorname{gr}_k \mathcal{D}/I_x \operatorname{gr}_k \mathcal{D}$ . This representation captures the operator's highest-order behavior near x, effectively tying algebraic properties to manifold's topology.
- [M1] The monomorphism induced by mapping  $\pi: \operatorname{gr}_k \mathcal{D} \to \prod_{x \in \mathcal{M}} \Sigma_{kx}$ , with each  $\pi_x: \operatorname{gr}_k \mathcal{D} \to \Sigma_{kx}$  acting as a natural projection, ensures that the set of local representations  $\{\sigma_x(D)\}$  uniquely identifies the principal symbol of D, thereby establishing a direct link between the algebra's elements and their manifestations across  $\mathcal{M}$ .

### Scaling for Localized Behavior

[S1] To discern the influence of D at x, scaling transformations  $g_{\lambda}$  for  $\lambda \in \mathbb{R}_+$  adjust D for local behavior analysis. The limit  $D_x = \lim_{\lambda \to \infty} \lambda^{-m} (g_{\lambda}^*)^{-1} D g_{\lambda}^* u$ , for  $u \in C_0^{\infty}(K_x)$  and excluding x for singular points, showcases D's localized impact, correlating with  $\sigma_x(D)$ .

### Fundamental Relationship

[T1] The relationship  $\sigma_x(D) \mapsto D_x$  is both 1-1 and multiplicative, highlighting the principal symbol's role in unveiling D's essence in a localized context. This interplay, facilitated by the monomorphism in [M1] and the scaling process in [S1], deepens our comprehension of differential operators' localized effects, affirming the algebra  $\mathcal{D}$ 's adaptability and the continuity of its application across  $\mathcal{M}$ .

### Edge Symbols

[E1] Edge symbols, represented as  $D(x;\xi)$ , act on the specific weighted Sobolev spaces  $K_{\gamma}^{s}(K_{\Omega})$ , which are constructed by gluing weighted and standard Sobolev spaces across different regions of the cone  $K_{\Omega}$ .  $K_{\gamma}^{s}(K_{\Omega})$  is an adaptation for cone structures of the abstract wedge spaces  $\mathcal{W}^{s}(\mathcal{M};K_{\Omega})$ . The

connection between the algebraic structure of edge symbols and  $\mathcal{W}^s(\mathcal{M}; K_{\Omega})$  underlies the continuity and scaling properties essential for the functionality of edge-degenerate pseudodifferential operators within the  $\mathcal{W}^s(\mathcal{M}; K_{\Omega})$  spaces.

### Quantization

[Q1] The exact sequence

$$0 \to J_{\gamma}^m \to \mathcal{A}_{\gamma}^m \to \mathcal{O}^m \to 0$$

delineates the structural relationships in the algebra of quantization for pseudodifferential operators. Here,  $J_{\gamma}^{m}$  is an ideal comprising edge symbols,  $\mathcal{A}_{\gamma}^{m}$  is an algebra of both interior and edge symbols meeting specific compatibility conditions, and  $\mathcal{O}^{m}$  consists of interior symbols, enabling a comprehensive formulation of quantization processes in the context of manifold  $\mathcal{M}$ .

### Calkin Algebra

- [A1] Let  $\mathcal{H}$  denote a Hilbert space, and  $\mathcal{B}(\mathcal{H})$  the algebra of bounded operators on  $\mathcal{H}$ . The set  $\tilde{\mathcal{A}} \subset \mathcal{B}(\mathcal{H})$ , representing zero-order pseudodifferential operators ( $\psi$ DO), forms a subalgebra known as the general algebra of zero-order  $\psi$ DOs (the general case follows by order reduction).
- [A2] A homomorphism  $\sigma: \tilde{\mathcal{A}} \to S$  is defined, mapping  $\tilde{\mathcal{A}}$  into a unital topological algebra S. This mapping is characterized by  $\sigma(A) = 0$  if and only if  $A \in \mathcal{K}$ , where  $\mathcal{K}$  denotes the ideal of compact operators within  $\mathcal{B}(\mathcal{H})$ .
- [A3] The symbol mapping  $\sigma$  induces a well-defined monomorphism  $\tilde{\sigma}: \tilde{\mathcal{A}}/(\mathcal{K}\cap \tilde{\mathcal{A}}) \to S$ , effectively establishing a one-to-one correspondence between the elements of the Calkin algebra  $\tilde{\mathcal{A}}/(\mathcal{K}\cap \tilde{\mathcal{A}})$  and the elements within S.
- [A4] There exists a continuous linear mapping  $Q: S \to \tilde{\mathcal{A}}$ , for which  $\sigma(Q(s)) = s$  for all  $s \in S$ , making Q the right inverse of  $\sigma$ . This mapping is instrumental in ensuring that the structure and relational properties between  $\tilde{\mathcal{A}}$  and S are preserved.

Edge Morphisms

[EM1] A morphism A of order m and weight  $\gamma$ , represented as an operator matrix  $A = \begin{pmatrix} A & C \\ B & D \end{pmatrix}$ , includes A as a pseudodifferential operator on  $\mathcal{M}$ , with B and C as edge boundary and coboundary operators, and D as a pseudodifferential operator on the edge X, all of order m and weight  $\gamma$ . The set of such morphisms is denoted by  $\mathrm{Mor}_{\gamma}^{m}(\mathcal{M})$ . The interior symbol of morphism A,  $\sigma(A)$ , is defined as  $\sigma(A)$ , the interior symbol of the operator A.

#### 2.3.1.2 Lemmas

In the framework of a noncommutative Calkin algebra on a manifold, we deploy a topos-theoretic approach in accordance to [40]. The internal spectrum models a C\*-algebra's structure within a sheaf topos, and the external spectrum effectively translates these algebraic points into a topological structure that can be visualized as points in a space. It is inferred from [40] that norm convergence in an algebra A implies topological convergence in the external spectrum  $\Sigma_{\rm ext}A$ , as the latter carries the weak\* topology, which respects norm limits. In particular, the topology of the internal spectrum, which is aligned with weak\* features suitable for C\*-algebra structures, is reflected in the external spectrum to maintain mathematical consistency and meaningful interpretation. Based on this inference the map  $\varepsilon : \mathcal{M} \to \Sigma_{\rm ext}A$ , where  $\varepsilon_x = \delta_x$  represents the Dirac measure is meaningful.

The Calkin algebra  $\mathcal{C}$  on  $\mathcal{M}$ , defined in [A3], achieves a notion of 'genericity' through the homeomorphic relation established between  $\mathcal{M}$  and  $\Sigma_{ext}(\mathcal{C})$  via the embedding  $\varepsilon$ , enriched by a topos-theoretic generalization of spatial isomorphism; the Gelfand transform  $\hat{\mathcal{C}} \cong \mathcal{C}$  in this context reflects a deep algebraic-geometric correspondence, emphasizing the continuity and topological equivalence between  $\mathcal{M}$  and  $\Sigma_{ext}(\mathcal{C})$ .

Additionally in [40] the broadened perspective on spectrum and space through sheaf toposes and frames offers the flexibility to rigorously define and use the external spectrum for non-C\*-algebraic structures, if it can be described within a suitable framework (like a topos or through frame theory). Hence, the algebra S ([A2], [A3]) is eligible for external spectrum. In particular, defining  $\varepsilon: M \to \Sigma_{ext}(\mathcal{C})$ ,

where  $\varepsilon_x = \delta_x$  is the Dirac measure, the continuity of  $\varepsilon$  and its inverse suggest that S respects the spatial topology required for an external spectrum; this continuity ensures that S can be effectively treated as a fibered space over the manifold, akin to the external spectrum's behavior over the base space of subalgebras. Also the algebraic operations within S need to be compatible with the fibered structure; the monomorphism [A3] and symbol mapping [A2] ensure that S retains algebraic properties consistent with the Calkin algebra, crucial for its interpretation as an external spectrum. Of course, an internal spectrum cannot be constructed for S due to its potentially non-C\*-algebra properties, hence S has no explicit Gelfand transform.

Let us note that S in [A2] can refer to either interior or edge symbol algebras of the edge-degenerate PDOs. However, in what follows, for ease of writing, by abuse of terminology, we will refer to S as the algebra of principal symbols (standard ones; not the ones for edge-degenerate operators), instead of the algebra of interior symbols, as the two essentially coincide.

**Lemma 2.3.1.** There is a one-to-one correspondence between points on the manifold  $\mathcal{M}$  and the external spectrum  $\Sigma_{ext}(S)$  of principal symbols S, which is related to differential operators on  $\mathcal{M}$ .

Proof.

Local Association Through Localization. ([L1], [L2]). For any point x on  $\mathcal{M}$ , the process of localization maps the behavior of differential operators at x. This involves identifying the principal symbols  $\sigma_x(D)$  for each differential operator D at x, using maximal ideals  $I_x$  comprised of functions that are zero at x.

Global Extension and Correspondence. The monomorphism [M1] expands these local associations to a global structure within S. It guarantees that the connections between points x on  $\mathcal{M}$  and their localized algebraic behaviors via  $\sigma_x(D)$  correspond to unique maximal ideals in S without overlap. This ensures a one-to-one correspondence between points on  $\mathcal{M}$  and maximal ideals in S, summarizing the differential actions at each point x.  $\square$ 

**Lemma 2.3.2.** There is one-to-one correspondence between the manifold  $\mathcal{M}$  and the external spectrum  $\Sigma_{ext}(\mathcal{C})$  of the Calkin algebra,  $\tilde{\mathcal{A}}/(\mathcal{K}\cap\tilde{\mathcal{A}})$ .

*Proof.* By [A3],  $\tilde{\sigma}$  creates a one-to-one correspondence between maximal ideals in the Calkin algebra and S, preserving their structural and relational properties. By Lemma 2.3.1 the external spectrum  $\Sigma_{ext}(S)$  of S and the manifold are in 1-1 correspondence. Therefore, there is one-to-one correspondence between the manifold and the external spectrum of the Calkin algebra.  $\square$ 

**Lemma 2.3.3.** The map  $\varepsilon : \mathcal{M} \to \Sigma_{ext} S$ , where  $\varepsilon_x = \delta_x$  is the Dirac measure, associating each point x in the manifold  $\mathcal{M}$  with a maximal ideal of the external spectrum  $\Sigma_{ext} S$  of the algebra S, is continuous.

*Proof.* In accordance to the constructions in [40], norm convergence in S implies topological convergence in the external spectrum  $\Sigma_{\text{ext}}S$ ; as was explained in the beginning of this section.

Evaluation Map Definition for S. Define  $ev_x(\sigma(D))$  for any  $x \in \mathcal{M}$  and a symbol  $\sigma(D) \in S$  to denote the action of the differential operator D at x, modulo lower order terms, reflecting the graded nature of S.

Density and Approximation Argument. Given  $\sigma(D) \in S$  and any  $\varepsilon > 0$ , we utilize the density of  $\mathcal{D}$  in  $\tilde{\mathcal{A}}$  [D0] to select  $D' \in \mathcal{D}$  such that  $\sigma(D')$  approximates  $\sigma(D)$  in the norm of S, i.e.,  $\|\sigma(D) - \sigma(D')\|_{S} < \varepsilon/3$ .

Formal Convergence Argument. For a converging sequence  $x_n \to x$  in  $\mathcal{M}$ , and considering  $\sigma(D') \in S$  that closely approximates  $\sigma(D)$  in S:

$$\|\sigma(D)(x_n) - \sigma(D)(x)\|_S \le \|\sigma(D)(x_n) - \sigma(D')(x_n)\|_S + \|\sigma(D')(x_n) - \sigma(D')(x)\|_S + \|\sigma(D')(x) - \sigma(D)(x)\|_S,$$

where the continuity of D' ensures  $\|\sigma(D')(x_n) - \sigma(D')(x)\|_S \to 0$  as  $n \to \infty$ .

Ensuring Continuity. This formulation guarantees that  $\|\sigma(D)(x_n) - \sigma(D)(x)\|_S < \varepsilon$ , affirming the continuity of  $\varepsilon$ .

**Lemma 2.3.4.** The map  $\varepsilon : \mathcal{M} \to \Sigma_{ext} \mathcal{C}$ , where  $\varepsilon_x = \delta_x$  is the Dirac measure, associating each point x in the manifold  $\mathcal{M}$  with a maximal ideal of the external spectrum  $\Sigma_{ext} \mathcal{C}$  of the Calkin algebra  $\mathcal{C}$  is continuous.

*Proof.* The argument is the same with the one in Lemma 2.3.3 applied to  $[A] \in \mathcal{C}$ , denoting the action of A modulo compact operators at x in accordance to the algebra's quotient structure, instead of  $\sigma(D) \in S$ , and with the density argument:

Given  $[A] \in \mathcal{C}$  and any  $\varepsilon > 0$ , we utilize the density of  $\mathcal{D}$  in  $\tilde{\mathcal{A}}$  to select  $D \in \mathcal{D}$  such that [D] approximates [A] in the quotient norm of  $\mathcal{C}$ , i.e.,  $\|[A] - [D]\|_{\mathcal{C}} < \varepsilon/3$ .  $\square$ 

**Lemma 2.3.5.** The map  $\varepsilon^{-1}: \Sigma_{ext}S \to \mathcal{M}$ , where  $\varepsilon_x = \delta_x$  is the Dirac measure, from a maximal ideal of the external spectrum  $\Sigma_{ext}S$  of the algebra S, to a point in the manifold  $\mathcal{M}$ , is continuous.

*Proof.* In accordance to the constructions in [40], norm convergence in S implies topological convergence in the external spectrum  $\Sigma_{\text{ext}}S$ ; as was explained in the beginning of this section.

Sequence of Ideals and Convergence. Assume a sequence of maximal ideals  $M_n$  converges to M in  $\Sigma_{ext}S$ . This implies that for every principal symbol  $\sigma(D) \in S$ , the evaluation at  $M_n$  (which can be thought of as evaluating  $\sigma(D)$  at the points  $x_n$  corresponding to  $M_n$ ) converges to the evaluation at M (evaluation at the point x corresponding to M) as  $n \to \infty$ , i.e.

$$\sigma(D)|_{M_n} \to \sigma(D)|_M$$
 as  $n \to \infty$ .

Approximation and Density in  $\mathcal{D}$ . For any  $\sigma(D) \in S$  and given  $\varepsilon > 0$ , there exists an operator  $D' \in \mathcal{D}$  approximating  $\sigma(D)$  within S, such that  $\|\sigma(D) - \sigma(D')\|_S < \varepsilon/3$ . This uses the density of  $\mathcal{D}$  in  $\tilde{\mathcal{A}}$  [D0].

Continuity of  $\sigma(D')$  and Convergence of Points. Consider  $x_n, x \in \mathcal{M}$  corresponding to  $M_n, M$ , respectively. The continuity of D' implies  $D'(x_n) \to D'(x)$ . Since  $\sigma(D')$  reflects D''s highest-order action, this continuity extends to  $\sigma(D')$ , ensuring that the evaluations  $\sigma(D')(x_n)$  converge to  $\sigma(D')(x)$  within the algebraic framework of S.

Ensuring Continuity of  $\varepsilon^{-1}$ . The convergence  $\sigma(D')(x_n) \to \sigma(D')(x)$ , due to the operational continuity of D' and its approximation of  $\sigma(D)$ , ensures that the spectral convergence  $M_n \to M$  mirrors as the topological convergence  $x_n \to x$  on  $\mathcal{M}$ ,

thereby demonstrating the continuity of  $\varepsilon^{-1}$ .  $\square$ 

**Lemma 2.3.6.** The map  $\varepsilon^{-1}: \Sigma_{ext}C \to \mathcal{M}$ , where  $\varepsilon_x = \delta_x$  is the Dirac measure, from a maximal ideal of the external spectrum  $\Sigma_{ext}C$  of the Calkin algebra C, to a point in the manifold  $\mathcal{M}$  is continuous.

*Proof.* The argument is the same with the one in Lemma 2.3.5 applied to  $[f] \in \mathcal{C}$  instead of  $\sigma(D) \in S$ , and with the density argument:

For any  $[f] \in \mathcal{C}$  and given  $\varepsilon > 0$ , there exists an operator  $D \in \mathcal{D}$  approximating [f] within  $\mathcal{C}$ , such that  $||[f] - [D]||_{\mathcal{C}} < \varepsilon/3$ . This utilizes the density of  $\mathcal{D}$  in  $\tilde{\mathcal{A}}$  [D0].

**Lemma 2.3.7.** The commutative structure of the differential operators algebra  $\mathcal{D}$  is preserved in the algebra of principal symbols S.

*Proof.* By contradiction, assume the commutative structure of  $\mathcal{D}$  is not preserved in S. This would imply a failure in the commutative properties' transition from  $\mathcal{D}$  to S.

Commutative Structure of  $\mathcal{D}$ . The commutative properties of  $\mathcal{D}$  with respect to operations involving  $C^{\infty}(\mathcal{M})$  are detailed in [L0]. The overall architecture of  $\mathcal{D}$  mirrors these local commutative behaviors, supported by an order-based filtration ([D1]) and reinforced by employing a partition of unity along with the choice of invertible pseudodifferential operators to avoid topological obstructions ([D3]).

Preservation of Commutativity in S. Through the monomorphism [M1], local principal symbols  $\sigma_x(D)$  are systematically connected to S, preserving local commutative structures globally. The relationship between  $\sigma_x(D)$  and  $D_x$  ([T1]) extends commutative properties from local to global contexts within S.

Contradiction and Conclusion. The mechanisms ensuring the preservation of commutativity from  $\mathcal{D}$  through S, as outlined by the structured mapping [M1], contradict the assumption of disrupted commutative structures. Therefore, the commutative structure within  $\mathcal{D}$  is indeed preserved in the algebra of principal symbols S.  $\square$ 

**Lemma 2.3.8.** The commutative structure of the differential operators algebra  $\mathcal{D}$  is preserved in the Calkin algebra  $\tilde{\mathcal{A}}/(\mathcal{K}\cap\tilde{\mathcal{A}})$ .

*Proof.* By contradiction, assume the commutative structure of  $\mathcal{D}$  is not preserved in the Calkin algebra. However, by Lemma 2.3.7 the commutative structure within  $\mathcal{D}$  is preserved in the algebra of principal symbols S. Hence, the mechanism ensuring commutativity's preservation from  $\mathcal{D}$  through S, and by [A3], to the Calkin algebra, contradict the assumption of disrupted commutative structures. Therefore, the commutative structure within  $\mathcal{D}$  is indeed preserved in the Calkin algebra,  $\tilde{\mathcal{A}}/(\mathcal{K}\cap\tilde{\mathcal{A}})$ .  $\square$ 

**Lemma 2.3.9.** The algebra of principal symbols S, associated with the differential operators on the manifold  $\mathcal{M}$ , satisfies the Ascending Chain Condition (ACC).

*Proof.* By contradiction, assume that S does not satisfy the ACC. This implies the existence of an infinite ascending sequence  $\{I_n\}$  of ideals in S that does not stabilize, i.e.  $I_n \subset I_{n+1}$  for all n and  $I_n \neq I_{n+1}$ .

Local Boundedness of  $D_x$ . According to [S1], for each x in  $\mathcal{M}$ , the operational impact of  $D_x$  is bounded due to scaling transformations, indicating that differential operators exhibit locally bounded complexity.

Transition of Boundedness from  $D_x$  to  $\sigma_x(D)$ . The monomorphism [T1] illustrates that each local principal symbol  $\sigma_x(D)$  directly correlates to the bounded limit  $D_x$ , implying that the complexity of  $\sigma_x(D)$  is similarly bounded at each point on  $\mathcal{M}$ .

Connection of Local Symbols  $\sigma_x(D)$  to Global S. Through the monomorphism [M1], local principal symbols  $\sigma_x(D)$  are systematically linked to their global counterparts within S, ensuring the transfer of local bounded complexity to the algebra of principal symbols S.

Implication of Filtration on Global D and S. The filtration of  $\mathcal{D}$  as detailed in [D1] not only organizes differential operators by their order but also enables the translation of local boundedness observed through  $D_x$  and  $\sigma_x(D)$  to a structured complexity within the global framework of  $\mathcal{D}$  and subsequently to S. This global structure of  $\mathcal{D}$ 's structure is further ensured through the utilization of a partition of unity and circumventing topological obstruction by selection of invertible pseudodifferential operators ([D3]).

Contradiction and Conclusion. The inherent bounded complexity of symbols

in S implies that any ascending chain of ideals in S must stabilize, contradicting the initial assumption. Therefore, S must satisfy ACC.  $\square$ 

**Lemma 2.3.10.** The Calkin algebra  $C = \tilde{\mathcal{A}}/(K \cap \tilde{\mathcal{A}})$  satisfies the Ascending Chain Condition (ACC).

*Proof.* By contradiction, assume that the Calkin algebra C does not satisfy the ACC, leading to an infinite ascending chain of ideals  $\{I_n\}$ .

Monomorphism and ACC in S. By [A3],  $\tilde{\sigma}$  creates a one-to-one correspondence between ideals in the Calkin algebra and S, preserving their structural and relational properties. Since S satisfies the ACC by Lemma 2.3.9, every ascending chain of ideals stabilizes.

Contradiction and Conclusion. The infinite ascending chain  $\{I_n\}$  in  $\tilde{\mathcal{A}}/(\mathcal{K}\cap\tilde{\mathcal{A}})$  would correspond to a similar chain in S through  $\tilde{\sigma}$ , contradicting S's ACC property. The contradiction confirms our initial assumption is false; therefore, the Calkin algebra must satisfy the ACC.  $\square$ 

**Lemma 2.3.11.** The Calkin algebra C is a generic algebra, i.e. the embedding  $\varepsilon : \mathcal{M} \to \Sigma_{ext} C$ , where  $\varepsilon_x = \delta_x$  is the Dirac measure, exists and is a homeomorphism, and the Gelfand transform of C can be given explicitly.

*Proof.* The Calkin algebra is eligible for application of the paper [40] on construction of Gelfand transform for noncommutative  $C^*$  algebras, as it contains commutative subalgebras by Lemma 2.3.8 and it satisfies the Ascending Chain Condition by Lemma 2.3.10.

The one-to-one correspondence between points on  $\mathcal{M}$  and maximal ideals in the external spectrum of the Calkin algebra  $\mathcal{C}$  is given by Lemma 2.3.2. The continuity of the embedding  $\varepsilon$  and its inverse  $\varepsilon^{-1}$  is given by Lemmas 2.3.4 and 2.3.6, respectively.

The link between external and internal spectrum as given in [40] allows for the explicit construction of Gelfand transform.  $\Box$ 

**Lemma 2.3.12.** The algebra S of principal symbols is a generic algebra, i.e. the embedding  $\varepsilon : \mathcal{M} \to \Sigma_{ext} S$ , where  $\varepsilon_x = \delta_x$  is the Dirac measure, exists and is a homeomorphism.

*Proof.* The one-to-one correspondence between points on  $\mathcal{M}$  and maximal ideals in the external spectrum of algebra S are given by Lemma 2.3.1.

The continuity of the embedding  $\varepsilon$  and its inverse  $\varepsilon^{-1}$  are given by Lemmas 2.3.3 and 2.3.5, respectively.  $\square$ 

**Lemma 2.3.13.** The coordinatization of the manifold can be given via the Gelfand transform of the Calkin algebra.

*Proof.* By Lemmata 2.3.11 and 2.3.12 the manifold is homeomorphic to the external spectrum of the Calkin algebra and the external spectrum of the algebra of principal symbols S, respectively. Hence, the external spectrum of the Calkin algebra and the external spectrum of S are also homeomorphic. Given that, as S is not eligible for an internal spectrum, whereas the Calkin algebra can support both internal and external spectral analysis, we will use the Calkin algebra for coordinatizing the manifold by its Gelfand transform.  $\square$ 

Lemma 2.3.14. Given two exact and splitting sequences

$$0 \to J1^m_{\gamma} \to A1^m_{\gamma} \to O1^m \to 0, \tag{2.3}$$

$$0 \to J2_{\gamma}^m \to A2_{\gamma}^m \to O2^m \to 0, \tag{2.4}$$

and the isometric isomorphism  $\phi: J1^m_{\gamma} \to J2^m_{\gamma}$ , then  $O1^m$  is isometrically isomorphic to  $O2^m$ .

*Proof*: We can express  $A1_{\gamma}^{m}$  and  $A2_{\gamma}^{m}$  as direct sums due to the exactness and splitting of the sequences:

$$A1_{\gamma}^{m} = J1_{\gamma}^{m} \oplus O1^{m}, \tag{2.5}$$

$$A2_{\gamma}^{m} = J2_{\gamma}^{m} \oplus O2^{m}. \tag{2.6}$$

Define a mapping  $\psi: A1^m_{\gamma} \to A2^m_{\gamma}$  where  $\psi(j,o) = (\phi(j),o)$  for any  $(j,o) \in A1^m_{\gamma}$ . This map  $\psi$  is constructed to maintain the structural relationship between  $A1^m_{\gamma}$  and  $A2^m_{\gamma}$ .

To verify  $\psi$  as an isometric isomorphism, we check for linearity, injectivity, surjectivity, and isometry:

- 1. Linearity:  $\psi$  respects vector addition and scalar multiplication, given its operation on each component of the direct sum.
- 2. Injectivity: Assume  $\psi(j_1,o_1) = \psi(j_2,o_2)$ . This leads to  $(\phi(j_1),o_1) = (\phi(j_2),o_2)$ . Given  $\phi$  is an isomorphism, we deduce  $j_1 = j_2$  and thus  $(j_1,o_1) = (j_2,o_2)$ , proving injectivity.
- 3. Surjectivity: For any  $(j_2,o_2) \in A2_{\gamma}^m$ , there exists  $(j_1,o_2) \in A1_{\gamma}^m$  such that  $\psi(j_1,o_2) = (\phi(j_1),o_2) = (j_2,o_2)$ , indicating surjectivity.
- 4. Isometry: Since  $\phi$  is an isometry between  $J1_{\gamma}^{m}$  and  $J2_{\gamma}^{m}$ , preserving inner product structures, the mapping  $\psi$ , defined as  $\psi(j,o)=(\phi(j),o)$ , naturally extends this isometry to  $A1_{\gamma}^{m}$  and  $A2_{\gamma}^{m}$ . By applying  $\phi$  to the J component and directly transferring the O component,  $\psi$  maintains the inner product relations intact across the entire structure.

Since  $\psi$  and  $\phi$  are isometric isomorphisms between  $Ai_{\gamma}^{m}$ 's and  $Ji_{\gamma}^{m}$ 's, i=1,2, then  $Oi^{m}=Ai_{\gamma}^{m}/Ji_{\gamma}^{m}$ , i=1,2 are isometrically isomorphic.  $\Box$ 

#### 2.3.1.3 Proof of Theorem 2.1.1

We consider two manifolds  $\mathcal{M}_i$ , i = 1, 2 with the same boundary and same boundary data, i.e. having the same Dirichlet-to-Neumann map.

1. On the two manifolds  $\mathcal{M}_i$ , i=1,2, let us consider the following direct BVPs  $P_i=\begin{pmatrix}A\\B_i\end{pmatrix}$ , for i=1,2, where A is our elliptic operator,  $B_1$  is the boundary condition with the input data of the inverse problem, i.e the Dirichlet data, and  $B_2$  corresponds to the output data, i.e. the Neumann data, connected by the given Dirichlet-to-Neumann map  $\Lambda$  which the two manifolds share.

This is meaningful, as in the static context of elliptic inverse BVPs, both the input (Dirichlet) and output (Neumann) boundary data are snapshots of the steady

state, not states in a temporal evolution. Hence, using the output data as boundary conditions for a conceptual direct problem does not inherently involve reverse engineering in a temporal sense, because the data does not inherently possess a "direction" of propagation; unlike the dynamic, time-evolving problem.

- **2.** We will treat the elliptic BVPs  $P_i$ , i=1,2, as edge problems, where the edge is the boundary and the cone degenerates to  $\mathbb{R}_+$ , interpreted as the inner normal. By [EM1] an operator A and its edge morphism have the same interior symbol, i.e.  $\sigma(Ai) = \mathcal{O}_i$ , i=1,2, where  $Ai \in \text{Mor}_{\gamma}^0$ , and  $\mathcal{O}_i$ , i=1,2 denote the interior symbols of the operator A for the corresponding manifold (they are determined by the manifold).
- **3.** From [46], Section 3.1.2, Proposition 3 and the comments following it, we get

**Proposition 2.3.15.** ([46]) The operator  $Z = F_{\eta \to y}^{-1} \kappa^{-1}(\eta) F_{y \to \eta}$ , where  $\kappa$  is a continuous groups with the strong operator topology, defines an isometric isomorphism

$$Z: \mathcal{W}^s(\mathbb{R}^q, E) \to H^s(\mathbb{R}^q, E).$$
 (2.7)

 $\mathcal{W}^s$  is the abstract wedge space defined in [E1], which is equivalent to the boundary in our case.

Also wedge spaces modelled by  $\{E, \kappa_{\lambda}\}, \{E, \tilde{\kappa}_{\lambda}\}$  are isomorphic for any choice of continuous groups with the strong operator topology. If

$$\tilde{Z}: \mathcal{W}^s(\mathbb{R}^q, E) \to H^s(\mathbb{R}^q, E)$$

is the isomorphism of Proposition 2.3.15 related to  $\tilde{\kappa}_{\lambda}$ , then we get the isometric isomorphism

$$\tilde{Z}^{-1}Z: \mathcal{W}^s(\mathbb{R}^q, E) \to \tilde{\mathcal{W}}^s(\mathbb{R}^q, E).$$

Given the isometric isomorphism between the abstract wedge spaces  $W^s(R^q,E)$  and  $\widetilde{W}^s(R^q,E)$  established through this specific isomorphism  $\widetilde{Z}^{-1}Z$ , the edge symbols  $D(x;\xi)$  on  $K^s_{\gamma}(K_{\Omega})$  and  $\widetilde{D}(x;\xi)$  on  $\widetilde{K}^s_{\gamma}(K_{\Omega})$  are isometrically isomorphic. This is

because as stated in [E1]  $K_{\gamma}^{s}(K_{\Omega})$  is an adaptation of  $W^{s}(R^{q}, E)$  with  $E = K_{\Omega}$  to specific geometric configurations, i.e. cones, and both sets of spaces serve analogous roles in the context of edge-degenerate operators and their symbol calculus (in particular, these spaces define the domains and codomains for the operators, and their transformations are dictated by similar structural and functional principles).

- **4.** Applying Lemma 2.3.14 for sequences described in [Q1], and using 3. we conclude that the interior symbols of the manifolds are isometrically isomorphic.
- **5.** By Lemma 2.3.13 the coordinatization of the manifold can be given via the Gelfand transform of the Calkin algebra.

Hence, the two manifolds are isometrically isomorphic.  $\Box$ 

#### 2.3.2 Proof on BC for parabolic problems

#### 2.3.2.1 Facts to be used in the proof

All definitions/facts included in the following itemized list are from [43].

Parabolic Symbols and Volterra Operators

- [P1] A symbol  $a \in S_V^{\mu;\ell}(\mathbb{R}^n \times \mathbb{R}^n \times \mathbb{H}; E, \tilde{E})$  is parabolic if it demonstrates parameter-dependent ellipticity within  $S^{\mu;\ell}(\mathbb{R}^n \times \mathbb{R}^n \times \mathbb{H}; E, \tilde{E})$ , ensuring crucial analytical properties over  $\mathbb{H}$  necessary for temporal dynamics in parabolic differential equations. Here,  $\mu$  denotes the order,  $\ell$  the degree of homogeneity, and  $E, \tilde{E}$  represent Hilbert spaces.
- [P2] A Volterra operator  $A(\lambda) \in L_{V(cl)}^{\mu;\ell}(X;\mathbb{H};E,F)$  qualifies as parabolic when it satisfies parameter-dependent ellipticity within  $L_{(cl)}^{\mu;\ell}(X;\mathbb{H};E,F)$ . This class of operators, emerging from symbols exhibiting the Volterra property, is specialized for equations typified by temporal parameters, aligning with parabolic equation characteristics.
- [P3] The sequence of principal symbols for Volterra operators is exact and splits as follows:

$$0 \to L_{V\ cl}^{\mu-1;\ell}(X;\mathbb{H};E,F) \xrightarrow{\iota} L_{V\ cl}^{\mu;\ell}(X;\mathbb{H};E,F) \xrightarrow{\sigma_{\psi}^{\mu;\ell}} S_{V}^{(\mu;\ell)}((T^{*}X \times \mathbb{H}) \setminus 0,\ \operatorname{Hom}(\pi^{*}E,\ \pi^{*}F)) \to 0$$

Here,  $\sigma_{\psi}^{\mu;\ell}$  denotes the principal symbol,  $\pi^*$  refers to the pull-back associated with the projection  $\pi$ , and  $S_V^{(\mu;\ell)}$  represents the space of anisotropic homogeneous functions of degree  $\mu$  that are analytic within  $\mathbb{H}$ .

#### 2.3.2.2 Proof on Theorem 2.1.2

Through [P1] and [P2] Volterra operators' parabolicity is linked with parameter-dependent ellipticity, hence we resort to the solution for inverse elliptic BVPs in Section 2.3.1.3. Theorem [P3] is required at step 4 to ensure that symbols are isomorphic to the Calkin algebra of the operators. □

#### 2.4 The Calderon Problem

While the edge calculus contains all "standard" elliptic BVPs for differential operators, the result holds as long as there is no obstruction to ellipticity. Obstruction to ellipticity is expressed as obstruction to the existence of Fredholm problems for a given operator, or equivalently as obstruction to the existence of Fredholm operators with a given interior symbol. It often happens that even though the interior symbol of an edge-degenerate operator is elliptic, the edge symbol is not invertible and the operator fails to be Fredholm. For the edge problem corresponding to the Calderon problem we will create a new edge symbol, by adding some "boundary and "coboundary" operators concentrated at the edge, which will offer to the edge symbol maximum domain of invertibility.

#### **2.4.1 Proof of Theorem 2.1.3**

Finding out the cases for which the edge problem for the Calderon problem can be made Fredholm, indicates the cases for which the uniqueness argument of section 2.3.1.3 applies. The following Lemma directly makes use of the analysis of [43], Section 6.1.1 for Fredholmness of the Laplace operator, as it turns out the problem is essentially reduced to that of the Laplacian for  $\sigma \neq 0$  and locally flat near the boundary manifold.

Lemma 2.4.1. The operator Cald corresponding to the multidimensional Calderon

problem on a manifold  $\mathcal{M}$ 

$$Cald \equiv div(\sigma \nabla) : \mathcal{W}^{s,\gamma}(\mathcal{M}) \to \mathcal{W}^{s-2,\gamma-2}(\mathcal{M}),$$

where  $\sigma$  is the conductivity, can be made Fredholm through conversion to an edge problem via addition of boundary and coboundary operators, for  $\gamma \neq \frac{1}{2}, \frac{3}{2}$ .

Proof.

1. Operator expressed in local coordinates. Consider local coordinates  $x = (r, x_1, x_2, ..., x_{n-1})$  near the boundary, with r normal to the boundary and  $x_i$  tangential. The Calderón operator in local coordinates is:

$$\operatorname{div}(\sigma(x)\nabla u) = \frac{1}{\sqrt{|g|}} \partial_i \left( \sqrt{|g|} g^{ij} \sigma(x) \frac{\partial u}{\partial x_j} \right)$$

Suppose the manifold is locally flat near the boundary, which means simplifying the metric tensor to approximately an identity matrix; hence,  $g_{ij} \approx \delta_{ij}$  and  $|g| \approx 1$ . Under this assumption, the Calderón operator can be simplified to:

$$\operatorname{div}(\sigma(x)\nabla u) \approx \frac{\partial}{\partial r} \left(\sigma(x)\frac{\partial u}{\partial r}\right) + \sum_{i=1}^{n-1} \frac{\partial}{\partial x_i} \left(\sigma(x)\frac{\partial u}{\partial x_i}\right)$$

where the divergence and gradient are reduced to their Euclidean forms.

2. Edge symbol of the operator. The edge symbol for an operator is derived by applying a Fourier transform to the tangential derivatives of the operator in local coordinates. As a pseudodifferential operator, the edge symbol is primarily concerned with capturing the leading-order behavior of the operator, particularly in a high-frequency domain; hence, as mixed derivatives do not contribute to the highest-order terms in this context, the focus is on pure higher-order derivatives.

Therefore, in the Fourier-transformed space, the edge symbol of the operator Cald becomes

$$\sigma_{\wedge}(\operatorname{Cald})(\xi) = \sigma(x)(\frac{\partial^2}{\partial r^2} - \|\xi\|^2),$$

where  $\|\xi\|^2=\xi_1^2+\xi_2^2+\ldots+\xi_{n-1}^2$  is a multi-dimensional frequency variable, with

 $\xi_i$  the Fourier dual variables corresponding to the tangential coordinates  $x_i$ .

Hence, the foundational structure of the edge symbol corresponding to the Calderón problem retains a consistent format regardless of the specific form of conductivity  $\sigma(x)$ , be it constant, linear, radial, polynomial, harmonic, exponential, etc.

3. Adjoint operator of the edge symbol. For test functions  $f,g \in C_0^{\infty}(\mathbb{R}_+ \times \mathbb{R}^{n-1})$ , we apply integration by parts, focusing on the radial derivative:

$$\int_{\mathbb{R}_{+}\times\mathbb{R}^{n-1}} \sigma(x) f \cdot \left( \frac{\partial^{2} g}{\partial r^{2}} - \sum_{i=1}^{n-1} \xi_{i}^{2} g \right) dr d\mathbf{x} = -\int_{\mathbb{R}_{+}\times\mathbb{R}^{n-1}} \sigma(x) \frac{\partial f}{\partial r} \cdot \frac{\partial g}{\partial r} dr d\mathbf{x}$$

The adjoint calculation involves 'reversing' the differential operation in the radial direction while keeping the tangential frequency components:

$$-\int_{\mathbb{R}_{+}\times\mathbb{R}^{n-1}} \sigma(x) \frac{\partial f}{\partial r} \cdot \frac{\partial g}{\partial r} dr d\mathbf{x} = \int_{\mathbb{R}_{+}\times\mathbb{R}^{n-1}} \sigma(x) \left( \frac{\partial^{2} f}{\partial r^{2}} - \sum_{i=1}^{n-1} \xi_{i}^{2} f \right) \cdot g dr d\mathbf{x}$$

This equation suggests that the adjoint family

$$\sigma_{\wedge}(Cald)(\xi)^*: \mathcal{K}^{2-s,2-\gamma}(\mathbb{R}_+) \to \mathcal{K}^{-s,-\gamma}(\mathbb{R}_+),$$

on  $C_0^\infty(\mathbb{R}_+)$  retains the same structure as the original edge symbol  $\sigma_\wedge(\operatorname{Cald})(\xi)$ .

4. *Homogeneity of the edge symbol*. To study the invertibility of the edge symbol in the spaces

$$\sigma_{\wedge}(\mathrm{Cald})(\xi): \mathcal{K}^{s,\gamma}(\mathbb{R}_+) \to \mathcal{K}^{s-2,\gamma-2}(\mathbb{R}_+),$$

it suffices to study the invertibility of  $\sigma_{\wedge}(\Delta)(\xi)$  at the normalized scale  $|\xi|=1$ , and then extend the result to all  $\xi \neq 0$  across the entire domain by scaling, due to the principle of homogeneity of the edge symbol.

5. Kernel and cokernel of the edge symbol. The kernel of the edge symbol is

$$\sigma_{\wedge}(\operatorname{Cald})(\xi)u = \sigma(x)(\frac{\partial^2 u}{\partial r^2} - \sum_{i=1}^{n-1} \xi_i^2 u) = 0.$$

For the case of spatially varying conductivity  $\sigma(x) \neq 0$  we get the equation

$$\frac{\partial^2 u}{\partial r^2} - \sum_{i=1}^{n-1} \xi_i^2 u = 0.$$

whose general solution is:

$$u(r,\xi_1,\xi_2,\ldots,\xi_{n-1}) = C_1 e^{r\sqrt{\sum_{i=1}^{n-1}\xi_i^2}} + C_2 e^{-r\sqrt{\sum_{i=1}^{n-1}\xi_i^2}}.$$

To be part of the kernel, the solution u must be integrable over  $\mathbb{R}_+$ . Given that the term  $e^{r\sqrt{\sum_{i=1}^{n-1}\xi_i^2}}$  grows exponentially as r increases (particularly for  $\sum_{i=1}^{n-1}\xi_i^2\neq 0$ ), integrability requires that the coefficient  $C_1$  associated with this term must be zero to prevent the function from becoming unbounded as  $r\to\infty$ . Therefore, the kernel for the Calderón problem's edge symbol has a one-dimensional kernel spanned by

$$u = e^{-|\xi|r}. (2.8)$$

Cokernel, i.e. the kernel of the adjoint edge symbol,

$$\sigma_{\wedge}(\Delta)(\xi)^*:\mathcal{K}^{2-s,2-\gamma}(\mathbb{R}_+)\to\mathcal{K}^{-s,-\gamma}(\mathbb{R}_+),$$

is also spanned by  $e^{-|\xi|r}$ .

The norm  $\mathcal{K}^{s,\gamma}(\mathbb{R}^n)$  of a function u is defined as

$$||u||_{\mathcal{K}^{s,\gamma}} = \left(\sum_{|\alpha| \leq s} \int_{\mathbb{R}^n} r^{-2\gamma} |D^{\alpha}u|^2 dr d\xi\right)^{1/2},$$

where  $D^{\alpha}$  represents derivatives up to order s with respect to both the radial variable r and the angular variables  $\xi$  within the multi-index  $\alpha$ . To avoid singularities at r=0, the combined exponent on r from  $r^{-2\gamma}$  and the derivatives should be greater than -1. Hence, for the function  $u(r, \xi_1, \dots, \xi_{n-1}) = e^{-r|\xi|}$ , the integral's convergence relies on the term

$$\int_{\mathbb{D}^n} r^{-2\gamma} r^k |\xi|^k e^{-2r|\xi|} dr d\xi,$$

where k is the degree of r in  $D^{\alpha}u$ . Therefore the condition  $k-2\gamma>-1$  must hold for the smallest k (i.e., k=0), thus

$$\gamma < \frac{1}{2}$$
.

Hence, the presence of the weight factor  $r^{-2\gamma}$  in the definition of the norm in  $\mathcal{K}^{s,\gamma}(\mathbb{R}_+)$  results in the assertion that  $e^{-r} \in \mathcal{K}^{s,\gamma}(\mathbb{R}_+)$  if and only if  $\gamma < \frac{1}{2}$ .

On the other hand, for the function  $u(r, \xi_1, \dots, \xi_{n-1}) = e^{-r|\xi|}$ , the convergence of  $||u||_{\mathcal{K}^{2-s,2-\gamma}}$  relies on the term

$$\int_{\mathbb{R}^n} r^{-2(2-\gamma)+k} |\xi|^{2k} e^{-2r|\xi|} dr d\xi,$$

where k is the degree of r in  $D^{\alpha}u$ . Therefore the condition  $-2(2-\gamma)+k>-1$  must hold for the smallest k (i.e., k=0), thus

$$\gamma > \frac{3}{2}$$
.

Hence, the presence of the weight factor  $r^{-2(2-\gamma)}$  in the definition of the norm in  $\mathcal{K}^{2-s,2-\gamma}(\mathbb{R}_+)$  results in the assertion that  $e^{-r|\xi|} \in \mathcal{K}^{2-s,2-\gamma}(\mathbb{R}_+)$  if and only if  $\gamma > \frac{3}{2}$ .

As a result of the above, we conclude that:

- Case 1 If  $\gamma < \frac{1}{2}$ , then  $\sigma_{\wedge}(\text{Cald})(\xi)$  has the one-dimensional kernel spanned by the function (2.8) and the trivial cokernel.
- Case 2 If  $\gamma > \frac{3}{2}$ , then  $\sigma_{\wedge}(\text{Cald})(\xi)$  has the trivial kernel and the one-dimensional cokernel spanned by the function (2.8).
- Case 3 If  $\frac{1}{2} < \gamma < \frac{3}{2}$ , then  $\sigma_{\wedge}(\text{Cald})(\xi)$  is invertible, satisfying both injectivity (trivial kernel) and surjectivity (trivial cokernel) conditions.
- Case 4 If  $\gamma = \frac{1}{2}$  or  $\gamma = \frac{3}{2}$ , then  $\sigma_{\wedge}(\text{Cald})(\xi)$  is not Fredholm. In particular, for  $\gamma = 1/2$  or (3/2), small alterations on functions belonging to  $\mathcal{K}^{s,\gamma}(\mathbb{R}^n)$  might lead to large deviations onto their images under the edge symbol, causing unexpected

limit infinities outside the range; thus the requirement for a closed range is not satisfied.

6. We want to make our edge symbol invertible, i.e. make the equation

$$\sigma_{\wedge}(\operatorname{Cald})(\xi)v = F$$
 (2.9)

uniquely solvable by putting finitely many conditions on the solution or the right-hand side. This is obviously impossible for the non-closed range case 4 (because the limit of a converging sequence in the domain might map to an element outside the range, making it impossible to uniquely link elements in the target space back to the domain), and we will deal only with cases 1 and 2.

6a. *Case 1*: Integral condition for Unique Solvability for  $\gamma < \frac{1}{2}$ .

The point is to restrict the solution space. For example, a global constraint over the whole solution space, determines the integral condition

$$B(\xi)v \equiv \int_0^\infty \phi(|\xi|r)v(r)dr = g \in \mathbb{C},\tag{2.10}$$

where  $\phi(|\xi|r) \in C_0^{\infty}(\mathbb{R}+)$  is not orthogonal to  $e^{-r\sqrt{\sum i=1^{n-1}\xi_i^2}}$ .

The non-orthogonality uniquely imposes a scalar constraint, ensuring that solutions v(r) are solely scalar multiples c of the kernel function. Thus it guarantees the equation's unique solvability within the kernel by preventing any arbitrary function from trivially satisfying it, thereby directly linking each solution v(r) to a unique scalar c that corresponds with a given g. Hence, the integral condition becomes a scalar equation for c, and essentially effectively reduces the infinite-dimensional solution space to a singular dimension defined by a specific scalar  $c \in \mathbb{C}$ .

To show uniqueness, let  $v_1(r)$  and  $v_2(r)$  be two solutions of the integral condition for the same g. The difference  $v_d(r) = v_1(r) - v_2(r)$  is a solution of the homogeneous integral condition. As  $v_1(r)$  and  $v_2(r)$  are of the form of a scalar multiplied by the kernel function  $e^{-|\xi|r}$ , then so is  $v_d(r)$ . As  $\phi(r)$  is not orthogonal to the kernel function, then  $v_d(r)$  is identically zero, i.e.  $v_1(r) = v_2(r)$ .

6a.i. Edge problem by quantization for Cald. The symbol of the Laplace-

Beltrami operator is quantized by smoothing near  $\xi=0$  (to ensure that the operator behaves well, even at low frequencies or near the "edges" of the domain) and replacing the multidimensional frequency vector  $\xi$  with the corresponding multidimensional differentiation operator  $-i\frac{\partial}{\partial x}$ , obtaining the following edge problem for Cald operator for  $\gamma<\frac{1}{2}$ :

$$\begin{cases} \operatorname{Cald} u = f, \\ Bu \equiv \int_0^\infty \phi(r[-i\frac{\partial}{\partial x}])u(x)dr = g(x). \end{cases}$$
 (2.11)

6a.ii. Estimates for Cald.

In what spaces will this problem be Fredholm? The spaces in which Cald acts are clear, and we only need to find the natural space into which the edge boundary operator *B* acts. Namely, by Theorem 3.32 of [43]

$$B(\xi) \in S_{CV}^0(\bullet_1, \bullet_2),$$

where  $S_{CV}^0$  is the space of symbols of compact fiber variation, and  $ullet_1$  is the space  $\mathcal{K}^{s,\gamma}(\mathbb{R}_+)$  equipped with the family of norms  $\|\cdot\|_{\xi} = \||\xi|^s \kappa_{|\xi|}^{-1} \cdot \|_{\mathcal{K}^{s,\gamma}(\mathbb{R}_{\bullet})}$  and  $ullet_2$  is the one-dimensional complex space  $\mathbb{C}$  equipped with the family of norms  $\|\cdot\|_{\xi} = |\xi|^{s+1/2}|\cdot|$ .

By [43], Theorem 3.32, the operator B acts continuously in the spaces

$$B: \mathcal{W}^{s,\gamma}(M) \to H^{s+1/2}(X), X = \partial M.$$

6a.iii. *Edge problem and Fredholmness for Cald*. Hence, the operator A corresponding to our edge boundary value problem acts in the spaces

$$A = \begin{pmatrix} \Delta \\ B \end{pmatrix} : \mathcal{W}^{s,\gamma}(M) \to \bigoplus . \tag{2.12}$$

$$H^{s+1/2}(X)$$

This operator is Fredholm; this follows from the general finiteness theorem [43],

Theorem 6.19.

6b. *Case 1*: Condition for Unique Solvability for  $\gamma > \frac{3}{2}$ .

To make Eq. (2.9) uniquely solvable, one can equip it, say, with a co-condition including a numerical unknown  $\mu \in \mathbb{C}$ :

$$\sigma_{\wedge}(\Delta)(\xi)v + \mu\phi(|\xi|r) = F, \tag{2.13}$$

where  $\phi$  is the same function as above.

6b.i. Quantizing, we obtain the problem

$$\Delta u + Cw = f, \tag{2.14}$$

where the operator C is given by the formula

$$Cw = \phi \left( r \left[ -i \frac{\partial}{\partial x} \right] \right) w.$$

6b.ii. A similar argument shows that the operator A corresponding to this edge coboundary value problem acts in the spaces

$$\mathcal{W}^{s,\gamma}(M)$$

$$A = (\Delta C): \oplus \to \mathcal{W}^{s-2,\gamma-2}(M). \tag{2.15}$$

$$H^{s-5/2}(X)$$

#### **Chapter 3**

### Polyhedral reconstruction via Boundary Control method

We study uniqueness of an elliptic Riemannian polyhedron using the elliptic version for Boundary Control method, which we presented in Chapter 2. We also present interface detection criteria for hyperbolic Riemannian manifolds through introduction of the waveguide notion, the four-wave mixing notion, etc.

#### 3.1 Introduction

In continuation of the work [49] where a uniqueness argument via Boundary Control (BC) method for a hyperbolic Riemannian polyhedron was presented, we proceed to uniqueness argument of an elliptic Riemannian polyhedron, by extending the elliptic version for Boundary Control (BC) method, which we presented in Chapter 2, i.e. extending the pseudodifferential cone and edge singularities algebra that were used there.

The category of manifolds with singularities, denoted as  $\mathfrak{M}_k$ , includes  $\mathfrak{M}_0$  for  $C^{\infty}$  manifolds and progresses to higher orders representing more complex singularities, such as conical or edge singularities. This hierarchy allows for the definition of  $\mathfrak{M}_{k+1}$  manifolds iteratively from  $\mathfrak{M}_k$ . Manifolds within  $\mathfrak{M}_k$  support a natural differential operators algebra, characterized by principal symbolic hierarchies and ellipticity concepts. Prior research, including [50], [51], and [52], illustrates that advancing from level k to k+1 in manifold analysis entails leveraging the parameter-

dependent calculus of the preceding level, enriched by index theory and additional insights, challenging the notion of a simple inductive approach from k to k+1. This complexity necessitates a detailed examination beyond mere induction, as suggested by [53]. Hence, we prove

**Theorem 3.1.1.** The BC method can provide a uniqueness argument for an elliptic Riemannian polyhedron.

Furthermore, for the reconstruction of hyperbolic Riemannian polyhedron problem, we use the reconstruction per compartment choice; hence we resort to papers solving the problem in smooth manifolds, and we add interface and vertex detection conditions in the case of different wave types and different media. For interface detection we try to find a condition equivalent to Snell's law but for perpendicular interface incidence.

Hence, we show that

#### **Theorem 3.1.2.** For electromagnetic waves in isotropic dielectric media

- (i) The amplitude transmission and reflection coefficients constitute conditions for interface detection.
- (ii) Coupled mode equations constitute a vertex detection criterion.
- (iii) For polyhedron with multiple interfaces meeting at a vertex, the RC filter, i.e. a multi-directional coupler, can constitute a vertex detection criterion.

**Theorem 3.1.3.** For electromagnetic waves in anisotropic non-linear media, e.g. a crystal, the four-wave-mixing constitutes a vertex detection criterion.

#### **Theorem 3.1.4.** For acoustic waves in fluid media

- (i) the intensity transmission and reflection coefficients constitute conditions for interface detection.
- (ii) The directional coupler with multiple transmission line matrices constitutes a vertex detection condition.

## 3.2 Reconstruction of an Elliptic Riemannian Polyhedron

#### 3.2.1 Algebra description

The iterative construction of higher singularities. [53], Section 10.3.1.

In their work, Calvo, Martin, and Schulze [54] introduce the category  $\mathfrak{M}_k$  for singularity-ordered spaces. A space M is part of this category if it progressively subtracts submanifolds Y, starting from a non-singular manifold ( $\mathfrak{M}_0$ ), through to manifolds with singularities of order k-1. Specifically, for a space M to belong to  $\mathfrak{M}_k$ , it must, after excluding a submanifold Y, fall within  $\mathfrak{M}_{k-1}$ . Furthermore, the dimensions of Y indicate the nature of the singularity—zero dimensions imply a corner, while higher dimensions suggest an edge.

By deductive method, in [3] is established a hierarchy of  $C^{\infty}$  submanifolds  $Y^{(l)}$  within M, leading to a decomposition of M into a sequence where each  $M^{(j)}$  comprises submanifolds of decreasing singularity order, forming smooth edges of varying dimensions within M.

Adequate differential operators of order  $\mu$  for spaces within  $\mathfrak{M}_k$  are denoted by  $A \in \operatorname{Diff}_{\operatorname{deg}}^{\mu}(M)$ , and are uniquely characterized by their behavior on non-singular portions of M and near singular edges, with the latter described by a specialized formula involving the radial derivative and smooth coefficients.

The concept of a principal symbolic hierarchy  $\sigma(A)$  for these operators is introduced, capturing the traditional homogeneous principal symbol for non-singular parts of M and extending it across the singularity order spectrum to describe the behavior of A in relation to singular edges, culminating in a family of operators defined for the conical model space.

#### Higher generations of weighted corner spaces. [53], Section 10.5.1.

In the study of manifolds with complex singularities, the focus is on defining and understanding weighted Sobolev spaces, which are essential for modeling the manifold's geometric and analytic properties. These spaces, denoted as  $\mathcal{K}^{s,\gamma}(X^{\wedge})$  for

compact manifolds X within a set  $\mathfrak{M}_k$ , and  $\mathcal{W}^{s,\gamma}(X^{\wedge} \times \mathbb{R}^q)$ , serve to encapsulate the behaviors near singularities through the incorporation of weight tuples  $\gamma \in \mathbb{R}^k$ .

Manifolds M are connected through a hierarchy of subspaces  $M^{(j)}$ , transitioning from complex structures to more simplified ones, ultimately allowing for an analytical framework that accommodates the manifold's singular characteristics. The construction of weighted Sobolev spaces is iteratively defined, starting from standard Sobolev spaces for k=0 scenarios and extending to weighted cone and edge spaces for manifolds with conical singularities or smooth edges, respectively. These definitions rely on stretching the manifold to fit the model spaces, with  $\mathcal{H}^{s,\gamma}(\mathbb{M})$  and  $\mathcal{W}^{s,\gamma}(\mathbb{M})$  being particular instances.

A remarkable aspect of these spaces is their invariance under natural chart transformations, facilitating the application across various manifold settings. Moreover, the transition to analyzing manifolds by directly addressing their singular nature, rather than their stretched counterparts, simplifies the notation and theoretical underpinnings, as illustrated by replacing  $\mathcal{H}^{s,\gamma}(\mathbb{M})$  with  $\mathcal{H}^{s,\gamma}(M)$ .

The iterative process is further elucidated through the use of group isomorphisms, which underpin the local modeling near singular points and the seamless connection between local and global perspectives on the manifold. This leads to a comprehensive framework that not only addresses the manifold's inherent complexity but also provides a methodological basis for exploring weighted corner spaces in higher-dimensional settings.

Lastly, the theory accommodates both compact and non-compact manifolds, allowing for a broad application spectrum. This includes the consideration of manifolds as countable unions of compact sets and the introduction of spaces like  $\mathcal{H}^{s,\gamma}_{(\text{comp})}(M)$  and  $\mathcal{H}^{s,\gamma}_{(\text{loc})}(M)$ , which are tailored to handle the nuances of manifold structures with varying degrees of compactness.

#### Additional edge conditions in higher corner algebras. [53], Section 10.5.2.

As we saw in Chapter 2 to extend an elliptic operator *A* into a Fredholm operator across Sobolev spaces, formulating additional boundary conditions is essential, particularly by enhancing the boundary symbol into a set of isomorphisms. This may

necessitate introducing vector bundles  $J_{\pm}$  on the boundary, even for scalar operators, and applying to operators between distributional sections of vector bundles E and F to achieve Fredholm operators.

For manifolds with edges, an edge-degenerate operator A necessitates supplementing the principal edge symbol  $\sigma_{\wedge}(A)$  to transform it into a  $2 \times 2$  block matrix of isomorphisms for suitable vector bundles  $J_{\pm}$ . This process involves detailed constructions based on the bundles  $E_y$  and  $F_y$  derived from projecting vector bundles over the manifold's singularities and adjusting for admissible weights, which influence the choice of  $J_{\pm}$  bundles.

Operators are considered Fredholm when they meet ellipticity conditions related to the edge algebra, signified by the bijectivity of the augmented edge symbol for all off-zero cotangent vectors. The Fredholm operators are then represented as  $2 \times 2$  block matrices connecting Sobolev spaces associated with the manifold and its boundary, based on specific weight data and the bundles  $E, F, J_-$ , and  $J_+$ .

For manifolds featuring hierarchical structure, the focus shifts to weighted Sobolev spaces associated with each subspace, characterized by their respective weights and vector bundles. The formulation extends to higher corner operator spaces, which encompass operators of a specific order and are represented as block matrices acting on the amalgamated weighted Sobolev spaces. These operators' ellipticity, crucial for their classification as Fredholm operators, is affirmed through the hierarchical structure of their principal symbols, accommodating both the manifold's interior and its corners.

#### **3.2.2 Proof of Theorem 3.1.1**

Having created the extension for function spaces and symbols we use the method of Chapter 2 to prove the Theorem.  $\Box$ 

# 3.3 Interface and vertex detection conditions for hyperbolic Riemannian Polyhedron reconstruction

We give conditions of interface and vertex detection for the reconstruction of a polyhedron with BC method in the case of different wave types and different media.

#### 3.3.1 Prerequisite facts

#### 3.3.1.1 Riemannian polyhedron

We start with a closed *n*-dimensional finite simplicial complex

$$\mathcal{M} = igcup_{i=1}^I \Omega^{(i)},$$

where  $\Omega^{(i)}$  are closed *n*-dimensional simpleces of  $\mathcal{M}$ .

We assume that  $\mathcal{M}$  is dimensionally homogeneous, i.e. any k-simplex,  $0 \le k < n$ , of  $\mathcal{M}$  is contained in at least one  $\Omega^{(i)}$ . We assume also that any (n-1)-dimensional simplex  $\gamma$  belongs either to two different n simpleces,  $\Omega^{(i)}$  and  $\Omega^{(j)}$ , which, in this case, we often denote by  $\Omega_-$  and  $\Omega_+$ , or to one n simplex  $\Omega^{(i)}$ . In the former case we call  $\gamma$  an *interface* (sometimes (n-1)-dimensional interface) between  $\Omega_-$  and  $\Omega_+$ , in the latter case we call  $\gamma$  a *boundary* (n-1)-simplex, with (n-1)-simpleces having this property making the boundary  $\partial \mathcal{M}$ .

We denote by  $\mathcal{M}^k$ ,  $0 \le k \le n$ , the *k*-skeleton of  $\mathcal{M}$  which consists of all *k*-simpleces of  $\mathcal{M}$ , with the differential structure on each *k*-simplex determined by its barycentric coordinates. Clearly,  $\mathcal{M} = \mathcal{M}^n$ .

#### 3.3.1.2 Boundary Control (BC) method for hyperbolic problems

The Boundary Control method (BCm), as elaborated e.g. in [55], offers a three-step process to construct a manifold that matches given data, involving defining input and state spaces (F and H, respectively), an input/state map W, and an input/output map R that serves as the inverse data.

- 1. Coordinatization: Attach coordinates to each point in a manifold  $\Omega$ , derived from state space H, to create a metrically equivalent set  $\tilde{\Omega}$  based on reachable states and the mapping W.
- 2. *Model Construction*: Use data R to determine inner products in the input space F, leading to an auxiliary space  $\tilde{H}$  and mapping  $\tilde{W}$ , which together form a model isometric to the original system's controllable part.
- 3. Replication of  $\tilde{\Omega}$ : By mimicking the coordinatization step with model states, replicate  $\tilde{\Omega}$ , ensuring it is metrically and structurally identical to the original  $\Omega$ .

Our metric is non-smooth between the polyhedron compartments. However, by smoothing u with respect to time t, we can extend it to non-smooth solutions, see e.g. [56].

#### 3.3.2 Electromagnetic waves in isotropic dielectric media

The material of this section is from [57].

#### 3.3.2.1 Interface detection

We examine interactions of plane electromagnetic (EM) waves at the interfaces between two non-absorbing, isotropic, and homogeneous media. These media are characterized by their permittivity and permeability values denoted  $(\varepsilon_1, \mu_1)$  and  $(\varepsilon_2, \mu_2)$ , for media 1 and media 2 respectively. Let  $E_i$  and  $H_i$ , i = 1, 2, 3 be the electric and magnetic fields associated with the incident, the refracted, and the reflected waves, respectively. Let the incidence plane be the xz- plane. Let  $\theta_1, \theta_2$  and  $\theta_3$  be the angles of incidence, transmission/refraction, reflection, respectively, and  $k_1, k_2$  and  $k_3$  the propagation vectors along the incidence direction, the refracted direction and the reflected direction, respectively.

Wave polarization at these interfaces is categorized into: P-polarized waves, where the magnetic field  $\vec{H}$  is perpendicular to the incidence plane, also recognized as TM-polarized; and S-polarized waves, where the magnetic field lies within the incidence plane, hence termed TE-polarized. The amplitude transmission and reflection

coefficients for both TM- and TE-polarized waves are defined as

$$t = \frac{E_2}{E_1},\tag{3.1}$$

and

$$r = \frac{E_3}{E_1},\tag{3.2}$$

indicating the wave amplitude ratios.

A lemma pertaining to normal incidence reveals that the amplitude transmission and reflection coefficients for TE- and TM-polarized waves are given, respectively, by

$$r_p = r_s = \frac{n_1 - n_2}{n_1 + n_2},\tag{3.3}$$

and

$$t_p = t_s = \frac{2n_1}{n_2 + n_1},\tag{3.4}$$

where  $n_1$  and  $n_2$  are the refractive indices of the respective media. This demonstrates that, at normal incidence, the coefficients are unaffected by wave polarization.

**Proof of Theorem 3.1.2 (i).** Following a shortest geodesic, this will be normal to the interface from both of its sides. Hence we can recover waves up to a very small part past the interface. We test the recovered values to spot the ones which satisfy the amplitude reflection and transmission coefficients given in the above Lemma, i.e. (3.4) and (3.3); these will correspond to the interface points.  $\square$ 

#### 3.3.2.2 Vertex detection

To detect the vertices we introduce waveguides, and make use of their coupling. For multi-dimensional polyhedron, we use directional couplers. Hence we start by introducing the relevant notions.

#### **3.3.2.2.1** Waveguides

Total internal reflection (TIR), a principle essential for understanding light behavior in optical fibers and other waveguide technologies, arises when light transitions from a denser medium to a rarer one  $(n_1 > n_2)$ , resulting in complete reflection at the interface without transmission. This is captured for TE-polarized waves where the critical angle causes  $\cos\theta_2$  to become imaginary, denoted by  $\cos\theta_2 = -i\sqrt{\frac{n_1^2\sin^2\theta_1}{n_2^2}-1}$ , indicating the absence of wave transmission across the boundary.

In TIR, the transmitted fields adjust to maintain  $E_y, H_x, H_z$  components, with power flow exclusively parallel to the interface, and no cross-boundary energy transfer. This is mathematically expressed through wave equations for upward moving waves in the lower medium,  $E_1 = E_0 e^{i(\omega t - \beta z - \kappa x)}$  and  $E_3 = E_0 e^{i(\omega t - \beta z + \kappa x)}$ , with  $\beta$  and  $\kappa$  describing wave propagation and boundary interaction.

Introducing two TIR interfaces creates a waveguide, confining the wave between them and allowing for evanescent decay outside, as shown by  $\vec{E} = A \cos \kappa x e^{i(\omega t - \beta z)}$ .

#### 3.3.2.2.2 Waveguide Modes

Modes developed include TE Mode, which is a TE-polarized wave guided in a waveguide, and the TM Mode, guided similarly as a TM-polarized wave. The waveguides can have different geometries -rectangular, circular, or arbitrary- with varied refractive index (RI) distribution n(x,y). Specifically, for a planar design, RI depends on the x-coordinate, assuming the structure is infinitely extended along the yz-plane. Inhomogeneous wave equations for E and H fields in waveguides are

$$\nabla^2 \vec{E} + \nabla (\frac{\nabla n^2}{n^2} \cdot \vec{E}) = \mu_0 \varepsilon_0 n^2 \frac{\partial^2 \vec{E}}{\partial t^2}, \tag{3.5}$$

and

$$\nabla^2 \vec{H} + \frac{\nabla n^2}{n^2} \times (\nabla \times \vec{H}) = \mu_0 \varepsilon_0 n^2 \frac{\partial^2 \vec{H}}{\partial t^2}, \tag{3.6}$$

respectively. These fields' variations depend on the waveguide's RI profile. TE and TM modes reveal specific field dependence of field components, with TEM mode equation for  $E_v$  being

$$\frac{\partial^2 E_y}{\partial x^2} + (k_0^2 n^2 - \beta^2) E_y = 0, \tag{3.7}$$

illustrating mode behavior in RI variable waveguides.

#### **3.3.2.2.3 Mode coupling**

We examine the mode coupling phenomenon in axially invariant, uniform waveguides, where separate modes are supported with invariant field patterns during propagation. Unlike in uniform waveguides, where only the phase of modes changes, couplers induce variations in mode amplitudes through energy redistribution. This coupling may occur between modes within the waveguide or involve conversion from guided to radiation modes. Hence, we study these power redistributions in detail. Introducing a perturbation to an ideal waveguide facilitates the exchange of energy between modes, potentially enabling complete conversion from one mode to another under specific conditions. Mode coupling is a pivotal process that, under certain circumstances, allows for nearly total energy transfers between specific modes.

A directional coupler enhances mode exchange by facilitating co-directional coupling of two identical modes. It utilizes the waveguide's evanescent fields, which extend beyond the waveguide's boundaries. Thus, when two waveguides are placed sufficiently close that their evanescent fields overlap, energy is redistributed between the guides. With adequate distance, this fundamental power transfer can extend almost the entire interaction length, making power coupling and decoupling periodic functions of the interaction length.

The total field of the coupled waveguides,  $\psi(x, y, z)$ , is expressible as a linear combination of the individual waveguide modes,  $\psi_1$  and  $\psi_2$ , i.e.,

$$\psi(x, y, z) = a(z)\psi_1(x, y) + b(z)\psi_2(x, y), \tag{3.8}$$

The coupled mode equations are given by

$$\frac{\partial a}{\partial z} = -i(\beta_1 + \kappa_{11})a - i\kappa_{12}b,\tag{3.9}$$

$$\frac{\partial b}{\partial z} = -i(\beta_2 + \kappa_{22})b - i\kappa_{21}a,\tag{3.10}$$

where  $\beta_1$  and  $\beta_2$  denote the propagation constants of the waveguides' modes, and the  $\kappa$  values represent the coupling coefficients.

**Proof of Theorem 3.1.2 (ii).** We consider two mathematical waveguides on two interfaces. The corner which constitutes the meeting point of the interfaces is going to satisfy the waveguide coupling mode equations; the smoothening of the metric allows for calculation of the values at the vertex points.. Let us note that we regard waveguides which have extremely small inter-interfacial area, hence coupled have again size approximately equal to the interface size. □

#### 3.3.2.2.4 Multiple interfaces meeting at a vertex

The material of this section is in addition to [57], also from [58].

In advancing the application of coupled mode equations to higher dimensions, it's essential to employ directional couplers, integral in enabling field interactions between dual-channel optical waveguides. These couplers facilitate energy transfer through evanescent mode coupling, leading to dynamic power redistribution between closely placed waveguides. The interaction is characterized by power tapping and reciprocal energy exchange, attributed to the overlapping of external fields via evanescent mode coupling. This process underpins the theoretical framework for analyzing power exchange between two waveguides, further elaborated through coupled mode equations.

Specifically, if we consider waves in two parallel waveguides with expressions

$$a(z) = a_0 e^{-i\beta z},$$
  

$$b(z) = b_0 e^{-i\beta z},$$
(3.11)

the resulting power in each waveguide can be respectively described as

$$|a(z)|^2 = 1 - \frac{\kappa^2}{\frac{1}{4}\Delta\beta^2 + \kappa^2} \sin^2\{\left(\sqrt{\frac{1}{4}\Delta\beta^2 + \kappa^2}\right)z\},$$
 (3.12)

$$|b(z)|^2 = \frac{\kappa^2}{\frac{1}{4}\Delta\beta^2 + \kappa^2} \sin^2\{\left(\sqrt{\frac{1}{4}\Delta\beta^2 + \kappa^2}\right)z\}.$$
 (3.13)

This mathematical formulation is crucial for understanding the variation of power along the z-axis in the waveguides.

Furthermore, an RC filter, constituted of multiple directional couplers and delayline sections, acts as an add-drop filter. This arrangement can be mathematically represented through the multiplication of transmission matrices corresponding to each coupler and delay-line section. The transmission matrix for an N-stage RC filter is denoted as

$$\begin{bmatrix} Y_1 \\ Y_2 \end{bmatrix} = T_c(L_{N+1}) \cdots T_{MZ} T_c(L_2) T_{MZ} T_c(L_1) \begin{bmatrix} X_1 \\ X_2 \end{bmatrix}, \qquad (3.14)$$

with  $T_{MZ}$  and  $T_c$  representing the transmission matrices for the delay-line section and the coupler, respectively.

**Proof of Theorem 3.1.2 (iii).** So many stages should be added to the directional coupler as the number of interfaces that meet at a vertex minus 1. Then the directional coupler will perform coupling of the waveguides corresponding to these interfaces, and when this value is recovered this will indicate the vertex is detected.  $\Box$ 

#### 3.3.3 Electromagnetic waves in anisotropic non-linear media

The material of this section is from [59].

#### 3.3.3.1 Crystal detection

For the crystal lattice we need to detect the vertices, i.e. interface is not relevant. We use the four-wave mixing formula as the condition for checking for a vertex. First we use z-scan for third order nonlinearity susceptibility, which is necessary for the four-wave mixing formula -we describe it in the appendix.

#### 3.3.3.1.1 Four-wave-mixing

In four-wave mixing, three monochromatic pump fields of frequencies  $\omega_1, \omega_2$ , and  $\omega_3$  interact within a medium characterized by its third-order nonlinear susceptibility to produce a polarization  $P_{NL}^{(3)}(\omega_s)$  at the mixed frequency  $\omega_s = \omega_1 \pm \omega_2 \pm \omega_3$ . This

generates a signal field at  $\omega_s$ , propagating in the z-direction through a cubic or isotropic nonlinear optical medium. Under assumptions such as plane monochromatic fields, undepleted pump fields, and signal propagation along the z-direction, the signal field's evolution, based on slowly varying envelope approximation, is governed by the differential equation

$$\frac{dE_s}{dz} = -\frac{i\omega_s^2 \mu_0 \varepsilon_0}{2k_s} \chi_{eff}^{(3)} E_1(z) E_2(z) E_3(z) e^{-i(\Delta \bar{k} \cdot \hat{s}_z)z}, \tag{3.15}$$

where  $\chi_{eff}^{(3)}$  is the third order nonlinear susceptibility and  $\Delta \vec{k} = \vec{k}_s - \vec{k}_1 - \vec{k}_2 - \vec{k}_3$  represents the phase mismatch. Integration of this equation, given the initial condition  $E_s(z=0)=0$ , leads to the signal field expression:

$$E_s(z) = \frac{\omega_s^2 \mu_0 \varepsilon_0}{2k_s (\Delta \vec{k} \cdot \hat{e}_z)} \chi_{eff}^{(3)} E_1(0) E_2(0) E_3(0) \left[ \frac{\sin\left(\frac{(\Delta \vec{k} \cdot \hat{e}_z)z}{2}\right)}{\left(\frac{(\Delta \vec{k} \cdot \hat{e}_z)z}{2}\right)} \right]^2, \tag{3.16}$$

highlighting that maximum signal intensity is achieved when the phase matching condition  $\Delta k = 0$  is satisfied. In a special case where the signal and one of the pump fields are degenerate ( $\omega_s = \omega_3$ ), the signal field grows exponentially with distance, characterized by gain or loss, as described by

$$E_s(z) = E_s(0) \exp(g_s z),$$
 (3.17)

where  $g_s(z)$  represents the gain or loss coefficient, emphasizing the controlled amplification or attenuation of the signal field through phase management in the nonlinear medium.

**Proof of Theorem 3.1.3.** We consider the case  $\omega_s = \omega_3$  above, where  $E_3$  represents the normal geodesic on the vertex. We use Z-scan to get the third order nonlinear susceptibility, which is necessary for the four-wave mixing equation (3.17). The points on the normal geodesic that satisfy (3.17) indicate a vertex.  $\square$ 

#### 3.3.4 Acoustic waves in fluid media

The material of this section is from [60].

The conditions for the interface detection use the pressure transmission and reflection coefficients. For the vertices, we use waveguiding, and an acoustic transmission line direction coupler.

#### 3.3.4.1 Interface detection

Regarding the propagation of acoustic waves across fluidic media interfaces, the process involves calculating the transmission and reflection coefficients for pressure waves. This calculation is crucial for understanding acoustic transmission lines or waveguides in various media. When an acoustic wave transmits from one medium to another, a portion of its energy is transmitted through the new medium while the remainder is reflected. This principle applies regardless of the medium being solid or fluid. In the case of lossless fluid media and planar waves, the complexity of this phenomenon is reduced. The fundamental equations for pressure p and velocity u in acoustic wave propagation are represented as

$$\left\{ \begin{array}{c} p(x,t) \\ u(x,t) \end{array} \right\} = Re \left[ \left\{ \begin{array}{cc} p_{+}(s) & p_{-}(s) \\ \frac{p_{+}(s)}{z_{0}} & \frac{-p_{-}(s)}{z_{0}} \end{array} \right\} \left\{ \begin{array}{c} e^{-sx/c} \\ e^{sx/c} \end{array} \right\} e^{st} \right], \quad (3.18)$$

where  $z_0$  denotes the characteristic impedance. For a planar wave encountering a fluidic interface, the intensity transmission and reflection coefficients,  $T_I$  and  $R_I$ , are used to quantify the energy distribution process. These coefficients are defined as

$$T_I = \frac{4(Z_2/Z_1)}{[(Z_2/Z_1) - 1]^2}$$
(3.19)

and

$$R_I = \left[\frac{(Z_2/Z_1) - 1}{(Z_2/Z_1) + 1}\right]^2,\tag{3.20}$$

highlighting the role of characteristic impedances  $Z_1$  and  $Z_2$  in determining the wave's behavior at the interface. The boundary conditions, including equal acoustic pressure and the continuity of particle velocities across the interface, ensure material coherence and facilitate the precise analysis of wave interactions at media boundaries. This framework simplifies the complex phenomena associated with acoustic wave transmission and reflection, aiding in the understanding of acoustic wave behavior in

different media.

**Proof of Theorem 3.1.4 (i).** Following a shortest geodesic, this will be normal to the interface from both of its sides. Hence we can recover waves up to a very small part past the interface. We test the recovered values to spot the ones which satisfy the transmission and reflection coefficients, i.e. (3.19) and (3.20) in the above Lemma; these will correspond to the interface points.  $\square$ 

#### 3.3.4.2 Vertex detection

**Proof of Theorem 3.1.4 (ii).** The acoustic multi-stage directional coupler with as many transmission matrices as the number of interfaces meeting at a vertex minus 1, obeys the same equation (3.14) as the one for the electromagnetic case, with the acoustic transmission line equations (3.18) replacing the electromagnetic ones.  $\Box$ 

#### **Chapter 4**

## Electrical impedance tomography revisited

In this Chapter we present a novel EIT algorithm. The algorithm involves the following steps (all relevant equations are derived below):

- 1. Using the given Dirichlet and Neumann data, we calculate  $u_z$  on the boundary via Eq. (4.14).
- 2. From Eq. (4.30), we calculate  $\hat{v}$  numerically; the RHS can be calculated from Eq. (4.19) using Eq. (4.14).
- 3. From Eq. (4.22), we find  $u_z$ , using  $\hat{v}$  and the calculated RHS of (4.30).
- 4. We numerically integrate  $u_z$  to find u.

#### **Notation**

• Let  $z, \zeta, h, \eta, k$ , be complex variables,

$$z = z_1 + iz_2$$
,  $\zeta = \zeta_1 + i\zeta_2$ ,  $h = h_1 + ih_2$ ,  $\eta = \eta_1 + i\eta_2$ ,  $k = k_1 + ik_2$ ,

where  $z_j, \zeta_j, h_j, \eta_j, k_j, j = 1, 2$  are real variables.

- Bar will denote complex conjugation.
- $\partial \Omega$  will denote the boundary of the two-dimensional domain  $\Omega$ .
- For simplicity of notation, f(z) will denote  $f(z,\bar{z})$ , i.e f(z) means that f is a

function of the two independent variables  $z_1$  and  $z_2$ .

#### **Basic Formulas**

This work makes crucial use of the following formulas, known as Pompeiu's formulas, for the complex-valued continuously differentiable function f(z):

$$f(z) = \frac{1}{2i\pi} \int_{\partial\Omega} \frac{f(\zeta)}{\zeta - z} d\zeta - \frac{1}{\pi} \iint_{\Omega} \frac{\partial f(\zeta)}{\partial \overline{\zeta}} \frac{d\zeta_1 d\zeta_2}{\zeta - z}, \ z \in \Omega, \tag{4.1}$$

$$f(z) = -\frac{1}{2i\pi} \int_{\partial\Omega} \frac{f(\zeta)}{\overline{\zeta} - \overline{z}} d\overline{\zeta} - \frac{1}{\pi} \iint_{\Omega} \frac{\partial f(\zeta)}{\partial \zeta} \frac{d\zeta_1 d\zeta_2}{\overline{\zeta} - \overline{z}}, \ z \in \Omega, \tag{4.2}$$

In the particular case of  $f(z) = 1/(z-z_0)$ , equation (4.1) suggests the following important identity:

$$\frac{1}{\pi} \frac{\partial}{\partial \overline{z}} \frac{1}{z - z_0} = \delta(z - z_0), \ z, z_0 \in \mathbb{C}. \tag{4.3}$$

Indeed, as the boundary  $\partial\Omega$  of the clopen  $\Omega\equiv\mathbb{C}$  is the empty set, the first integral on the right-hand side of (4.1) vanishes, and (4.1) implies (4.3) by virtue of the definition of the  $\delta$ -function.

## 4.1 A simple re-derivation of the basic equations of EIT

Let the real-valued function u(z) satisfy the PDE

$$u_{77} = qu, \tag{4.4}$$

where q(z) is a real-valued function.

Letting in (4.1)  $f = e^{-ikz}u_z$ , and employing (4.4), equation (4.1) becomes

$$u_{z}(z) = \frac{1}{2i\pi} \int_{\partial\Omega} e^{ikz - ik\zeta} u_{\zeta}(\zeta) \frac{d\zeta}{\zeta - z} - \frac{1}{\pi} \iint_{\Omega} e^{ikz - ik\zeta} (qu)(\zeta) \frac{d\zeta_{1}d\zeta_{2}}{\zeta - z}, \ k \in \mathbb{C}, z \in \Omega.$$

$$(4.5)$$

Letting in (4.2)  $f = e^{i\bar{k}\bar{z}}u$ , we find

$$u = -\frac{1}{2i\pi} \int_{\partial\Omega} e^{-i\overline{k}\overline{z} + i\overline{k}\overline{\zeta}} \frac{u(\zeta)d\overline{\zeta}}{\overline{\zeta} - \overline{z}} - \frac{1}{\pi} \iint_{\Omega} e^{-i\overline{k}\overline{z} + i\overline{k}\overline{\zeta}} u_{\zeta}(\zeta) \frac{d\zeta_{1}d\zeta_{2}}{\overline{\zeta} - \overline{z}}, \ k \in \mathbb{C}, z \in \Omega.$$

$$(4.6)$$

Replacing in (4.6)  $u_{\zeta}(\zeta)$  via (4.5) we find the following:

$$u = -\frac{1}{2i\pi} \int_{\partial\Omega} e^{i\overline{k}(\overline{\zeta} - \overline{z})} u(\zeta) \frac{d\overline{\zeta}}{\overline{\zeta} - \overline{z}} + \frac{1}{2i} \int_{\partial\Omega} G^{k}(z, \eta) u_{\eta}(\eta) d\eta - \iint_{\Omega} G^{k}(z, \eta) (qu)(\eta) d\eta_{1} d\eta_{2},$$

$$k \in \mathbb{C}, \ z \in \Omega. \quad (4.7)$$

where

$$G^{k}(z,\eta) = -\frac{1}{\pi^{2}} \iint_{\Omega} \frac{e^{i(-\overline{k}\overline{z}-k\eta+k\zeta+\overline{k}\overline{\zeta})} d\zeta_{1} d\zeta_{2}}{(\overline{\zeta}-\overline{z})(\eta-\zeta)}.$$
 (4.8)

With the change of variables  $\zeta = z + \eta$ , (4.8) becomes

$$G^k(z, \eta) = rac{1}{\pi^2} \iint_{\Omega} rac{e^{i(kz + \overline{k}\overline{\eta})} d\eta_1 d\eta_2}{\overline{\eta}z},$$

implying that

$$G^{k}(z,\eta) = G^{k}(z-\eta), \tag{4.9}$$

with

$$G^{k}(z) = \frac{1}{\pi^{2}} \iint_{\Omega} \frac{e^{i(kz+k\eta+\overline{k}\overline{\eta})} d\eta_{1} d\eta_{2}}{\overline{\eta}(\eta+z)}.$$
 (4.10)

Using the identity

$$\frac{\partial G^k(z-\eta)}{\partial z} = -\frac{1}{\pi} \frac{e^{ik(z-\eta)}}{z-\eta}, \ k \in \mathbb{C}, z \in \mathbb{C}, \tag{4.11}$$

and employing (4.9) and integration by parts, (4.7) becomes the basic equation of EIT:

$$u(z) = -\frac{1}{2i\pi} \int_{\partial\Omega} e^{i\overline{k}(\overline{\zeta} - \overline{z})} u(\zeta) \frac{d\overline{\zeta}}{\overline{\zeta} - \overline{z}} - \frac{1}{2i\pi} \int_{\partial\Omega} e^{ik(z-\eta)} \frac{u(\eta)d\eta}{z - \eta} - \iint_{\Omega} G^{k}(z-\eta)(qu)(\eta)d\eta_{1}d\eta_{2},$$

$$k \in \mathbb{C}, z \in \Omega. \quad (4.12)$$

Incidentally, the easiest way to derive (4.11) is to first establish the identity

$$\frac{\partial G^{k}(z)}{\partial \overline{z}} = -\frac{1}{\pi} \frac{e^{-i\overline{k}\overline{z}}}{\overline{z}}, \ k \in \mathbb{C}, z \in \mathbb{C}, \tag{4.13}$$

and then find (4.11) by taking the complex conjugate of (4.13) and using the identity

$$\overline{G^k(z-\eta)}=G^k(z-\eta).$$

To find (4.13) we differentiate (4.10) with respect to  $\partial_{\overline{z}}$  and use (4.3), i.e.

$$\begin{split} \frac{\partial G^k(z)}{\partial \bar{z}} &= \frac{1}{\pi^2} \iint_{\Omega} \frac{\mathrm{e}^{\mathrm{i}(kz+k\eta+\bar{k}\bar{\eta})}}{\bar{\eta}} \frac{\partial}{\partial \bar{z}} \frac{1}{\eta - (-z)} d\eta_1 d\eta_2 = \frac{1}{\pi^2} \iint_{\Omega} \frac{\mathrm{e}^{\mathrm{i}(kz+k\eta+\bar{k}\bar{\eta})}}{\bar{\eta}} \pi \delta(\eta - (-z)) d\eta_1 d\eta_2 \\ &= -\frac{1}{\pi} \frac{\mathrm{e}^{-\mathrm{i}\bar{k}\bar{z}}}{\bar{z}}. \end{split}$$

# **4.2** Using the equation for $u_z$

Equation (4.5) is much simpler than the basic equation (4.12). Furthermore, if both the Dirichlet and the Neumann data are given, then

$$u_z dz = \frac{1}{2} \left( \frac{\partial u(z(s))}{\partial s} + i \frac{\partial u(z(s))}{\partial v} \right) ds, \ z(s) \in \partial \Omega, \tag{4.14}$$

where s denotes the arc-length parameterization of the curve  $\partial\Omega$ , hence  $\partial u/\partial s$  is the derivative of f along the tangent of  $\partial\Omega$ , and  $\partial/\partial v$  is the derivative along the outward normal to  $\partial\Omega$ . Identity (4.14) implies that the first term of the right-hand side of (4.5) is known.

In what follows we will show that useful information can be obtained by employing Eq. (4.5). In this connection, we first concentrate on the simple case that  $\Omega$  is the unit disc, and we also take k = 0.

$$\zeta = \tau e^{i\phi},\tag{4.15}$$

4.2. Using the equation for 
$$u_z$$

74

then

$$\partial_{\zeta} = \frac{1}{2} e^{-i\varphi} \left[ \partial_{\tau} - \frac{i}{\tau} \partial_{\varphi} \right], \ \partial_{\overline{\zeta}} = \frac{1}{2} e^{i\varphi} \left[ \partial_{\tau} + \frac{i}{\tau} \partial_{\varphi} \right]. \tag{4.16}$$

Letting

$$u(\tau,\phi) = \sum_{m=-\infty}^{\infty} \hat{u}_m(\tau) e^{\mathrm{i}m\phi}, \qquad (4.17)$$

it follows from (4.16) that

$$u_{\zeta} = \frac{1}{2} \sum_{m=-\infty}^{\infty} e^{i(m-1)\phi} \left[ \frac{d\hat{u}_{m}(\tau)}{d\tau} + \frac{m}{\tau} \hat{u}_{m}(\tau) \right], \tag{4.18}$$

$$u_{\zeta}|_{\partial\Omega} = \frac{1}{2} \sum_{m=-\infty}^{\infty} e^{i(m-1)\phi} \left[ \frac{d\hat{u}_{m}(1)}{d\tau} + m\hat{u}_{m}(1) \right] = \frac{1}{2} \sum_{m=-\infty}^{\infty} \zeta^{m-1} \left[ \frac{d\hat{u}_{m}(1)}{d\tau} + m\hat{u}_{m}(1) \right]. \tag{4.19}$$

Similarly, we let

$$(qu)(\tau,\phi) = \sum_{m=-\infty}^{\infty} \hat{v}_m(\tau) e^{\mathrm{i}m\phi}, \qquad (4.20)$$

$$(qu)(\zeta)d\zeta_1 d\zeta_2 = \sum_{m=-\infty}^{\infty} \hat{v}_m(\tau) e^{\mathrm{i}m\phi}(\tau d\tau d\phi) = \sum_{m=-\infty}^{\infty} \hat{v}_m(\tau) \zeta^m \tau^{-m}(-\mathrm{i}e^{-\mathrm{i}\phi} d\tau d\zeta)$$

$$= -\mathrm{i} \sum_{m=-\infty}^{\infty} \hat{v}_m(\tau) \zeta^{m-1} \tau^{-m+1} d\tau d\zeta. \qquad (4.21)$$

Therefore using (4.19) and (4.21), equation (4.5) becomes

where we employed Cauchy's Integral Formula to get the last equality.

If  $\rho = 1$ , then we recover identity (4.19)

$$u_{z}(z)|_{z=e^{i\theta}} = \frac{1}{2} \sum_{m=-\infty}^{\infty} \left[ \frac{d\hat{u}_{m}(1)}{d\tau} + m\hat{u}_{m}(1) \right] e^{i\theta(m-1)}$$
(4.23)

Expanding the integral from  $\rho$  to 1 as a Taylor's series around  $\rho = 1$ ,

$$-\int_{\rho}^{1} \tau^{-m+1} \hat{v}_{m}(\tau) d\tau = \sum_{n=0}^{\infty} \frac{\left(\int_{1}^{\rho} \tau^{-m+1} \hat{v}_{m}(\tau) d\tau\right)^{(n)}|_{\rho=1}}{n!} (\rho - 1)^{n}$$

$$= \hat{v}_{m}(1)(\rho - 1) \left(1 + \frac{(-m+1)}{2!}(\rho - 1) + \frac{(-m+1)(-m)}{3!}(\rho - 1)^{2} + \dots\right)$$

$$+O\left((\rho - 1)^{2}\right), \quad (\rho - 1) \to 0,$$

(4.22) becomes

$$u_{z}(z) = \frac{1}{2} \sum_{m=-\infty}^{\infty} \left[ \frac{d\hat{u}_{m}(1)}{d\tau} + m\hat{u}_{m}(1) \right] z^{m-1}$$

$$+2 \sum_{m=-\infty}^{\infty} z^{m-1} \hat{v}_{m}(1) (\rho - 1) \left( 1 + \frac{(-m+1)}{2!} (\rho - 1) + \frac{(-m+1)(-m)}{3!} (\rho - 1)^{2} + \dots \right)$$

$$+O\left( (\rho - 1)^{2} \right), \ (\rho - 1) \to 0.$$

$$(4.24)$$

#### 4.3 Direct Constraints

Poincaré's lemma

$$\int_{\partial\Omega} F = \iint_{\Omega} dF,\tag{4.25}$$

with

$$F = Gdz$$
,  $dF = G_{\overline{z}}d\overline{z} \wedge dz = 2iG_{\overline{z}}dz_1dz_2$ ,

yields the complex form of Green's theorem

$$\int_{\partial\Omega} G(z)dz = 2i \iint_{\Omega} G_{\overline{z}}(z)dz_1dz_2. \tag{4.26}$$

Letting

$$G(z) = (\sum_{n=0}^{\infty} c_n z^n) u_z(z), \ z = \tau e^{i\phi}, \tag{4.27}$$

and using (4.19) we find

$$G(z)dz|_{\partial\Omega} = \left(\sum_{n=0}^{\infty} c_n z^n\right) \frac{1}{2} \sum_{m=-\infty}^{\infty} e^{i(m-1)\phi} \left[\frac{d\hat{u}_m(1)}{d\tau} + m\hat{u}_m(1)\right] (ie^{i\phi}d\phi)$$

$$= \frac{i}{2} \sum_{n=0}^{\infty} c_n \sum_{m=-\infty}^{\infty} e^{i(n+m)\phi} \left[\frac{d\hat{u}_m(1)}{d\tau} + m\hat{u}_m(1)\right] d\phi, \qquad (4.28)$$

while using (4.4) and (4.20) we find

$$G_{\overline{z}}(z)dz_{1}dz_{2} = \left(\frac{\partial}{\partial \overline{z}}\left(\sum_{n=0}^{\infty}c_{n}z^{n}\right)u_{z}(z) + \left(\sum_{n=0}^{\infty}c_{n}z^{n}\right)u_{z}\overline{z}(z)\right)dz_{1}dz_{2} = \left(\sum_{n=0}^{\infty}c_{n}z^{n}\right)qu(\tau,\phi)(\tau d\tau d\phi)$$

$$= \sum_{n=0}^{\infty}c_{n}\sum_{m=-\infty}^{\infty}\hat{v}_{m}(\tau)e^{i(n+m)\phi}\tau^{n+1}d\tau d\phi, \qquad (4.29)$$

where the first term on the right-hand side vanishes as it contains the d-bar derivative of an analytic function. Using (4.28) and (4.29) in (4.26) we find

$$\frac{\mathrm{i}}{2} \sum_{n=0}^{\infty} c_n \sum_{m=-\infty}^{\infty} \int_0^{2\pi} \mathrm{d}\phi e^{i(n+m)\phi} \left[ \frac{d\hat{u}_m(1)}{d\tau} + m\hat{u}_m(1) \right] = 2i \sum_{n=0}^{\infty} c_n \sum_{m=-\infty}^{\infty} \int_0^{2\pi} \mathrm{d}\phi e^{i(n+m)\phi} \int_0^1 d\tau \tau^{n+1} \hat{v}_m(\tau).$$

The integration over  $\tau$  implies that m = -n. Then, since the above equation is valid for all  $c_n$ , it follows that

$$\int_0^1 d\tau \tau^{n+1} \hat{v}_{-n}(\tau) = \frac{1}{4} \left[ \frac{d\hat{u}_{-n}(1)}{d\tau} - n\hat{u}_{-n}(1) \right], \ n \ge 0.$$
 (4.30)

The fact that u is real implies that  $\hat{v}_{-n}(\tau) = \overline{\hat{v}}_n(\tau)$ . Thus, (4.30) implies constraints for all the coefficients of qu.

# 4.4 $\Omega$ arbitrary bounded domain, i.e. not restricted to unit disk

We first show that Eq (4.22) is valid even after removing the restriction k = 0. Using (4.19) and (4.21), equation (4.5) without assuming k = 0 becomes

$$u_{z}(z) = \frac{1}{4i\pi} \sum_{m=-\infty}^{\infty} \left[ \frac{d\hat{u}_{m}(1)}{d\tau} + m\hat{u}_{m}(1) \right] \int_{\partial\Omega} \frac{e^{ikz - ik\zeta} \zeta^{m-1} d\zeta}{\zeta - z}$$

$$+ \frac{i}{\pi} \sum_{m=-\infty}^{\infty} \int_{\rho}^{1} d\tau \hat{v}_{m}(\tau) \tau^{-m+1} \int_{\partial\Omega} \frac{e^{ikz - ik\zeta} \zeta^{m-1} d\zeta}{\zeta - z}$$

$$= \frac{1}{2} \sum_{m=-\infty}^{\infty} \left[ \frac{d\hat{u}_{m}(1)}{d\tau} + m\hat{u}_{m}(1) \right] z^{m-1} - 2 \sum_{m=-\infty}^{\infty} z^{m-1} \int_{\rho}^{1} \hat{v}_{m}(\tau) \tau^{-m+1} d\tau,$$

$$z = \rho e^{i\theta}, \ 0 < \rho < 1, \ 0 < \theta < 2\pi,$$

where we used Cauchy's Integral Formula. Hence equation (4.22) does not change, i.e. it is the same in both k = 0 and  $k \neq 0$  case.

Using (4.18) and (4.21), (4.5) becomes

$$u_{z}(z) = \frac{1}{4i\pi} \sum_{m=-\infty}^{\infty} \int_{\partial\Omega} \frac{\zeta^{m-1}}{\tau^{m-1}} \left[ \frac{d\hat{u}_{m}(\tau)}{d\tau} + \frac{m}{\tau} \hat{u}_{m}(\tau) \right] \frac{e^{ikz - ik\zeta} d\zeta}{\zeta - z}$$

$$+ \frac{i}{\pi} \sum_{m=-\infty}^{\infty} \int_{\rho}^{\tau} d\tau \hat{v}_{m}(\tau) \tau^{-m+1} \int_{\partial\Omega} \frac{\zeta^{m-1} e^{ikz - ik\zeta} d\zeta}{\zeta - z}$$

$$= \frac{1}{2} \sum_{m=-\infty}^{\infty} \frac{z^{m-1}}{\tau^{m-1}} \left[ \frac{d\hat{u}_{m}(\tau)}{d\tau} + \frac{m}{\tau} \hat{u}_{m}(\tau) \right] - 2 \sum_{m=-\infty}^{\infty} z^{m-1} \int_{\rho}^{\tau} \hat{v}_{m}(\tau) \tau^{-m+1} d\tau,$$

$$z = \rho e^{i\theta}, \ \rho = |z|, \ \theta = arg(z), \tag{4.31}$$

where the Cauchy Integral Formula was used.

Using (4.18), (4.27) becomes

$$G(z)dz|_{\partial\Omega} = \left(\sum_{n=0}^{\infty} c_n z^n\right) \frac{1}{2} \sum_{m=-\infty}^{\infty} e^{i(m-1)\phi} \left[\frac{d\hat{u}_m(\tau)}{d\tau} + \frac{m}{\tau} \hat{u}_m(\tau)\right] (i\tau e^{i\phi} d\phi)$$

$$= \frac{i}{2} \sum_{n=0}^{\infty} c_n \sum_{m=-\infty}^{\infty} e^{i(n+m)\phi} \tau^{n+1} \left[\frac{d\hat{u}_m(\tau)}{d\tau} + \frac{m}{\tau} \hat{u}_m(\tau)\right] d\phi. \tag{4.32}$$

Using (4.32) and (4.29) in (4.26) we find

$$\begin{split} \frac{\mathrm{i}}{2} \sum_{n=0}^{\infty} c_n \sum_{m=-\infty}^{\infty} \int_0^{2\pi} \mathrm{d}\phi \, e^{i(n+m)\phi} \, \tau^{n+1} \big[ \frac{d\hat{u}_m(\tau)}{d\tau} + \frac{m}{\tau} \hat{u}_m(\tau) \big] \\ &= 2i \sum_{n=0}^{\infty} c_n \sum_{m=-\infty}^{\infty} \int_0^{2\pi} \mathrm{d}\phi \, e^{i(n+m)\phi} \int_0^{\tau} d\tau \, \tau^{n+1} \hat{v}_m(\tau). \end{split}$$

The integration over  $\tau$  implies that m = -n. Then, since the above equation is valid for all  $c_n$ , it follows that

$$\int_0^{\tau} d\tau \, \tau^{n+1} \hat{v}_{-n}(\tau) = \frac{1}{4} \tau^{n+1} \left[ \frac{d\hat{u}_{-n}(\tau)}{d\tau} - \frac{n}{\tau} \hat{u}_{-n}(\tau) \right], \, n \ge 0.$$
 (4.33)

Again the fact that u is real implies that  $\hat{v}_{-n}(\tau) = \overline{\hat{v}}_n(\tau)$ . Thus, (4.33) implies constraints for all the coefficients of qu.

# 4.5 Appendices

#### 4.5.1 Appendix I (verification of (4.22))

Using the representation (4.17), and employing the identities (4.16) we find

$$u_{z\bar{z}} = \frac{1}{4} \left[ \partial^2 \tau + \frac{1}{\tau} \partial \tau + \frac{1}{\tau^2} \partial^2 \phi \right] u(\tau, \phi) = \frac{1}{4} \sum_{m=-\infty}^{\infty} \left[ \frac{\mathrm{d}^2 \hat{u}_m(\tau)}{\mathrm{d}\tau^2} + \frac{1}{\tau} \frac{\mathrm{d}\hat{u}_m(\tau)}{\mathrm{d}\tau} - \frac{m^2}{\tau^2} \hat{u}_m(\tau) \right] e^{\mathrm{i}m\varphi}. \tag{4.34}$$

Then integration by parts yields:

$$\int_{\rho}^{1} d\tau \tau^{-m+1} \hat{v}_{m}(\tau) = \frac{1}{4} \int_{\rho}^{1} d\tau \tau^{-m+1} \left[ \frac{d^{2} \hat{u}_{m}(\tau)}{d\tau^{2}} + \frac{1}{\tau} \frac{d\hat{u}_{m}(\tau)}{d\tau} - \frac{m^{2}}{\tau^{2}} \hat{u}_{m}(\tau) \right] 
= \frac{1}{4} \left[ \frac{d\hat{u}_{m}(1)}{d\tau} + m\hat{u}_{m}(1) - \frac{d\hat{u}_{m}(\rho)}{d\rho} \rho^{1-m} - m\hat{u}_{m}(\rho) \rho^{-m} \right].$$

Hence, equation (4.22) becomes

$$u_{z} = \frac{1}{2} \sum_{m=-\infty}^{\infty} \left[ \frac{d\hat{u}_{m}(1)}{d\tau} + m\hat{u}_{m}(1) \right] z^{m-1} - \frac{1}{2} \sum_{m=-\infty}^{\infty} z^{m-1} \left[ \frac{d\hat{u}_{m}(1)}{d\tau} + m\hat{u}_{m}(1) \right] + \frac{1}{2} \sum_{m=-\infty}^{\infty} z^{m-1} \left[ \rho^{1-m} \frac{d\hat{u}_{m}(\rho)}{d\rho} + m\rho^{-m} \hat{u}_{m}(\rho) \right],$$

or

$$u_z = \frac{1}{2} \sum_{m=-\infty}^{\infty} e^{i(m-1)\theta} \left[ \frac{\mathrm{d}\hat{u}_m(\rho)}{\mathrm{d}\rho} + \frac{m}{\rho} \hat{u}_m(\rho) \right], \tag{4.35}$$

which is indeed valid by (4.18).

# 4.5.2 Appendix II (verification of (4.30))

Letting  $q = \frac{1}{4}$ , (4.4) is a modified Helmholtz equation, hence its fundamental solution corresponding to  $k = \sqrt{-(-\frac{1}{4})} = \frac{1}{2}$  is

$$G(\xi, \zeta; x, y) = \frac{1}{2\pi} K_0(k|\zeta - z|) = \frac{1}{2\pi} K_0(\frac{1}{2}|\zeta - z|),$$

with z = x + iy,  $\zeta = \xi + i\zeta$ , where  $K_0(z)$  denotes the zeroth order modified Bessel function of the second kind, where

$$K_m(x) = \int_0^\infty e^{-x\cosh(t)} \cosh(mt) dt.$$

Hence, it follows that

$$u(\tau,\phi) = \sum_{m=-\infty}^{\infty} d_m \frac{K_m(\tau)}{K_m(1)} e^{\mathrm{i}m\phi}, \tag{4.36}$$

where  $K_m(\tau)$  with  $k = \frac{1}{2}$  is analytic at  $\tau = 1$ .

In this case,

$$\frac{\mathrm{d}\hat{u}_m(1)}{\mathrm{d}\tau} = d_m \frac{K'_m(1)}{K_m(1)}, \ \hat{u}_m(1) = d_m. \tag{4.37}$$

Also,

$$\hat{v}_m(\rho) = \frac{d_m}{4} \frac{K_m(\tau)}{K_m(1)}.$$
(4.38)

Hence, using

$$-K_{-n-1}(\tau) = K'_{-n}(\tau) - \frac{n}{\tau}K_{-n}(\tau),$$

$$\frac{d}{d\tau} \left[\tau^{n+1}K_{-n-1}(\tau)\right] = -\tau^{n+1}K_{-n}(\tau),$$

we have

$$\int_{0}^{1} d\tau \tau^{n+1} \frac{d_{-n}}{4} \frac{K_{-n}(\tau)}{K_{-n}(1)} = \frac{d_{-n}}{4K_{-n}(1)} \int_{0}^{1} \frac{d}{d\tau} \left[ -\tau^{n+1} K_{-n-1}(\tau) \right] 
= \frac{d_{-n}}{4K_{-n}(1)} \int_{0}^{1} \frac{d}{d\tau} \left[ \tau^{n+1} K'_{-n}(\tau) - \frac{n}{\tau} \tau^{n+1} K_{-n}(\tau) \right] 
= \frac{1}{4} \left[ d_{-n} \frac{K'_{-n}(1)}{K_{-n}(1)} - n d_{-n} \right], \ n \ge 0,$$
(4.39)

which is indeed (4.30).

#### **4.5.3** Appendix III (Verification of (4.31))

Integration by parts and (4.34) yield:

$$\begin{split} \int_{\rho}^{\tau} \mathrm{d}\tau \tau^{-m+1} \hat{v}_{m}(t) &= \frac{1}{4} \int_{\rho}^{\tau} \mathrm{d}\tau \ \tau^{-m+1} \left[ \frac{\mathrm{d}^{2} \hat{u}_{m}(\tau)}{\mathrm{d}\tau^{2}} + \frac{1}{\tau} \frac{\mathrm{d} \hat{u}_{m}(\tau)}{\mathrm{d}\tau} - \frac{m^{2}}{\tau^{2}} \hat{u}_{m}(\tau) \right] \\ &= \frac{1}{4} \left[ \frac{\mathrm{d} \hat{u}_{m}(\tau)}{\mathrm{d}\tau} \tau^{1-m} + m \hat{u}_{m}(\tau) \tau^{-m} - \frac{\mathrm{d} \hat{u}_{m}(\rho)}{\mathrm{d}\rho} \rho^{1-m} - m \hat{u}_{m}(\rho) \rho^{-m} \right]. \end{split}$$

Hence, equation (4.31) becomes

$$\begin{array}{ll} u_z & = & \frac{1}{2} \sum_{m=-\infty}^{\infty} \frac{z^{m-1}}{\tau^{m-1}} \left[ \frac{d\hat{u}_m(\tau)}{d\tau} + \frac{m}{\tau} \hat{u}_m(\tau) \right] - \frac{1}{2} \sum_{m=-\infty}^{\infty} z^{m-1} \left[ \tau^{1-m} \frac{d\hat{u}_m(\tau)}{d\tau} + m \hat{u}_m(\tau) \tau^{-m} \right] \\ & + \frac{1}{2} \sum_{m=-\infty}^{\infty} z^{m-1} \left[ \rho^{1-m} \frac{d\hat{u}_m(\rho)}{d\rho} + m \rho^{-m} \hat{u}_m(\rho) \right] \\ & = & \frac{1}{2} \sum_{m=-\infty}^{\infty} z^{m-1} \left[ \rho^{1-m} \frac{d\hat{u}_m(\rho)}{d\rho} + m \rho^{-m} \hat{u}_m(\rho) \right] \end{array}$$

or

$$u_z(z) = \frac{1}{2} \sum_{m=-\infty}^{\infty} e^{i(m-1)\theta} \left[ \frac{d\hat{u}_m(\rho)}{d\rho} + \frac{m}{\rho} \hat{u}_m(\rho) \right]$$

which is indeed valid by (4.18).

# **4.5.4** Appendix IV (Verification of (4.33))

Let  $q = \frac{1}{4}$ . Instead of (4.36), we choose

$$u(\tau,\phi) = \sum_{m=-\infty}^{\infty} c_m K_m(\tau) e^{\mathrm{i}m\phi},$$

where  $K_m(\tau)$  is the modified Bessel function of 2nd kind.

In this case,

$$\frac{\mathrm{d}\hat{u}_m( au)}{\mathrm{d} au} = c_m K_m'( au),$$

and,

$$\hat{v}_m(\tau) = \frac{c_m}{4} K_m(\tau).$$

Hence,

$$\begin{split} \int_0^\tau \mathrm{d}\tau \ \tau^{n+1} \frac{c_{-n}}{4} K_{-n}(\tau) &= \frac{c_{-n}}{4} \int_0^\tau \frac{d}{d\tau} \left[ \tau^{n+1} K'_{-n}(\tau) - \frac{n}{\tau} \tau^{n+1} K_{-n}(\tau) \right] \\ &= \frac{1}{4} \tau^{n+1} \left[ c_{-n} K'_{-n}(\tau) - \frac{n}{\tau} c_{-n} K_{-n}(\tau) \right], \ n \geq 0, \end{split}$$

which is indeed (4.33).

# Chapter 5

# Implementation of two 2D PET analytic reconstruction algorithms in STIR and their performance evaluation

In Software for Tomographic Image reconstruction (STIR), an object-oriented library implemented in C++ for 3D Positron Emission Tomography (PET) and Single Photon Emission Computed Tomography (SPECT) reconstruction, we implement a PET analytic reconstruction algorithm based on the gridding method (GRD2D), and we improve the implementation in STIR of another algorithm based on spline interpolation (SRT2D). We perform comparisons in terms of speed and image quality, in particular contrast for both 'hot' and 'cold' Regions of Interest (ROIS) between these two algorithms and the prevailing analytic reconstruction algorithm Filtered Backprojection (FBP2D) included in STIR. SRT2D and GRD2D prove to be strong alternatives to FBP2D in terms of image quality, and also GRD2D has significant computational advantage over FBP2D.

## 5.1 Prerequisites

#### **5.1.1 2D Geometry**

In this chapter, we consider a 2D PET scanner; see chapter 6 for the more general 3D case. The scanner consists of gamma-ray detectors arranged in the circumference of a circle. The scanner measures emissions along lines connecting pairs of detectors. We call such a line LOR (Line of Response). We symbolize the angle of an LOR with the x axis with  $\theta$ . Typically we have the same number of LORs for each angle  $\theta$ . We symbolize them with  $n_{\rm rad}$  (or sp) and call them *number of tangential positions*. We symbolize the number of angles  $\theta$  with  $n_{\rm ang}$  (or sth) and call them *number of views*. Theoretically a scanner with N number of detectors can have N(N-1)/2 number LORs, but this can vary vastly.

For convenience we will define a rotated coordinate system  $(\rho, \tau)_{\theta}$ . The transformation from the rotated to the standard coordination system is given by

$$x = \tau \cos \theta - \rho \sin \theta$$
,  $y = \tau \sin \theta + \rho \cos \theta$ ,

and the inverse by

$$\tau = x\cos\theta + y\sin\theta, \quad \rho = -x\sin\theta + y\cos\theta.$$
 (5.1)

[61]

Typically (and almost always) the views  $\theta_i$  of a scanner are equidistant, i.e.  $d_{\rm ang} = \pi/n_{\rm ang}$ . The same does not hold for the tangential positions; however, when they are equidistant, then  $d_{\rm rad} = 2r_{\rm scn}/n_{\rm rad}$ , where  $r_{\rm scn}$  is the scanner ring radius, and we say that the data are *arc corrected* (this can be easily achieved with a linear interpolation).

Finally we will symbolize by f(x,y) the activity in the point (x,y), and might refer to f as the *image*. The emissions along the Line of Response (LOR) with angle

 $\theta$  and tangential position  $\rho$  are given by the Radon transform

$$(\mathcal{R}f)(\boldsymbol{
ho};\boldsymbol{ heta}) = \int_{-r_{\mathrm{scn}}}^{r_{\mathrm{scn}}} f(\boldsymbol{ au}, \boldsymbol{
ho}; \boldsymbol{ heta}) \, \mathrm{d} \boldsymbol{ au}.$$

The function

$$(\mathcal{R}_{\theta}f)(\cdot) = (\mathcal{R}f)(\cdot, \theta)$$

is called the projection of f at angle  $\theta$ .

The Radon transform is intimately related to the Fourier transform by the projection slice theorem [62], which states that

$$\widehat{\mathcal{R}_{\theta}f}(r) = \widehat{f}(r\cos\theta, r\sin\theta),$$

i.e. the 1D Fourier transform of the projections  $(\mathcal{R}_{\theta}f)(\cdot)$  of angle  $\theta$  is the 2D Fourier transform of f(x,y) evaluated at a line of angle  $\theta$  passing through the domain origin.

The goal of image reconstruction in PET is to reconstruct the activity image f(x,y) using the measured radionuclide emissions along LORs, i.e. calculate f given its Radon transform  $\mathcal{R}f$ . However, it is impossible to reconstruct a continuous function from discrete samples of its Radon transform. In practice, the image is discretized, and the reconstruction is performed on a grid of pixels to approximate the continuous function.

#### **5.1.2** Direct Fourier Method

We can fill the Fourier space F(u,v) of f by calculating the Fourier transform of  $g(\rho;\theta)$  for all available  $\theta$ . In order to reconstruct f(x,y) the fastest method is to calculate the 2D inverse Fourier transform of F. This is called Direct Fourier Method (DFM).

Besides DFM there are other analytic methods for reconstruction which rely on the backprojection of each pixel  $(x_i, y_i)$  (Backprojection-Filtering [63], Filtered Backprojection [64]). Other non-analytic (iterative) reconstruction methods include Algebraic Reconstruction Techniques (ART) [65], Maximum-Likelihood Estimation Method (MLEM) [66] and Ordered Subset Expectation Maximization (OSEM) [67].

The main difficulty of DFM is that the available samples in the Fourier space of f –taken by the projection-slice theorem– (i.e.  $(r_{\rm ip}\cos\theta_{\rm ith},r_{\rm ip}\sin\theta_{\rm ith}))$  are not uniformly distributed, while in order to reconstruct f we need them to lie on a regular grid (typically  $(r_{\rm ix},r_{\rm iy})$ ). For example, for a sample scanner consisting of 16 detectors and 8 tangential positions the available and the required samples are illustrated in Figure 5.1.

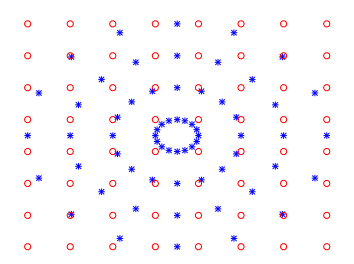


Figure 5.1: o regular grid, \* samples provided by projection slice theorem

Many methods exist for the estimation of the Fourier samples onto the regular grid. Two-dimensional interpolation is the simplest and fastest method but might not yield satisfactory results. A more accurate (but slower) method is gridding which is analyzed below.

# 5.2 2D Gridding algorithm (GRD2D)

We implement in STIR [68] GRD2D, a 2D PET reconstruction algorithm using the Fourier Slice Theorem and the gridding method. We choose a variant for the gridding method [69] to reconstruct f with bounded support from  $\hat{f}$ , which is particularly suited to PET reconstruction. The gridding method is used to reconstruct the image f from its Fourier transform  $\hat{f}$ , sampled on a non-uniform grid. The process begins by convolving  $\hat{f}$  with a window function  $\hat{w}$  to produce  $\hat{g}$ , which smooths the non-uniform samples. Following this, the function g is computed by applying the inverse Fourier transform to  $\hat{g}$ , and finally, the image f is obtained by dividing g by the window function w to correct for the initial weighting. The steps of the algorithm, as described in [69], follow:

**Step 1** Compute samples of  $\hat{f}$  from the available projections

86

Using the notation introduced in section 5.1.1, and for

$$-n_{\rm rad}/2 \le \mu < n_{\rm rad}/2, \ 0 \le \nu < n_{\rm ang},$$
 (5.2)

the projections measured by the scanner are

$$p_{\mu,\nu} = (\mathcal{R}_{\theta_{\nu}} f)(r_{\mu}), \quad (r_{\mu}, \theta_{\nu}) = (\mu d_{\text{rad}}, \nu d_{\text{ang}}).$$

Choosing an FFT-friendly integer  $N_{\text{rad}} \ge n_{\text{rad}}$ , say

$$N_{\text{rad}} = \beta_{\text{rad}} n_{\text{rad}}, \quad \beta_{\text{rad}} \in \mathbb{R}, \quad \beta_{\text{rad}} \ge 1,$$

(5.2) becomes

$$-N_{\rm rad}/2 \le \mu < N_{\rm rad}/2, \ 0 \le \nu < n_{\rm ang}.$$
 (5.3)

Padding (filling with zeros up to the desired length) each projection  $p_{\mu,\nu}$  at both ends with  $(N_{\rm rad}-n_{\rm rad})/2$  zeros and applying 1-D FFT, in view of the projection slice theorem, we get

$$\hat{p}_{\mu,\nu} = \hat{f}(r_{\mu}\cos\theta_{\nu}, r_{\mu}\sin\theta_{\nu}), \quad r_{\mu} = \mu/(N_{\text{rad}}d_{\text{rad}}),$$

where  $d_{\text{rad}}$  is the pixel size. Thus we have obtained the samples  $\hat{p}_{\mu,\nu}$  in the polar grid formed by the sampling points

$$u^{\mu,\nu} = (r_{\mu}\cos\theta_{\nu}, r_{\mu}\sin\theta_{\nu}),$$

in the disk

$$D = \{ u \in \mathbb{R}^2 | |u| \le 1/(2d_{\text{rad}}) \}.$$

In the gridding method the reconstruction interval is of the form

$$R = [-Md/2, Md/2] \times [-Md/2, Md/2], M \in \mathbb{R}^+.$$

As we assume f to be strictly space-limited to R, i.e. we perform a full reconstruction, choosing  $M = M_{\text{rad}}$  and  $d = d_{\text{rad}}$ ,

$$R = [-r_{\rm scn}, r_{\rm scn}] \times [-r_{\rm scn}, r_{\rm scn}].$$

**Step 2** Numerically compute  $\hat{g}$  using convolution of  $\hat{f}$  with a window function  $\hat{w}$  on K intervals.

To compute the convolution product

$$\hat{g}(u) = (\hat{w} * \hat{f})(u) = \int_{\mathbb{R}^2} \hat{w}(u - u') \,\hat{f}(u') \,du'$$
 (G1)

on the grid points  $\{l/(N_{\rm rad}d_{\rm rad}) \mid l=(l_1,l_2),-N_{\rm rad}/2 \leq l_1,l_2 \leq N_{\rm rad}/2\}$  in D, we partition D such that each sampling point  $u^{\mu,\nu}$  lies in exactly one cell, and we approximate (G1) by

$$\hat{g}(l/(N_{\rm rad}d_{\rm rad})) = \frac{d_{\rm rad}}{N_{\rm rad}d_{\rm rad}} \sum_{\nu} \sum_{\mu} \sigma_{\mu} \hat{w}(l/(N_{\rm rad}d_{\rm rad}) - T_p(r_{\mu}, \theta_{\nu})) \hat{p}_{\mu,\nu}, \quad (**)$$

where  $\sigma_{\mu} = |\mu|$  if  $\mu > 0$  and  $\sigma_0 = 1/4$ , and the transformation  $T_p : \mathbb{R} \times [0, \pi) \to \mathbb{R}^2$  with  $T_p(\rho, \theta) = (\rho \cos \theta, \rho \sin \theta)$  turns (G1) to polar coordinates (since we have a polar grid). Outside the disk D, we put  $\hat{g}_l = 0$ .

For the windowing function  $\hat{w}$ , we will choose a separable 2D Kaiser-Bessel window

$$\widehat{w}_{\mathrm{KB}}(\alpha r, \nu; s) = \chi_{[-\nu, \nu]}(s) \frac{I_0\left(2\pi a r \nu \sqrt{1 - (s/\nu)^2}\right)}{2\nu}$$

where  $\alpha \geq 1$  with  $\alpha^2 \hat{w} = \int_{\mathbb{R}^2} \hat{w}(u) \, du$  is the "equivalent width" of the window  $\hat{w}$ ,  $I_0$  the zero-order modified Bessel function, and

$$r = n_{\rm rad} d_{\rm rad}/2$$
,  $v = K/(2\beta n_{\rm rad} d_{\rm rad})$ .

Its support is in the interval  $V = [-K/(2\beta n_{\rm rad}d), K/(2\beta n_{\rm rad}d)]^2$  for some

 $K \in \mathbb{Z}_+$  with  $K/(\beta n_{\rm rad}) \ll 1$ , i.e. it is "small".

The Kaiser-Bessel window has a jump discontinuity at  $s=\pm v$ , and the relative height of the jump is  $RH=I_0(2\pi\alpha rv)$ . To reduce RH we need to increase the product  $\alpha v$  (r is no longer at our disposal); however increasing  $\alpha$  will also widen w and hence narrow  $\hat{w}$  (as  $\hat{w}$  and w are reciprocal to each other), and also w must stay away from zero in R, whereas increasing v will widen  $\hat{w}$  but simultaneously increase the computational load. Hence, we cannot simply widen the window for more smoothing effect: according to [69] for PET the optimal parameters are  $\alpha=2$  for window width and K=4 for the support of the convolution.

#### Step 3 Compute g using the 2D inverse Fourier transform.

Evaluating at  $x = kd_{\text{rad}}$ ,  $k = (k_1, k_2)$  for  $-N_{\text{rad}}/2 \le k_1, k_2 < N_{\text{rad}}/2$ , the truncated Fourier series resulting from applying the dual version of the Poisson summation formula to g, and shifting the summation index, yields

$$g'(kd_{\text{rad}}) = \exp(-i\pi k \cdot 1)(N_{\text{rad}}d_{\text{rad}})^{-1} \sum_{l=0}^{N_{\text{rad}}-1} \hat{g}((l-N_{\text{rad}}/2)/d) \exp(i2\pi k(l/N_{\text{rad}})),$$

$$0 \le k < N_{\text{rad}}. \quad (G2)$$

In our full reconstruction case, f and g are strictly space-limited to R, and there is no aliasing error even if we choose Q = R, where  $Q = [-N_{\rm rad}d_{\rm rad}/2,N_{\rm rad}d_{\rm rad}/2]$ .

Applying the inverse DFT to the sequence  $\{\hat{g}_{l-N_{\rm rad}/2}\}_{l=0}^{N_{\rm rad}-1}$ , which we have estimated in the previous step, we can compute  $g'(kd_{\rm rad})$  for  $0 \le k < N_{\rm rad}$ , and then extend it onto all  $k \in \mathbb{Z}^2$ , and in particular to  $-N_{\rm rad}/2 \le k < N_{\rm rad}/2$ , given that g' is periodic with period  $N_{\rm rad}d_{\rm rad}$ .

## **Step 4** Compute f = g/w.

Stipulating the weights are positive and bounded away from zero in R, holds

$$f(kd_{\rm rad}) = g' \Big|_{k = -N_{\rm rad}/2}^{N_{\rm rad}/2 - 1} / w(kd_{\rm rad}), -n_{\rm rad}/2 \le k < n_{\rm rad}/2.$$
 (G3)

#### 5.2.1 Implementation details of Step 2

For efficiency we are saving the Cartesian grid coordinates in a matrix  $\{l/(N_{\rm rad}d_{\rm rad}) \mid l=(l_1,l_2),-N_{\rm rad}/2 \leq l_1,l_2 \leq N_{\rm rad}/2\}$  of the input data polar grid.

For the implementation of the approximation of the convolution by (\*\*), for every view and for every tangential position and for every x-point of the reconstructed image we calculate the x-coordinate  $T_x$  of the 2D vector  $\frac{1}{N_{\text{rad}}d_{\text{rad}}} - T_p(\rho_{\mu}, \theta_{V})$ . If  $T_x$  falls into the support of the window used in convolution, we calculate the value of the Fourier transform of the Kaiser-Bessel window at  $T_x$ . For every y-point of the reconstructed grid, we calculate  $T_y$ . If  $T_y$  falls inside the window used in convolution, we calculate the value of the Fourier transform of the Kaiser-Bessel window at  $T_y$  and the quadrature part suggested by equation (\*\*). Let us note that, Kaiser-Bessel window is separable, thus allowing us to do this. This part of the implementation can be vastly improved by calculating explicitly the intervals where the support of the window function used in the convolution is non-zero (it leads to the dropping of two loops).

#### 5.2.2 Further notes on (STIR) implementation

For the 1D and 2D Fourier transforms we use STIR's DFT implementation, which we append with a small function fftshift that reorders the initial data. Assuming that the number of tangential positions is even, GRD2D code should work for every scanner.

In case the length of the interpolation window is K = 1, the gridding method reduces to a simple bilinear interpolation, which makes the code dramatically faster. However, as no less than K=4 gives results satisfactory for medical applications (K=6 is as accurate as Filtered Backprojection) [69], the interpolation algorithm for K=1 was not implemented.

Only direct sinograms (i.e., segment 0) are used, since GRD2D is a 2D code. Therefore, the number of z positions in the final image will be equal to the number of axial positions in segment 0. By default, when setting z output size := -1

for the case of FBP2D (and in particular in AnalyticReconstruction.cxx, which GRD2D also extends), the output image consists of  $2 \times$  number of axial positions -1 elements. This indicates that number of axial positions -1 extra images are reconstructed through linear interpolation between neighboring sinograms (commonly referred to as cross-planes).

The computational burden of computing the convolution can be effectively parallelized both in shared and distributed memory architectures.

As STIR's FBP2D has a Ramp-Hamming filter, i.e. an enhanced variant beyond the Ramp filter (the latter being an integral component of the mathematical formulation of FBP), we have created a simple low-pass filter that can be optionally applied depending on the respective parameter set in the parameter file.

# 5.3 Spline Reconstruction Technique (SRT2D) algorithm

## 5.3.1 Mathematical formulation and algorithm steps

SRT2D was introduced in [70], and the content of this subsection will be taken from this paper. This algorithm reconstructs the image  $f(x_1, x_2)$  from its Radon transform data  $\hat{f}(\rho, \theta)$ . It does so by first approximating the projection data with natural cubic splines, calculating the Hilbert transform of the spline-interpolated data, and then performing numerical integration over the angle  $\theta$  to obtain the final reconstructed image.

Although we use the available PET data, the algorithm is fundamentally designed to work with CT data, specifically the Radon transform of attenuation, as it was originally part of a SPECT algorithm. Since after precorrections, both the PET sinogram and CT data are line integrals (Radon transforms) of some underlying function, the algorithm designed to process the Radon transform of attenuation (CT data) can still work with the PET sinogram, which represents line integrals of the radiotracer distribution; This is because in PET, attenuation is independent of the location of the source along the line between two detectors and can therefore be

factored out.

Taking the real part of the inverse Radon transform yields

$$f(x_1, x_2) = -\frac{1}{4\pi^2} \int_0^{2\pi} h_{\rho}(\rho, \theta) d\theta,$$

with the Hilbert transform

$$h(\rho,\theta) = \oint_{-\infty}^{\infty} \frac{\hat{f}(\rho',\theta)}{\rho'-\rho} d\rho'.$$

Suppose that  $\hat{f}(\rho, \theta)$  is given, for every  $\theta$ , at n equally spaced points  $\rho_i \in [-1, 1]$ , i.e. suppose that  $\hat{f}_i = \hat{f}(\rho_i, \theta)$  are known. In order to calculate numerically  $f(x_1, x_2)$  we perform the following steps.

**Step 1** Calculation of the natural cubic spline of  $\hat{f}(\rho, \theta)$ .

In each interval  $[\rho_i, \rho_{i+1}]$  we approximate  $\hat{f}(\rho, \theta)$  calculating the natural cubic spline  $S_i(\rho, \theta)$  (in  $\rho$ ) by subroutine splint from Numerical Recipes [61], which uses the second derivatives  $\hat{f}_i''$  of  $\hat{f}(x,y)$  with respect to  $\rho$  at  $\rho = \rho_i$ , calculated themselves by subroutine spline from Numerical Recipes [61].

**Step 2** Calculation of  $h_{\rho}(\rho, \theta)$ .

For  $\rho \neq \rho_i, \rho_{i+1}$  holds

$$h_{\rho}(\rho,\theta) = \frac{\partial}{\partial \rho} \sum_{i=1}^{n-1} \int_{\rho_{i}}^{\rho_{i+1}} \frac{S_{i}(\rho',\theta)}{\rho' - \rho} d\rho',$$

$$= \sum_{i=1}^{n-1} \left( \frac{\hat{f}_{i}}{\rho_{i} - \rho} - \frac{\hat{f}_{i+1}}{\rho_{i+1} - \rho} - \frac{1}{4} (\rho_{i} - 3\rho_{i+1} + 2\rho) \hat{f}_{i}'' - \frac{1}{4} (3\rho_{i} - \rho_{i+1} - 2\rho) \hat{f}_{i+1}'' \right)$$

$$+ \left[ \frac{\hat{f}_{i} - \hat{f}_{i+1}}{\rho_{i} - \rho_{i+1}} - \frac{1}{6} (\rho_{i} - \rho_{i+1} - \frac{3(\rho_{i+1} - \rho)^{2}}{\rho_{i} - \rho_{i+1}}) \hat{f}_{i}'' \right]$$

$$+ \frac{1}{6} (\rho_{i} - \rho_{i+1} - \frac{3(\rho_{i} - \rho)^{2}}{\rho_{i} - \rho_{i+1}}) \hat{f}_{i+1}'' \right] \ln \left| \frac{\rho_{i+1} - \rho}{\rho_{i} - \rho} \right|,$$

$$(5.4)$$

where  $\rho$  is calculated for any  $x_1$  and  $x_2$  (for any  $\theta$ ) using (5.1).

Step 3 Numerical integration of (5.4).

We calculate

$$\int_0^{2\pi} h_{\rho}(\theta) d\theta = \frac{2\pi}{N} \sum_{i=0}^{N-1} h_{\rho}\left(\frac{2\pi i}{N}\right),\tag{5.5}$$

and multiplying by  $-\frac{1}{4\pi^2}$  we get  $f(x_1, x_2)$ .

#### 5.3.2 Symmetries

We will explain SRT2D's symmetries-related speeding up technique [71].

Let  $\{x_{1_{k_1}}\}_{k_1=1}^{sx}$ ,  $\{x_{2_{k_2}}\}_{k_2=1}^{sy}$ ,  $\{\rho_i\}_{i=1}^{sp}$  be uniform partitions of [-1,1], let  $\{\theta_j\}_{j=1}^{sth}$  be a uniform partition of  $[0, \pi \frac{sth-1}{sth}]$ , and

$$\rho = x_2 \cos \theta - x_1 \sin \theta. \tag{5.6}$$

The above partitions correspond to constant detector spacing. Then, the eight points

- $(x_{1_{k_1}}, x_{2_{k_2}}, \theta_j, \rho_k), (x_{1_{k_1}}, x_{2_{sx-k_2+1}}, \theta_{sth-j+2}, \rho_k), (x_{1_{sx-k_1+1}}, x_{2_{k_2}}, \theta_{sth-j+2}, \rho_{sp-k}), (x_{1_{sx-k_1+1}}, x_{2_{sy-k_2+1}}, \theta_j, \rho_{sp-k}),$
- and either  $(x_{1_{k_2}}, x_{2_{k_1}}, \theta_{sth/2-j}, \rho_{sp-k}), (x_{1_{k_2}}, x_{2_{sx-k_1+1}}, \theta_{j-2-sth/2}, \rho_{sp-k}),$   $(x_{1_{sx-k_2+1}}, x_{2_{k_1}}, \theta_{j-2-sth/2}, \rho_k), \text{ and } (x_{1_{sx-k_2+1}}, x_{2_{sy-k_1+1}}, \theta_{sth/2-j}, \rho_k), \text{ for } 2 \leq j \leq \lceil \frac{sth}{2} \rceil,$
- or  $(x_{1_{k_2}}, x_{2_{k_1}}, \theta_{3*sth/2-j-1}, \rho_k)$ ,  $(x_{1_{k_2}}, x_{2_{sx-k_1+1}}, \theta_{sth/2+j-3}, \rho_k)$ ,  $(x_{1_{sx-k_2+1}}, x_{2_{k_1}}, \theta_{sth/2+j-3}, \rho_{sp-k})$ , and  $(x_{1_{sx-k_2+1}}, x_{2_{sy-k_1+1}}, \theta_{3*sth/2-i-1}, \rho_{sp-k})$ , for  $\lceil \frac{sth}{2} \rceil \leq j \leq sth-1$ ,

have the same  $\ln |\rho - \rho_{i+1}|$  value.

Thus, by executing the algorithm for  $k_1$  from 1 to  $\lceil \frac{sx}{2} \rceil$  and for  $k_2$  from 1 to  $k_1$ , we only need to compute once the logarithm associated with the above eight points (the logarithms associated with j=1 must be computed separately).

#### 5.3.2.1 Prerequisite relations and their proofs

To illustrate the validity of the above assertion, we need to make use of the following relations, which hold for  $j \ge 2$ :

$$\rho(x_{1_{k_1}}, x_{2_{k_2}}, \theta_j) = -\rho(x_{1_{sx-k_1+1}}, x_{2_{k_2}}, \theta_{sth-j+2}), \tag{5.7}$$

$$\rho(x_{1_{k_1}}, x_{2_{k_2}}, \theta_j) = \rho(x_{1_{k_1}}, x_{2_{sv-k_2+1}}, \theta_{sth-j+2}), \tag{5.8}$$

$$\rho(x_{1_{k_1}}, x_{2_{k_2}}, \theta_j) = -\rho(x_{1_{sx-k_1+1}}, x_{2_{sy-k_2+1}}, \theta_j), \tag{5.9}$$

$$\rho_i - \rho = -(\rho_{sp-i+1} - (-\rho)) = -(\rho_{sp-i+1} + \rho), \tag{5.10}$$

$$\sum_{j=2}^{sth} \sum_{i=1}^{n-2} D_{i,j} \ln \left| \rho(x_{1_{k_1}}, x_{2_{k_2}}, \theta_j) - \rho_{i+1} \right| = \sum_{j=sth}^{2} \sum_{i=1}^{n-2} D_{i,sth-j+2} \ln \left| \rho(x_{1_{k_1}}, x_{2_{k_2}}, \theta_{sth-j+2}) - \rho_{i+1} \right|,$$
(5.11)

where  $D_{i,j} = [D_i(\rho, \theta_j) - D_{i+1}(\rho, \theta_j)]$ , and  $\sum_{j=sth}^2$  denotes summation with decreasing, instead of increasing order.

Furthermore, the following two relations are also required for proving the assertion.

$$\rho(x_{1_{k1}}, x_{2_{k2}}, \theta_j) = -\rho(x_{1_{k2}}, x_{2_{k1}}, \theta_{sth/2-j}) \quad \text{for} \quad 1 \le j \le \left\lceil \frac{sth}{2} \right\rceil$$
 (5.12)

$$\rho(x_{1_{k1}}, x_{2_{k2}}, \theta_j) = \rho(x_{1_{k2}}, x_{2_{k1}}, \theta_{3*sth/2-j-1}) \text{ for } \left\lceil \frac{sth}{2} \right\rceil \le j \le sth - 1 \quad (5.13)$$

Assuming  $\{x_{1_{k_1}}\}=\{x_{2_{k_2}}\}$ , as is the case with reconstructed images, we therefore can calculate only the logarithm for  $(x_{1_{k_1}},x_{2_{k_2}})$  and use it also for  $(x_{2_{k_2}},x_{1_{k_1}})$ 

Properties (5.7)-(5.9) are shown in Figure (7.7), for specific values of  $x_{1_{k_1}}$ ,  $x_{2_{k_2}}$  and  $\theta_i$ .

The proof of equations 5.7 and 5.8, is based on the following facts:

1. 
$$x_{1_{k_1}} = x_1(k_1) = -x_1(sx - k_1 + 1), x_{2_{k_2}} = x_2(k_2) = -x_2(sx - k_2 + 1).$$
 This is a straightforward consequence of the fact that  $\{x_{1_{k_1}}\}$  and  $\{x_{2_{k_2}}\}$  are uniform partitions of  $[-1,1]$ .

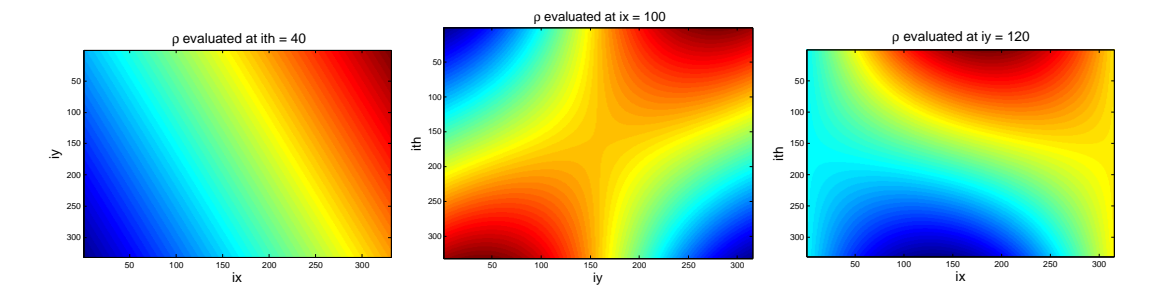


**Figure 5.2:** Examples of symmetries displayed along three planes corresponding to the discretized array of  $\rho$  values: (left) symmetries in the  $x_1x_2$  plane for  $\theta(40)$ , (center) symmetries in the  $x_2\theta$  plane for  $x_1(100)$ , (right) symmetries at the  $x_1\theta$  plane for  $x_2(120)$ .

2. 
$$\cos(\theta_j) = \cos(\theta(j)) = -\cos(\theta(sth - j + 2)), \sin(\theta_j) = \sin(\theta(j)) = \sin(\theta(sth - j + 2)).$$

This is a straightforward consequence of the fact that  $\theta(j) = \pi - \theta(sth - j + 2)$ , since  $\{\theta_j\}_{j=2}^{sth}$  is a uniform partition of  $\left[\pi \frac{1}{sth}, \pi \frac{sth-1}{sth}\right]$ , and of the identities  $\cos(\theta_j) = -\cos(\pi - \theta_j)$  and  $\sin(\theta_j) = \sin(\pi - \theta_j)$ .

Equation 5.9 follows from equations 5.7 and 5.8. Equation 5.10 is a straightforward consequence of the fact that  $\{\rho_i\}$  is a uniform partition of [-1,1]. In equation 5.11 we replace j with sth - j + 1, and traverse  $\{\theta_j\}$  in the opposite direction.

Equations 5.12 and 5.13 follow from equation 5.6 for  $\theta$  and  $\frac{\pi}{2} - \theta$ , and for  $\frac{\pi}{2} + \theta$  and  $\pi - \theta$ , where  $\theta \in (0, \frac{\pi}{2})$ , respectively.

#### 5.3.2.2 Patterns

Further acceleration of the implementation can be achieved by making use of the following patterns:

- 1. In each step (except the first) only the number  $D_{i+1}$  should be calculated and stored for use in the next step, since  $D_i$  corresponds to  $D_{i+1}$  of the previous iteration.
- 2. Simplification of  $D_i$  leads to formula  $D_i = \frac{\widehat{f_i} \widehat{f_{i+1}}}{\rho_i \rho_{i+1}} \frac{1}{6} \left( \rho_i \rho_{i+1} \frac{3(\rho_{i+1} \rho)^2}{\rho_i \rho_{i+1}} \right) \widehat{f}_i'' + \frac{1}{6} \left( \rho_i \rho_{i+1} \frac{3(\rho_i \rho)^2}{\rho_i \rho_{i+1}} \right) \widehat{f}_{i+1}''$  Therefore, at each iteration (except the first), only the coefficient of  $\widehat{f}_i''$  must be calculated and stored until the next iteration, since the coefficient of  $\widehat{f}_{i+1}''$

corresponds to the coefficient  $\hat{f}_i^{"}$  of the previous iteration.

#### **5.3.3** STIR implementation improvements

A first implementation of SRT2D in STIR took place in [71]. We present the improvements of the new implementation.

#### 5.3.3.1 Compact form of the code

We have created a function that calculates the derivative of Hilbert transform for a specific  $\rho$  and  $\theta$ , and used this function to calculate all Hilbert transforms. Special care should be put in the input data for this function each time. Compact form speeds up the code by 30% percent (we did not do less calculations, but simply lessened the amount of code).

#### 5.3.3.2 Input data read as viewgrams instead of as sinograms

Sinogram is the measurements of the scanner for (a particular segment and) a particular axial position (and for all tangential positions and all views). Viewgram is the measurements of the scanner for (a particular segment and) a particular view (and for all tangential positions and all axial positions).

The main difference in the code when reading input data as viewgrams instead of sinograms is that we are reading the data for a particular view  $(\theta)$  each time. Therefore the first loop has to be along the views. Derivatives of the data and the quantity 'termC' are now calculated for a specific view  $(\theta)$  (instead of a specific axial position in the case of sinogram). Second and third loops are along  $x_1$  and  $x_2$  (as in the sinogram code). Inside the third loop we calculate  $\log |p_i - x|$  for the particular  $x = x(\theta, x_1, x_2)$  (where p denotes the partition for tangential positions). And the final loop is along the axial positions (instead of the views which we had in the sinogram code). We are using the already-computed values of the logarithm for ALL axial positions. Another significant change is that the value of the function calculating Hilbert derivative for the particular  $\theta, x_1, x_2$  (and axial position) is directly added to the final image (in the sinogram case, these values were stored in a vector of length sth, and were summed and assigned to the image after the completion of fourth loop.)

Reading input data as viewgrams instead of sinograms, led to the improvement of speed (35%). The function calculating the derivative of Hilbert transform requires the time consuming calculation of  $\log |p_i - x|$  for  $i = 1 \dots sp$ , where sp is the number of tangential positions, but x depends only on  $x_1, x_2$  and  $\theta$ , and not on the axial positions. Therefore we calculate  $\log |p_i - x(\theta, x_1, x_2)|$  for particular  $x_1, x_2$ , and  $\theta$  and use the value for ALL axial positions. Note that we can make use of the values of the logarithm, because the last loop of our algorithm is over axial positions, since we are reading our data as viewgrams. (In the case of sinograms, the last loop has to be along the views( $\theta$ )).

Reading input data as viewgrams instead of sinograms improved the speed by 35

#### 5.3.3.3 Variable pixel-size and number of pixels

By changing number of pixels, we change the area to be reconstructed. We changed the limits of the partition for  $x_1$  and  $x_2$  accordingly, in particular we set the partition ends as -sx/(sp+1) and -sx/(sp+1), respectively, where sx is the the number of pixels chosen by the user increased by 1, and sp the number of tangential positions. If sx < (sp+1), then we reconstruct area smaller than the default, if sx = sp+1, we reconstruct the default area, and if sx > sp+1 we reconstruct an area larger than the default. Let us note that in the latter case, the extra area added is simply filled with zeroes.

By changing the pixel-size, we change the norm of the partition for  $x_1$  and  $x_2$ , i.e. 2/(sp+1). The reason one might want to change the pixel-size would be to change the resolution, and therefore see the image with more (if the pixel-size is greater than 1) or less (if the pixel-size is less than 1) detail. Let us note this equals to changing voxel size (if ring diameter is to not be taken into account, as in our case). By dividing the norm of the partition by the pixel-size, we must also scale accordingly the values of the image. In particular since bin size cannot change as it depends on the scanner, if we change the voxel size, we must accordingly divide the image values, following STIR's convention for handling voxel size adjustments.(See Figure 5.3 below)

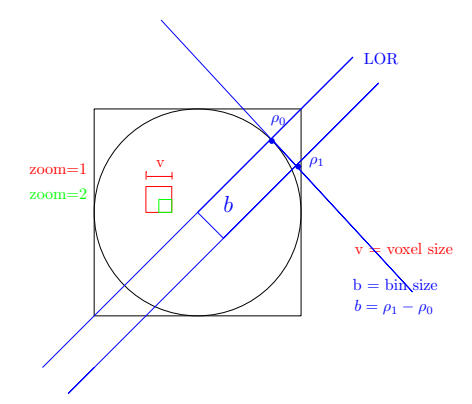


Figure 5.3: Zoom

#### 5.3.3.4 Parallelization of SRT2D

We have parallelized the algorithm using OpenMP (a shared-memory architecture). For compatibility with both OpenMP-enabled and non-OpenMP builds, conditional directives were used to include the necessary OpenMP-specific code. Additionally, default values for the number of threads were set, with a warning printed when only a single thread is used, similar to the approach taken in FBP2D.

The most efficient strategy is to parallelize the main loop (axial position in input read as sinogram, and views in input read as viewgram).

We have used a parallel for construct, with no wait clause.

For safety we have used a critical construct to access the data (from STIR's proj\_data\_ptr) and to write our data to image (STIR's VoxelsOnCartesianGrid), respectively. These do not seem to delay the code, and might even be unneccessary.

We maintained the automatic scheduling option, since special scheduling did not improve speed, as by the nature of the code work load for threads is balanced.

The overall improvement of parallelization on speed when using 4 threads is 50%.

### 5.3.3.5 Filtering

For the same reason we added a filter in GRD2D (see Step 5.2 of GRD2D), after experimentation with various filter choices and combinations, we also created a mixture of automated filters for SRT2D, in particular, a Wiener [72], a gamma [73] and a median [74] filter (the latter used with caution as it can potentially suppress

details). As default filters we have set the Wiener and the gamma filter; however, the reader is given the option to disable or enable each one of the available filters from the parameter file.

Wiener filter. It computes a local mean and variance for the whole slice. It then shifts the value of each pixel in the slice by the estimated noise level, averaging the computed local variance over the slice. To minimize the impact of noise on pixel intensity, the filter adjusts pixels based on noise and variance levels: pixels with high variance are lightly corrected to maintain detail while reducing noise, whereas pixels with variance similar to or lower than noise undergo stronger smoothing to suppress noise, balancing detail preservation and noise reduction.

Gamma filter. It adjusts the luminance of an image to either amplify or attenuate its contrast without altering the inherent spatial characteristics. Initially, it normalizes pixel values to a [0, 1] range, facilitating consistent application across varying image intensities. It then calculates the average pixel value of the image, disregarding pixels with absolute values less than a threshold (0.1) to focus on more significant data points. Based on this average, a gamma correction value is determined, aiming to adjust the average pixel intensity towards a predefined target (0.25). The correction is applied by raising each pixel's value to the power of the gamma value, effectively modifying the distribution of pixel intensities to enhance or reduce contrast. Pixels with negligible intensity are excluded from this power operation to maintain numerical stability. Finally, the image is denormalized, scaling the pixel values back to their original range.

Median filter. It processes an image one pixel at a time. It considers a local neighborhood around each pixel. For each pixel, a small window of neighboring pixels (in this case, a  $3 \times 3$  grid centered around the pixel in question) is taken; the values of those pixels are then collected and sorted. Then, the replaced pixel value is computed as the median of this ordered list of neighboring pixel values, which replaces the original pixel values. Since it is to be applied to EACH pixel, apart from the border pixels, the threshold is set effectively half-way through the sorted list, so by definition half the values are either lower or higher.

# 5.4 Comparison of algorithms

#### **5.4.1** Phantom and data creation

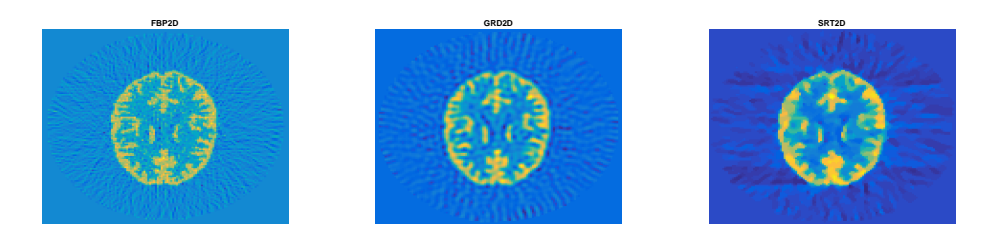
We will perform comparisons with the Hoffman Phantom, which in our case has a contrast ratio of 5:1 for grey matter vs. white matter and zero uptake in the ventricles; this represents a minor deviation from the typical 4:1 ratio used in standard FDG-PET brain scans.



Figure 5.4: Hoffmann brain phantom

Scanner interfiles and sinograms (with the addition of Poisson noise) were created in STIR; the latter together with the parameter files and the reconstructed images via a bash script allowing automation of the procedure.

We will compare GRD2D, SRT2D and STIR's FBP2D.



**Figure 5.5:** Reconstructed images of FBP2D, GRD2D, and SRT2D with a 0.1 Poisson noise scaling factor.

## **5.4.2** Image Quality Metrics

According to the NEMA standards [75], the contrast image quality metric is measured in Regions Of Interest (ROIs) with a diameter as close as possible to the inner diameter of each hot, cold and background sphere. To adjust this test for the Hoffmann phantom, we regard as 'hot sphere' the white matter (WM) ROI with

ground truth value 127, as 'cold sphere' the cerebrospinal fluid (CSF) ROI with value 0, and as 'background' the grey matter (GM) ROI with value 25.

In Matlab we detect the ROIs through blurring, and pixel intensity-based segmentation of the phantom, and save their coordinates to be applied to the reconstructed images. Blurring is used to avoid the inclusion of pixels that are close to each ROI's boundary; as it averages the pixel values within a neighborhood, the sharp transitions at the boundaries are smoothed out, causing the boundary pixels to take on intermediate values rather than retaining their original, distinct values. Then the ROIs are defined based on the specific pixel intensity values, i.e, ROIs corresponding to WM, CSF and GM are identified by selecting pixels with an intensity value of 127, 0 (within a circular region avoiding the zero-valued region surrounding the actual image data), and 25, respectively.

For STIR, to generate different levels of Poisson noise, the forward-projected sinograms were scaled with factors of 0.1, 0.5, and 0.9 before calling a Poisson random number generator. This will be denoted as "noise level" in the text below, where a lower noise level corresponds to a noisier image and a higher noise level corresponds to a less noisy image. For each algorithm, we generate 100 reconstruction images (realizations) at each noise level.

On each such set of 100 realizations, we apply 10 postfilters with increasing FWHM, e.g. gaussian with increasing standard deviation  $\sigma$ , and then calculate contrast as per the NEMA standard. Let us underline that we used the Nema contrast tests, as there is no specific standardized test equivalent to the NEMA standard that is universally applied to the Brainweb phantoms. Although we took great care to treat appropriately the complex boundaries of our phantom's ROIs, Nema tests could still be expected to potentially make contrast appear worse than it actually is for anatomically realistic phantoms.

#### 5.4.2.1 Metrics

The CoV is calculated as:

$$CoV = \frac{\sigma}{m}$$

where  $\sigma$  and m are the standard deviation and the mean, respectively, of the entire reconstructed image, averaged over all realizations per postfilter.

It should be noted that this calculation of CoV includes both noise-induced variability and the inherent non-uniformity of the phantom itself. Therefore, the CoV will not approach zero even in noiseless cases but will instead be limited by the CoV of the noiseless image.

As per the Nema standard, for the 'hot' ROI, the contrast  $Q_{H,r}$  for realization r is calculated by:

$$Q_{H,r} = \left(\frac{\frac{C_{H,r}}{C_{B,r}} - 1}{\frac{a_H}{a_B} - 1}\right)$$

where  $C_{H,r}$  is the average counts in the 'hot' ROI,  $C_{B,r}$  is the average counts in the 'background' ROI,  $a_H$  is the analytic activity concentration in the 'hot' ROI, i.e. 4, and  $a_B$  is the analytic activity concentration in the 'background' ROI, i.e. 1. The total contrast  $C_{\text{hot}}$  for the 'hot' ROI is determined by averaging the contrast over all realizations. Therefore, the ideal algorithmic reconstruction would give a value of  $Q_{H,r} = 1$ . A value of  $Q_{H,r}$  greater than one overestimates the contrast of the hot region.

Further, for the 'cold' ROI, the contrast  $Q_{C,r}$  for realization r is calculated by

$$Q_{C,r} = \left(1 - \frac{C_{C,r}}{C_{B,r}}\right)$$

where  $C_{C,r}$  is the average counts in the 'cold' ROI, and  $C_{B,r}$  is the average counts in the 'background' ROI. The total contrast  $C_{\text{cold}}$  for the 'cold' ROI is determined by averaging the contrast over all realizations. The analytic activity for the cold region is zero; therefore, the ideal value for  $Q_{C,r}$  would be one.

#### 5.4.2.2 Noise Sensitivity and Algorithm Behavior

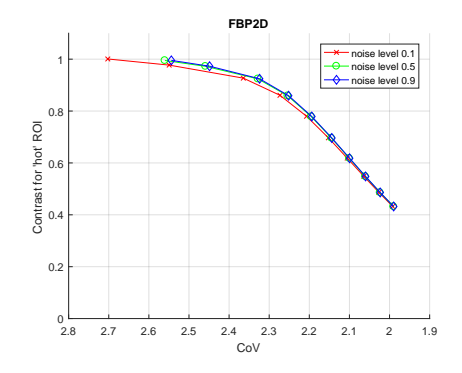
We will discuss noise dependence for each algorithm, particularly how contrast and CoV vary across noise levels and postfilter strengths.

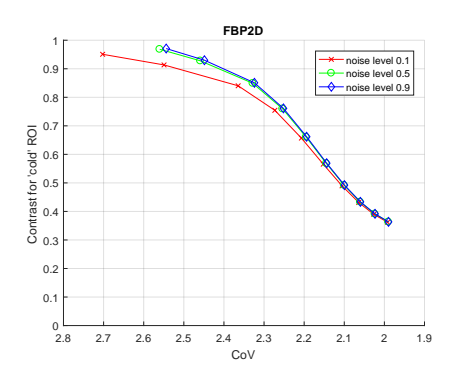
For each algorithm, we plot contrast (as per the NEMA standard) versus the Coefficient of Variation (CoV) for each noise level, as defined in subsection 5.4.2.1.

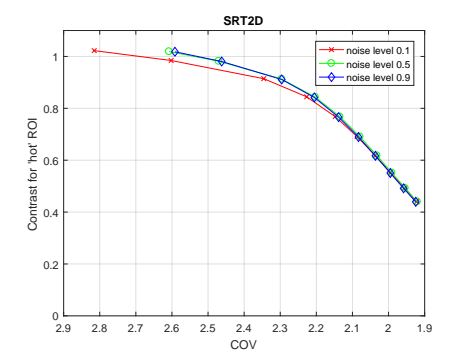
It should be noted that this calculation of CoV includes both noise-induced variability and the inherent non-uniformity of the phantom itself. Therefore, the CoV will not approach zero even in noiseless cases but will instead be limited by the CoV of the noiseless image.

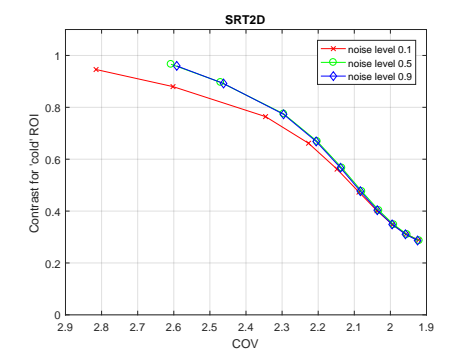
Reversing the CoV axis, we observe that for lower CoV (corresponding to higher postfilter values), all algorithms become less sensitive to noise, i.e. as the image gets more blurred/smoothed each algorithm converges to a steady contrast value. This behavior suggests a potential indication of linearity in noise suppression but does not conclusively prove it.

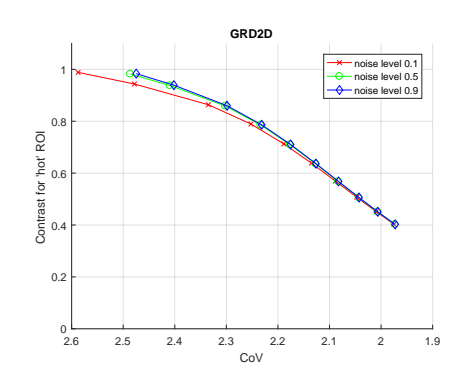
In a linear algorithm, we expect lower counts (and hence more noise) to result in a higher CoV for the same contrast. If CoV remains constant despite increased noise, it likely indicates that the noise contribution to the CoV is smaller than the non-uniformity component of the phantom, which is still acceptable. This trend holds for all algorithms.

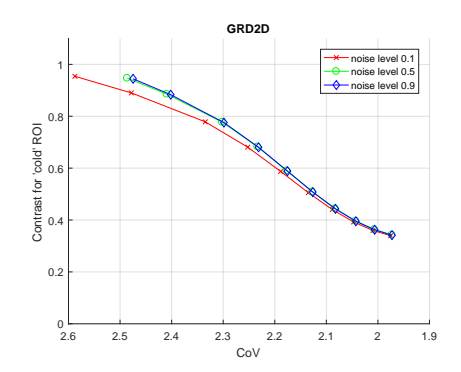






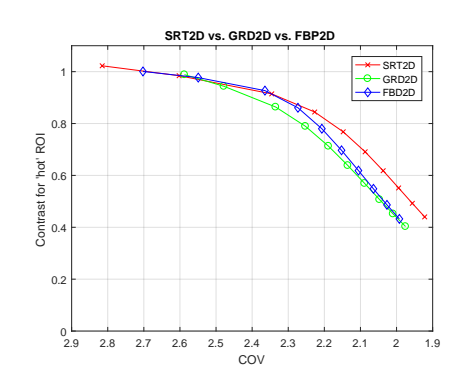


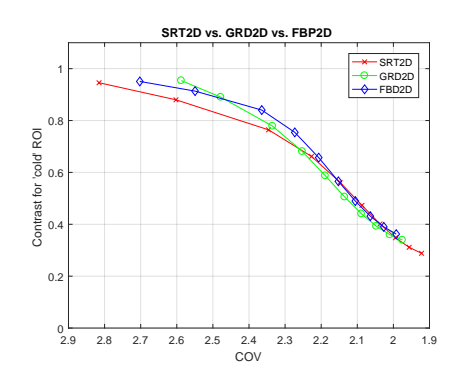




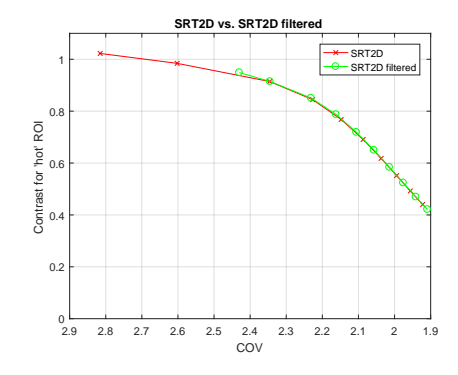
# 5.4.2.3 Contrast vs. CoV: the 10 different postfilters at the highest noise level data are the parameters

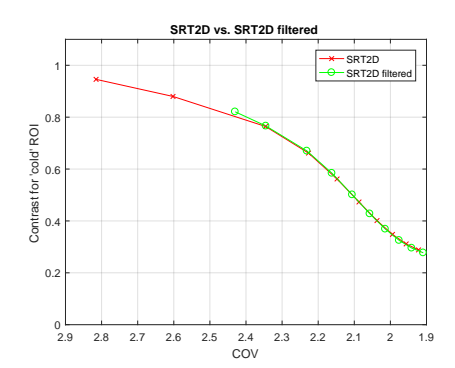
We only present results at the highest noise level, hence at the lowest count level, as the differences between algorithms are more pronounced then.



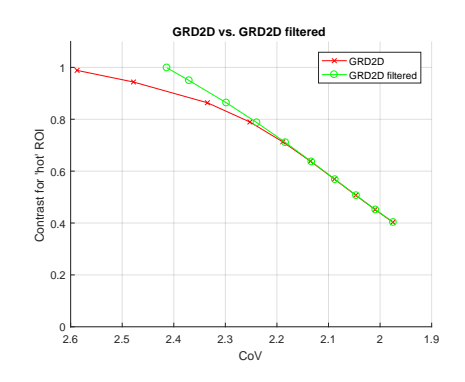


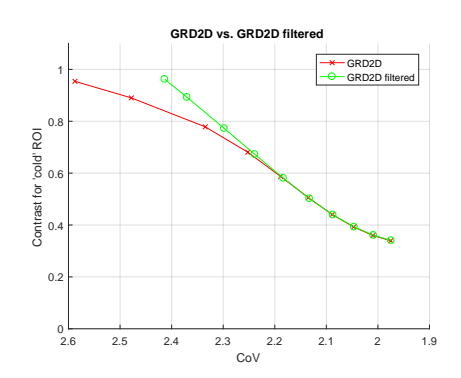
Applying to SRT2D the Wiener automated (i.e. based on the image values and not on parameters' choice) filter,



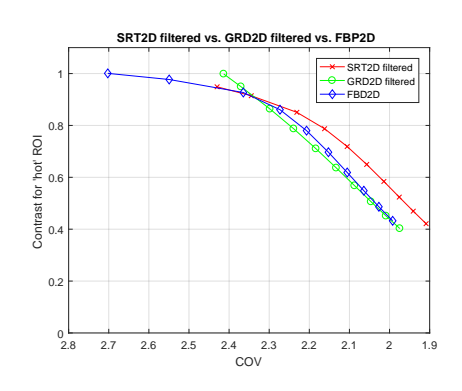


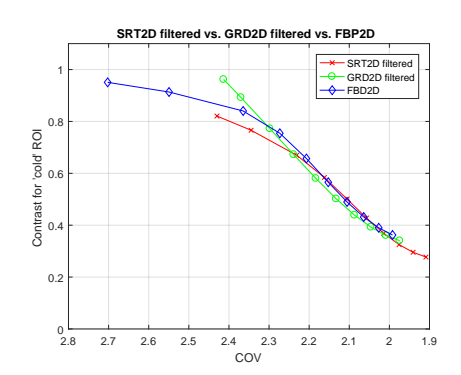
and to GRD2D the filter with parameter 0.5





we get





The algorithms have comparable performance. However, taking into account both contrast and noise, it seems that the best choice for the first sigma of the postfilter is GRD2D filtered, whereas for the 3rd sigma onwards for the 'hot' ROI the best choice is SRT2D with or without filter.

As [71] does not specify the ROI strategy used, it is difficult to compare our results with theirs.

#### **5.4.3** Computational complexity

Let us assume  $sx \sim sy \sim sp \sim sa \sim sth \sim N \in \mathbb{N}$ , where sp is the number of tangential positions, sth is the number of views, sx,sy are the number of points in x,y coordinates, and sa is the number of axial positions, respectively. Then the order of computational complexity of SRT2D is  $O(N^4)$ , whereas of FBP2D is  $O(N^3)$  (the bulk of activity is due to backprojection), and of GRD2D is  $O(N^2 \log_2 N)$  [69].

# Chapter 6

# Implementation of two 2D SPECT analytic reconstruction algorithms in STIR and their performance evaluation

In Software for Tomographic Image Reconstruction (STIR), an object-oriented library implemented in C++ for 3D Positron Emission Tomography (PET) and Single Photon Emission Computed Tomography (SPECT) reconstruction, we implement two analytic 2D SPECT reconstruction algorithms: Kunyansky SPECT Algorithm (KSA2D) and Spline Reconstruction Technique (SRT2DSPECT). As Filtered Backprojection (FBP) does not provide an inverse for the attenuated Radon transform, we focus on these analytic algorithms and compare them with STIR's Ordered Subsets Maximum A Posteriori One Step Late (OSMAPOSL) in terms of image quality, particularly contrast for both 'hot' and 'cold' Regions of Interest (ROIs). Both SRT2DSPECT and KSA2D have better contrast over OSMAPOSL, despite the fact the latter is an iterative algorithm. In particular, KSA2D shows an advantage for 'hot' ROIs, and SRT2DSPECT for 'cold' ROIs. Additionally, KSA2D is notably fast.

# 6.1 Prerequisites

#### **6.1.1** Formulation of the problem

The goal of SPECT is to reconstruct the radionuclide distribution  $f(\mathbf{x})$ ,  $\mathbf{x} \equiv (x_1, x_2)$ , for known attenuation coefficient  $\alpha(\mathbf{x})$ , from measured projections  $g_{\theta}(\rho)$ , where  $\boldsymbol{\theta}(\theta)$  is the direction along which the detector measures the intensity of radiation and  $\rho$  is the distance of this line from the origin. This problem is equivalent to the inversion of the attenuated Radon transform

$$g_{\theta}(\rho) \equiv R_{\alpha,\theta} f = \int_{\mathbb{R}} \exp(-D_{\theta} \alpha [\mathbf{x} + t \boldsymbol{\theta}(\theta)]) f(\mathbf{x} + t \boldsymbol{\theta}(\theta)) dt, \qquad (6.1)$$

where the divergent beam transform  $D_{\theta}\alpha(\mathbf{x})$  is

$$D_{\theta}\alpha(\mathbf{x}) = \int_{0}^{\infty} \alpha(\mathbf{x} + t\mathbf{\theta}(\theta)) dt.$$
 (6.2)

[76]

For convenience a rotated coordinate system  $(\tau, \rho)$  with axes parallel to vectors  $\boldsymbol{\theta}(\theta)$  and  $\boldsymbol{\theta}^{\perp}(\theta)$  can be introduced

$$\tau = x_1 \cos \theta + x_2 \sin \theta = \mathbf{x} \cdot \mathbf{\theta}(\theta),$$

$$\rho = -x_1 \sin \theta + x_2 \cos \theta = \mathbf{x} \cdot \mathbf{\theta}^{\perp}(\theta),$$
(6.3)

and then (6.1) and (6.2) can be written for  $f_{\theta}^{\star}(\tau,\rho) = f(\mathbf{x}(\tau,\rho,\theta)), \ \alpha_{\theta}^{\star}(\tau,\rho) = \alpha(\mathbf{x}(\tau,\rho,\theta))$  and  $D_{\theta}^{\star}\alpha_{\theta}^{\star}(\tau,\rho) = D_{\theta}\alpha(\mathbf{x}(\tau,\rho,\theta))$ . [76]

As stated in [77], the inversion formula was first derived by Novikov [78], extending the derivation of the analogous result for the inverse Radon transform presented in [79]; then in [70] the inversion formula was obtained via a slight modification of a certain formula contained in [79]. In [76] Kunyansky introduced a SPECT reconstruction algorithm based on [78]; we implemented it in STIR as Kunyansky SPECT Algorithm 2D (KSA2D). In [70] the SPECT reconstruction algorithm Spline Reconstruction Technique 2D was introduced; we implemented it

in STIR as SRT2DSPECT.

SRT2DSPECT has two mathematical formulations, in [70] and [77]. For our implementation within STIR, we used [70] because it is of higher image quality. In particular, except for the attenuated Radon transform  $\hat{g}_{\theta}(\rho)$  of the radiopharmaceutical distribution f(x), the mathematical formulation in [70] takes as data the Radon transform  $\hat{\alpha}(\rho,\theta)$ , whereas the mathematical formulation of [77] employs the attenuation coefficient  $\alpha(x)$ ; while the values at the node points used for the spline approximating  $\hat{\alpha}$ , which is used extensively in both algorithms, in [70] are exact, in [77] are themselves approximations, leading inevitably to lower image quality.

#### **6.1.2** SPECT scanner description and assumptions

We assume a cylindrical scanner of radius R. The projections are arc-corrected, meaning the detectors are positioned in a line perpendicular to the scanner, rather than curved around it. Therefore, the distance of the detectors from the origin forms a uniform partition of [-R,R]. This configuration corresponds to SPECT with a parallel hole collimator. We also assume that the angles  $\theta$  are equidistant, forming a uniform partition of  $[0,2\pi]$ .

# **6.2** Kunyansky's SPECT Algorithm (KSA2D)

#### **6.2.1** Mathematical formulation of the reconstruction formula

The content of this subsection is taken from [76]. The real-valued version of the Novikov formula becomes simpler when straightforward differentiation in  $\rho$  replaces the application of the operator  $(-\sin\theta \frac{\partial}{\partial x_1},\cos\theta \frac{\partial}{\partial x_2})$ , equivalently expressed as  $(\boldsymbol{\theta}^{\perp}(\theta)\cdot\nabla)$ , to a function in  $(\tau,\rho)$  coordinates.

Hence, the reconstruction formula is given by

$$f(\mathbf{x}) = \frac{1}{4\pi} \int_0^{2\pi} M_{\theta}(\mathbf{x} \cdot \boldsymbol{\theta}(\theta), \mathbf{x} \cdot \boldsymbol{\theta}^{\perp}(\theta)) d\theta,$$
 (6.4)

$$M_{\theta}(\tau, \rho) = \frac{\partial}{\partial \rho} [\exp(D_{\theta}^{\star} \alpha_{\theta}^{\star}(\tau, \rho)) m_{\theta}(\rho)]. \tag{6.5}$$

where the modified projections  $m_{\theta}(\rho)$  are

$$m_{\theta}(\rho) = e^{-A_{\theta}(\rho)} \left[ h_{\theta}^{c}(\rho) H \left( h_{\theta}^{c}(\rho) e^{A_{\theta}(\rho)} g_{\theta}(\rho) \right) + h_{\theta}^{s}(\rho) H \left( h_{\theta}^{s}(\rho) e^{A_{\theta}(\rho)} g_{\theta}(\rho) \right) \right], \tag{6.6}$$

with

$$h_{\theta}^{c}(\rho) = \cos(HA_{\theta}(\rho)),$$
 (6.7)

$$h_{\theta}^{s}(\rho) = \sin(HA_{\theta}(\rho)),$$
 (6.8)

$$A_{\theta}(\rho) = \frac{1}{2} (R_{\theta} \alpha)(\rho), \tag{6.9}$$

and the Hilbert transform H of a function h(u)

$$Hh(u) = \frac{1}{\pi} \mathcal{P} \int_{\mathbb{R}} \frac{h(u)}{u - v} \, \mathrm{d}v. \tag{6.10}$$

#### 6.2.2 The algorithm steps and a few implementation comments

For a very detailed description of the algorithm implementation we refer the reader to Section 4 of [76]. Hence, we include only the algorithm steps with a few comments of ours.

We assume radially and angularly uniformly discretized  $g_{\theta_i}(p_j)$ ,  $i = 1, 2, ..., n_{\phi}$ ,  $j = 1, 2, ..., n_p$ , where  $n_{\phi}$  is the number of projections,  $n_p$  is the discretization size of each projection.

Step 1 Evaluate the divergent beam transform  $D_{\theta}\alpha(x)$  (DBT) given by (6.2), using bilinear interpolation and trapezoidal quadrature.

Simply using bilinear interpolation and trapezoidal quadrature for the calculation of the DBT, and ultimately the Radon transform, is nowhere near as accurate as the Siddon's algorithm [80] used for the forward project in STIR's pinhole SPECT scanners, but it needs only  $\mathcal{O}(n_p^2)$  operations, making it extremely fast.

Note that we assume that the attenuation coefficient is given on the same Cartesian grid on which the image will be reconstructed (therefore scaling is not an option for attenuation). (Hence, the settings for the number of pixels and pixel-size are disabled). An appropriate interpolation can be used in case attenuation is given on a different grid.

Step 2 Evaluate the Radon transform  $A_{\theta_i}(\rho_j)$  given by (6.9) and (6.1) (which is simply  $\frac{1}{2}D_{\theta_i}^{\star}\alpha_{\theta_i}^{\star}(\tau_1,\rho_j), i=1,2,\ldots,n_{\phi}, i=1,2,\ldots,n_p$ ).

**Step 3** Evaluate  $HA_{\theta}(\rho)$ , the Hilbert transform of  $A_{\theta}(\rho)$ .

In [76] the Hilbert transform is regarded as a convolution with kernel  $1/(\pi p)$ , and it is calculated as discrete convolution with the kernel represented by the sequence  $K_j$ ,  $j=-n_p,\ldots,n_p$ . This kernel has  $2n_p+1$  elements, so to perform such a convolution one should pad the function to  $2n_p+1$  samples and then follow the standard procedure (i.e.  $f*K=\hat{f}\hat{K}$  where  $\hat{f}$  can be calculated using FFT).

The method of calculation of Hilbert transform we preferred is the one mentioned in [81], as it gives better results for the points close to the interval edges, as shown in Figure 6.1.  $2n_p + 1$  is not an FFT-friendly number (thus making the algorithm slow), so we pad the kernel function to actually  $2n_p$  samples (since it has a finite support, and therefore it is zero at the boundary), and we set  $\hat{K}_1 = \hat{K}_{n_p+1} = 1$ ,  $\hat{K}_{2,\dots,n_p} = 2$  and  $\hat{K}_{n_p+2,\dots,2n_p} = 0$ .

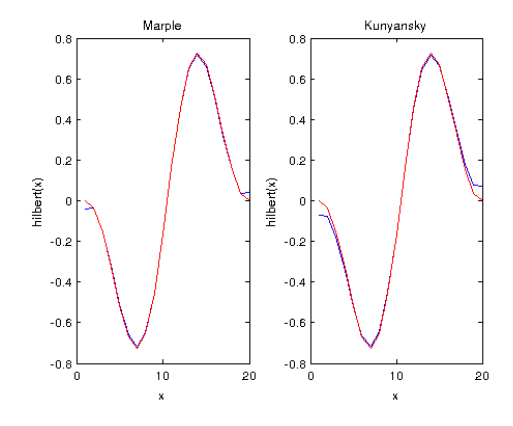


**Figure 6.1:** Hilbert transform of sinc(x): precise value vs. numerical value with Marple's method (which we use) vs. Kunyansky's method

As STIR's FBP2D has a Ramp-Hamming filter, i.e. an enhanced variant

beyond the Ramp filter (the latter being an integral component of the mathematical formulation of FBP), we also added to KSA2D the filter proposed in [76]:

$$\hat{W}[\rho] = \left\{ \begin{array}{ll} 1/2(1 + \cos(\pi \rho/\rho^{\text{cutoff}})), & |\rho| \le \rho^{\text{cutoff}} \\ 0, & |\rho| > \rho^{\text{cutoff}} \end{array} \right., \quad \rho^{\text{cutoff}} \le \rho^{\text{Nyquist}}, \quad (6.11)$$

where  $ho^{ ext{cutoff}}$  is the cut-off frequency.

#### **Step 4** Compute modifying projections $m_{\theta}(\rho)$ by

- i. calculating  $h_{\theta}^{c}(\rho)$  and  $h_{\theta}^{s}(\rho)$  using (6.7) and (6.8), respectively,
- ii. calculating the Hilbert transforms  $H(h^c_{\theta}(\rho)e^{A_{\theta}(\rho)}g_{\theta}(\rho))$  and  $H(h^s_{\theta}(\rho)e^{A_{\theta}(\rho)}g_{\theta}(\rho))$  and
- iii. calculate  $m_{\theta}(\rho)$  using (6.6).
- **Step 5** Differentiate the product  $\exp(D_{\theta}^{\star}\alpha_{\theta}^{\star}(\tau,\rho))m_{\theta}(\rho)$  in  $\rho$ , hence calculating (6.5), using a central difference scheme.

For the differentiation of the product  $\exp(D_{\theta}^{\star}\alpha_{\theta}^{\star}(\tau,\rho))m_{\theta}(\rho)$  is employed a fourth order central difference

$$u'(\rho) \approx \frac{1}{12\Delta\rho} \left[ \left( -u(\rho + 2\Delta\rho) + u(\rho - 2\Delta\rho) \right) + 8\left( u(\rho + \Delta\rho) - u(\rho - \Delta\rho) \right) \right].$$

We have also extended the method to the left boundary by using the 4th order forward difference

$$u'(\rho) \approx \frac{1}{\Delta \rho} \left[ -\frac{25}{12} u(\rho) + 4u(\rho + \Delta \rho) - 3u(\rho + 2\Delta \rho) + \frac{4}{3} u(\rho + 3\Delta \rho) - \frac{1}{4} u(\rho + 4\Delta \rho) \right],$$

and for the right boundary the 4th order backward difference

$$u'(\rho) \approx \frac{1}{\Delta \rho} \left[ \frac{25}{12} u(\rho) - 4u(\rho + \Delta \rho) + 3u(\rho + 2\Delta \rho) - \frac{4}{3} u(\rho + 3\Delta \rho) + \frac{1}{4} u(\rho + 4\Delta \rho) \right].$$

**Step 6** Backproject the result of the differentiation  $M_{\theta}(\tau, \rho)$  to obtain (6.4), again

using bilinear interpolation and a simple quadrature rule.

#### **6.2.3** Notes on STIR implementation

The following points pertain to implementation particularly in STIR.

There is a subtle point regarding reconstruction for all slices in SPECT in STIR. Note that in SPECT only direct sinograms are defined, therefore in STIR's notation we are iterating over all axial positions of segment 0. As in the case of FBP2D, for data created by STIR's simulated parallel hole SPECT scanners, user is forced to set z output size in the parameter file, to the number of rings (so that the final image z positions will be compatible). Otherwise, the default  $z\_output\_size$  in STIR is  $2*number\_of\_slices-1$ , i.e.  $(number\_of\_slices-1)$  extra elements are added, in particular the oblique projections between neighbour rings, which are not defined in SPECT.

FFT function in STIR for complex data works only for number of data that are power of 2 (the remaining FFT functions work for even number of data). Therefore padding is required for the Fourier transform used in the calculation of the three Hilbert transforms.

Grid spacing of attenuation map must be the same with grid spacing for the reconstructed image. If we change xy output, grid does not essentially change, but grid changes once zoom is changed. In the latter case interpolation of attenuation in the new grid would be required, therefore the mathematical formulae should change in case zoom would be included.

# 6.3 Spline Reconstruction Technique (SRT2DSPECT)

# **6.3.1** Mathematical formulation and algorithm steps of SRT2DSPECT

The content of this subsection is taken from [70], which introduces the mathematical formulation of SRT2DSPECT we implement in STIR.

Taking the real part of attenuated Radon transform yields

$$f(x_1, x_2) = \frac{1}{4\pi} \int_0^{2\pi} (r_{x_1} \sin \theta - r_{x_2} \cos \theta) d\theta, \tag{6.12}$$

where  $\tau$  and  $\rho$  are given by (6.3), and

$$r(\tau, \rho, \theta) = I(\tau, \rho, \theta) \left( \alpha^{cme} \left( \frac{1}{\pi} h^c + 2\alpha^s \right) + \alpha^{sme} \left( \frac{1}{\pi} h^s - 2\alpha^c \right) \right), \quad (6.13)$$

with

$$I(\tau, \rho, \theta) = \exp\left(\int_{\tau}^{\sqrt{1-\rho^2}} A(\tau', \rho, \theta) d\tau'\right), \tag{6.14}$$

$$A(\tau, \rho, \theta) = -\frac{1}{4\pi^2} \int_0^{2\pi} h_{\rho}(\tau \sin(\theta - t) + \rho \cos(\theta - t), t) dt,$$
 (6.15)

$$h_{\rho}(\rho,\theta) = \frac{\partial}{\partial \rho} \sum_{i=1}^{n-1} \int_{\rho_i}^{\rho_{i+1}} \frac{S_i(\rho',\theta)}{\rho' - \rho} d\rho', \tag{6.16}$$

and

$$\alpha^{cpe}(\rho,\theta) = e^{\frac{1}{2}\hat{\alpha}(\rho,\theta)}\cos\frac{h(\rho,\theta)}{2\pi}, \quad \alpha^{spe}(\rho,\theta) = e^{\frac{1}{2}\hat{\alpha}(\rho,\theta)}\sin\frac{h(\rho,\theta)}{2\pi}(6.17)$$

$$\alpha^{cme}(\rho,\theta) = e^{-\frac{1}{2}\hat{\alpha}(\rho,\theta)}\cos\frac{h(\rho,\theta)}{2\pi}, \quad \alpha^{sme}(\rho,\theta) = e^{-\frac{1}{2}\hat{\alpha}(\rho,\theta)}\sin\frac{h(\rho,\theta)}{2\pi}(6.18)$$

$$\alpha^{c}(\rho,\theta) = \alpha^{cpe}(\rho,\theta)\hat{g}_{\theta}(\rho), \quad \alpha^{s}(\rho,\theta) = \alpha^{spe}(\rho,\theta)\hat{g}_{\theta}(\rho), \quad (6.19)$$

$$h^{c}(\rho,\theta) = \int_{-\infty}^{\infty} \frac{\alpha^{c}(\rho',\theta)}{\rho'-\rho}d\rho', \quad h^{s}(\rho,\theta) = \int_{-\infty}^{\infty} \frac{\alpha^{s}(\rho',\theta)}{\rho'-\rho}d\rho'. \quad (6.20)$$

$$(6.21)$$

Suppose that  $\hat{\alpha}(\rho, \theta)$  is given, for every  $\theta$ , at n equally spaced points  $\rho_i \in [-1, 1]$ , i.e. suppose that  $\hat{\alpha}_i = \hat{\alpha}(\rho_i, \theta)$  are known. Similarly for  $\hat{g}_{\theta}(\rho)$ . Then to calculate numerically  $f(x_1, x_2)$  we perform the following steps.

113

**I.1** Calculation of  $h(\rho, \theta)$  at all given  $\rho$  and  $\theta$  using

$$h(\rho,\theta) = -\hat{\alpha}_{i} + \hat{\alpha}_{i+1} + \frac{1}{36} \left( -4\rho_{i}^{2} - 5\rho_{i}\rho_{i+1} - 5\rho_{i+1}^{2} - 3(\rho_{i} - 5\rho_{i+1})\rho - 6\rho^{2} \right) \hat{\alpha}_{i}^{"} + \frac{1}{36} \left( 5\rho_{i}^{2} + 5\rho_{i}\rho_{i+1} - 4\rho_{i+1}^{2} - 3(5\rho_{i} - \rho_{i+1})\rho + 6\rho^{2} \right) \hat{\alpha}_{i+1}^{"}, \qquad (6.22)$$

where the second derivatives  $\hat{\alpha}_i''$  of  $\hat{\alpha}(x,y)$  with respect to  $\rho$  at  $\rho = \rho_i$  are calculated by subroutine spline from Numerical Recipes [61].

1.2 Use of Step I.1 for the calculation of  $\alpha^{cpe}(\rho, \theta)$  and  $\alpha^{spe}(\rho, \theta)$  by use of (6.17), and then of  $\alpha^{c}(\rho, \theta)$  and  $\alpha^{s}(\rho, \theta)$  by use of (6.19) and the data function  $\hat{g}_f$ .

Calculation of the second derivatives of  $\alpha^c(\rho, \theta)$  and  $\alpha^s(\rho, \theta)$  by use of subroutine spline.

*Step II* Calculations on segments  $[\rho_i, \rho_{i+1}]$ .

- **II.1** Calculate numerically  $\alpha(x_1, x_2)$  (same procedure as in PET)
  - $\theta$ ). In each interval  $[\rho_i, \rho_{i+1}]$  we approximate  $\hat{\alpha}(\rho, \theta)$  calculating the natural cubic spline  $S_i(\rho, \theta)$  (in  $\rho$ ) by subroutine splint from Numerical Recipes [61], which uses the second derivatives  $\hat{\alpha}_i''$  of  $\hat{\alpha}(x,y)$  with respect to  $\rho$  at  $\rho=\rho_i$ , which had themselves been calculated at Step I.1.

i. Calculation of the natural cubic spline of  $\hat{\alpha}(\rho, \theta)$  for any  $x_1, x_2$  (and

**ii.** Calculation of  $h_{\rho}(\rho, \theta)$ .

For  $\rho \neq \rho_i, \rho_{i+1}$  holds

$$h_{\rho}(\rho,\theta) = \frac{\partial}{\partial \rho} \sum_{i=1}^{n-1} \int_{\rho_{i}}^{\rho_{i+1}} \frac{S_{i}(\rho',\theta)}{\rho' - \rho} d\rho'$$

$$= \sum_{i=1}^{n-1} \left( \frac{\hat{\alpha}_{i}}{\rho_{i} - \rho} - \frac{\hat{\alpha}_{i+1}}{\rho_{i+1} - \rho} \right)$$

$$-\frac{1}{4} (\rho_{i} - 3\rho_{i+1} + 2\rho) \hat{\alpha}_{i}^{"} - \frac{1}{4} (3\rho_{i} - \rho_{i+1} - 2\rho) \hat{\alpha}_{i+1}^{"}$$

$$+ \left[ \frac{\hat{\alpha}_{i} - \hat{\alpha}_{i+1}}{\rho_{i} - \rho_{i+1}} - \frac{1}{6} (\rho_{i} - \rho_{i+1} - \frac{3(\rho_{i+1} - \rho)^{2}}{\rho_{i} - \rho_{i+1}}) \hat{\alpha}_{i}^{"} \right]$$

$$+ \frac{1}{6} (\rho_{i} - \rho_{i+1} - \frac{3(\rho_{i} - \rho)^{2}}{\rho_{i} - \rho_{i+1}}) \hat{\alpha}_{i+1}^{"} \ln \left| \frac{\rho_{i+1} - \rho}{\rho_{i} - \rho} \right|,$$
(6.23)

where  $\rho$  is calculated for any  $x_1$  and  $x_2$  (for any  $\theta$ ) using (6.3).

iii. Numerical integration of (6.23).

We calculate

$$\int_{0}^{2\pi} h_{\rho}(\theta) d\theta = \frac{2\pi}{N} \sum_{i=0}^{N-1} h_{\rho}\left(\frac{2\pi i}{N}\right), \tag{6.24}$$

and multiplying by  $-\frac{1}{4\pi^2}$  we get  $f(x_1, x_2)$ .

*II.2* We calculate  $h(\rho, \theta)$  for  $\rho \neq \rho_i$  and  $\rho \neq \rho_{i+1}$ 

$$h(\rho,\theta) = \sum_{i=1}^{n-1} \left\{ F_i - \frac{1}{\rho_i - \rho_{i+1}} \ln \left| \frac{\rho_{i+1} - \rho}{\rho_i - \rho} \right| \left[ (\rho_{i+1} - \rho) \hat{\alpha}_i - (\rho_i - \rho) \hat{\alpha}_{i+1} - \frac{1}{6} (\rho_i - \rho) (\rho_{i+1} - \rho) \left( (\rho_i - 2\rho_{i+1} + \rho) \hat{\alpha}_i'' + (2\rho_i - \rho_{i+1} - \rho) \hat{\alpha}_{i+1}'' \right) \right] \right\},$$
(6.25)

where  $F_i$  is the right–hand side of (6.22).

II.3 We calculate  $\alpha^{cme}(\rho,\theta)$  and  $\alpha^{sme}(\rho,\theta)$  by (6.18) using Steps II.1 and II.2,  $\alpha^{c}(\rho,\theta)$  and  $\alpha^{s}(\rho,\theta)$  by (6.19) using splint with the derivatives calculated at Step I.1 and the corresponding node values at Step I.2, and  $h^{c}(\rho,\theta)$  and  $h^{s}(\rho,\theta)$  using relations similar to (6.25).

**II.4** We numerically calculate  $I(\tau, \rho, \theta)$  assuming compact support, hence on finite integration domain. If  $\tau < 0$ , in place of (6.14) we use

$$I(\tau, \rho, \theta) = \exp\left(\hat{\alpha}(\rho, \theta) - \int_{-\sqrt{1-\rho^2}}^{-\tau} A(\tau', \rho, \theta) d\tau'\right). \quad (3.16)$$
(6.26)

We use the Gauss-Legendre quadrature

$$\int_{\alpha}^{\beta} A(\tau', \rho, \theta) d\tau' \approx w_1 A(\tau_1, \rho, \theta) + w_2 A(\tau_2, \rho, \theta), \tag{6.27}$$

where the abscissas  $\tau_1, \tau_2$  and the weights  $w_1, w_2$  are given by

$$\tau_1 = a + (b - a) \left( \frac{1}{2} - \frac{\sqrt{3}}{6} \right), \quad \tau_2 = a + (b - a) \left( \frac{1}{2} + \frac{\sqrt{3}}{6} \right), \quad w_1 = w_2 = \frac{1}{2} (b - a).$$
(6.28)

- **II.5** Using Steps II.3 and II.4 we calculate  $r(\tau, \rho, \theta)$  by (6.13).
- **II.6** Finally we calculate  $f(x_1, x_2)$  using (6.12) by numerical integration similar to the one in Step II.1.iii, and numerical calculation of the partial derivatives  $r_{x_1}$  and  $r_{x_2}$  by a forward difference scheme and a backward difference scheme for the first half and second half of the interval [-1,1], respectively, i.e.

$$\alpha'(\mathbf{x}) \approx \frac{-3\alpha(\mathbf{x}) + 4\alpha(\mathbf{x} + \Delta\mathbf{x}) - \alpha(\mathbf{x} + 2\Delta\mathbf{x})}{2\Delta\mathbf{x}}$$
 (6.29)

$$\alpha'(\mathbf{x}) \approx \frac{-3\alpha(\mathbf{x}) + 4\alpha(\mathbf{x} + \Delta\mathbf{x}) - \alpha(\mathbf{x} + 2\Delta\mathbf{x})}{2\Delta\mathbf{x}}$$

$$\alpha'(\mathbf{x}) \approx \frac{3\alpha(\mathbf{x}) - 4\alpha(\mathbf{x} - \Delta\mathbf{x}) + \alpha(\mathbf{x} - 2\Delta\mathbf{x})}{2\Delta\mathbf{x}}$$
(6.29)

#### Speeding up techniques, filtering, and further aspects of 6.3.2 the STIR implementation

We describe some aspects of the STIR implementation of SRT2DSPECT; predominantly, the ones leading to speed and image quality improvement.

#### 6.3.2.1 SPECT symmetry

For the Hilbert transform, we could apply the same symmetries used for the derivative of the Hilbert transform in 2D SRT PET (SRT2D algorithm in STIR), as discussed in Chapter 4 of the thesis, since both include the same logarithmic expression.

A new symmetry has been employed for the calculation of the derivative of the Hilbert transform for partition th2.

Let  $x, y, \rho \in [-1, 1]$  and  $\theta \in [0, 2\pi)$ , and let  $\{x_i\}_{i=1}^{sx}, \{y_i\}_{i=1}^{sy}$  be uniform partitions of [-1, 1] with sx = sy points,  $\{\rho_i\}_{i=1}^{sp}$  uniform partition of [-1, 1] with sp points, and  $\{\theta_i\}_{i=0}^{sth}$  uniform partition of  $[0, 2\pi - \frac{2\pi}{sth}]$  with sth points. Let  $Nt \in \mathbb{N}$ , such that Nt even and Nt << sth (i.e. Nt = 8 or Nt = 10) and let  $\{t_i\}_{i=1}^{Nt}$  be a uniform partition of  $[0, 2\pi - \frac{2\pi}{Nt}]$  with Nt points.

Let  $\rho(\omega; a, b, c) := a\cos(c - \omega) + b\sin(c - \omega)$  and if  $a, b \in [-1, 1], c \in [0, 2\pi]$ , we observe that  $\rho(\omega) = -\rho(\pi + \omega)$ . Therefore, for the partitions mentioned above we get  $\rho(t_i; a, b, \theta_i) = -\rho(t_{Nt/2+i}, a, b, \theta_i)$  for  $j = 1 \dots Nt/2$  (See Figure 6.2 below).

Therefore  $\ln |\rho - \rho(t_j; a, b, \theta_i)| = \ln |\rho + \rho(t_{Nt/2+j}; a, b, \theta_i)|$ . And so, we have that  $\ln |\rho_k - \rho(t_j; a, b, \theta_i)| = \ln |\rho_{sp-k+1} - \rho(t_{Nt/2+j}; a, b, \theta_i)|$ . This is a direct consequence of equation  $\rho_i - \rho = -(\rho_{sp-i+1} - (-\rho)) = -(\rho_{sp-i+1} + \rho)$ .

SPECT requires the calculation of  $\ln(|\rho_k - \rho(t_j; a, b, \theta_i)|)$  for all  $k = 1 \dots sp$ ,  $j = 1 \dots Nt$ . We can reduce evaluations of log by calculating the logarithm for  $k = 1 \dots sp$  and  $j = 1 \dots Nt/2$ .

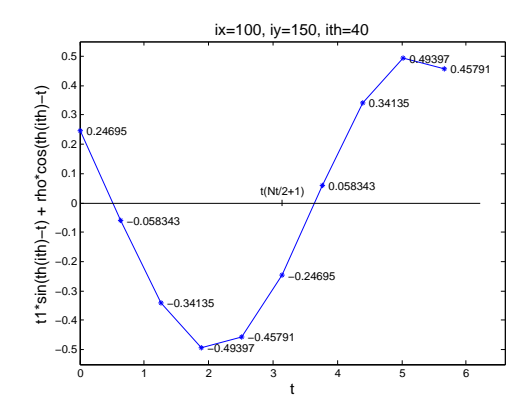


**Figure 6.2:** Examples of symmetry of  $t_1 \sin(th(ith) - t) + rho\cos(th(ith) - t)$  with respect to the values t of th2 for  $x_1(100), x_2(150), \theta(40)$ .

#### 6.3.2.2 Input data read as viewgrams instead of as sinograms

To read input data as viewgrams instead of sinograms, the same logic applies as in 2D PET [82]. In the case of 2D SPECT, though, it leads to further improvement of speed (45%) compared to 2D PET(35%), as there are more quantities we can calculate in the third loop, and use the computed values in ALL iterations of the fourth loop. In particular, besides  $log|p_i-x|$ , where p is the partition for tangential positions, we can calculate the spline coefficients, and more importantly the logarithms for the function for calculating the derivative of Hilbert transform, which is calculated for each axial position for the coarser (second) partition of  $\theta$ (views) in a fifth(!) loop nested inside the fourth loop. It is noteworthy that the final loops run along axial position, x1, x2 (instead of  $x1, x2, \theta$ ) and the values are added to the final image (instead of being integrated and assigned to the final image, as in the case of sinogram).

#### 6.3.2.3 Further speeding up techniques

We need to calculate 3 Hilbert transforms with the same  $\rho$ . So, we have calculated the logarithm value once for each  $\rho_i$  and use this value for all these Hilbert transforms. (Let us note that since each symmetry evaluates Hilbert transform for the same  $\rho$  as the original point, we could cache the logarithmic value of  $\rho - \rho_i$  and use it for the extra 3 Hilbert transforms of the symmetric point. Therefore, having 8 symmetric point, should we have used the symmetries for the Hilbert transform, we would have used the same logarithmic value for a total of 8\*3=24 Hilbert transforms.)

#### 6.3.2.4 Parallelization

In case of SPECT with input read in sinogram format, due to the size of the matrices that were used, there was a problem on the initialization of these matrices for the threads. Therefore, we had to initialize calloc inside our parallel loops, which slows down the algorithm. In case of SPECT with input read in viewgram format the matrices were not that large; in particular matrix dimension for viewgram is  $sa \times sx \times sy$ , whereas for sinogram  $sa \times sy \times sth$ , and number of axial positions sa is significantly less than number of views sth.

#### 6.3.2.5 Reading attenuation data from file

We set the attenuation filename as an optional input and check its validity before reading the attenuation data in the same way as the emission data, using STIR's reconstruction functions.

#### 6.3.2.6 Filtering

For the same reason we added a filter to KSA2D (see Step 2 in Section 6.2.2), after experimentation with various filter choices and combinations, we created a mixture of automated filters for SRT2D, in particular, a Wiener, a gamma and a median filter (the latter used with caution as it can potentially suppress details). As default filters we have set the Wiener and the gamma filter; however, the reader is given the option to disable or enable each one of the available filters from the parameter file.

Wiener filter. It computes a local mean and variance for the whole slice. It then shifts the value of each pixel in the slice by the estimated noise level, averaging the computed local variance over the slice. To minimize the impact of noise on pixel intensity, the filter adjusts pixels based on noise and variance levels: pixels with high variance are lightly corrected to maintain detail while reducing noise, whereas pixels with variance similar to or lower than noise undergo stronger smoothing to suppress noise, balancing detail preservation and noise reduction.

Gamma filter. It adjusts the luminance of an image to either amplify or attenuate its contrast without altering the inherent spatial characteristics. Initially, it normalizes pixel values to a [0, 1] range, facilitating consistent application across varying image intensities. It then calculates the average pixel value of the image, disregarding pixels with absolute values less than a threshold (0.1) to focus on more significant data points. Based on this average, a gamma correction value is determined, aiming to adjust the average pixel intensity towards a predefined target (0.25). The correction is applied by raising each pixel's value to the power of the gamma value, effectively modifying the distribution of pixel intensities to enhance or reduce contrast. Pixels with negligible intensity are excluded from this power operation to maintain numerical stability. Finally, the image is denormalized, scaling the pixel values back to their original range.

*Median filter.* It processes an image one pixel at a time. It considers a local neighborhood around each pixel. For each pixel, a small window of neighboring pixels (in this case, a  $3 \times 3$  grid centered around the pixel in question) is taken; the values of those pixels are then collected and sorted. Then, the replaced pixel value is computed as the median of this ordered list of neighboring pixel values, which replaces the original pixel values. Since it is to be applied to EACH pixel, apart from the border pixels, the threshold is set effectively half-way through the sorted list, so by definition half the values are either lower or higher.

# 6.4 Comparison of algorithms

#### 6.4.1 Phantom and creation of data

We will perform comparisons with XCAT phantom of  $128 \times 128 \times 128$  voxels (see Fig. 6.3).

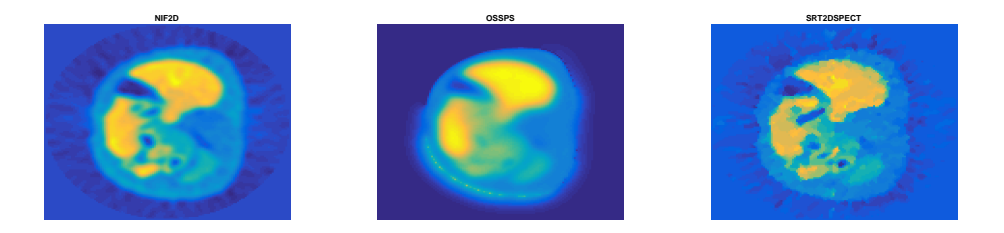


Figure 6.3: XCAT cardiac phantom

Scanner interfiles and sinograms (with the addition of Poisson noise) were created in STIR; the latter together with the parameter files and the reconstructed images via a bash script allowing automation of the procedure. The implementation should work for every scanner (having set the extend of rotation to 360), assuming an appropriate attenuation map is given; in particular, attenuation image must be  $sp \times sp$ , where sp is the number of tangential positions of the scanner. (Let us note that for the DFT's, the size of sp does not matter, as it is always doubled and padded to the smallest power of 2.)

Attenuation correction has to be off for FBP. Therefore we are not going to perform comparisons with STIR's FBP2D.

We compare KSA2D, SRT2DSPECT, and STIR's OSMAPOSL.



**Figure 6.4:** Reconstructed images of KSA2D, OSSPS, and SRT2DSPECT with a 0.01 Poisson noise scaling factor.

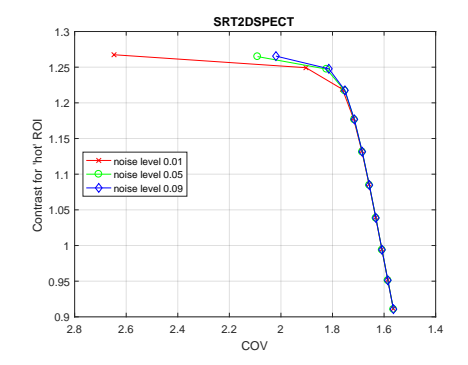
#### **6.4.2** Image Quality Metrics

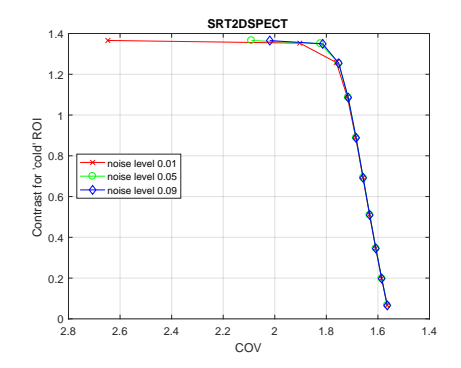
To adjust the NEMA standard test for the XCAT phantom, we regard the 'hot sphere' as the ROI with a value of 2800, the 'cold sphere' as the ROI with a value of 0, and the 'background' as the ROI with a value of 700.

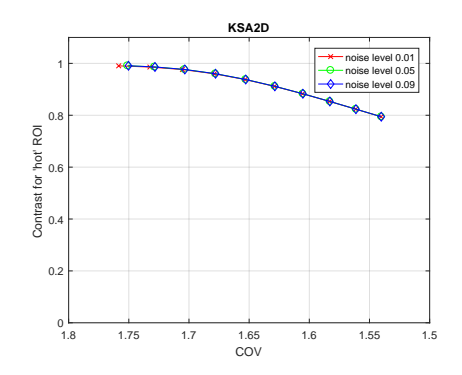
For details regarding how ROIs are chosen, the contrast metrics, and noise sensitivity comments, refer to Section 5.4.2, which describes the methodology applied for 2D PET; the same approach is followed here, adjusted for the specific characteristics of the XCAT phantom used in 2D SPECT.

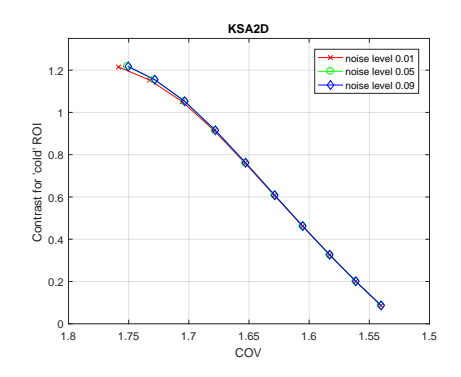
For STIR, to generate different levels of Poisson noise, the forward-projected sinograms were scaled with factors of 0.01, 0.05, and 0.09 before calling a Poisson random number generator.

## 6.4.2.1 Noise Sensitivity and Algorithm Behavior



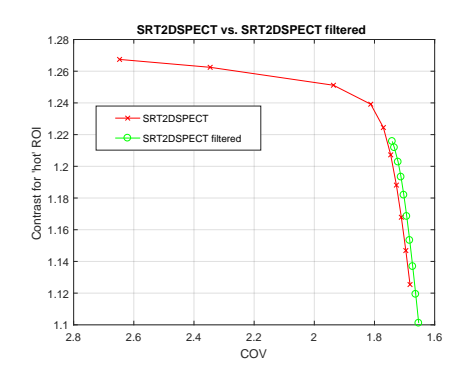


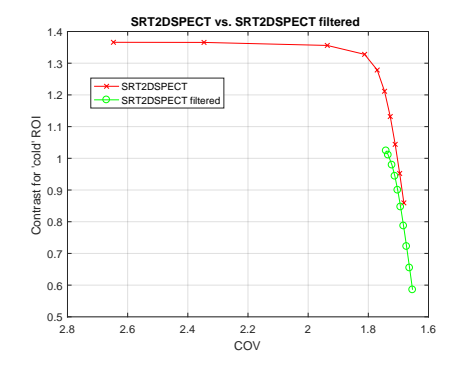




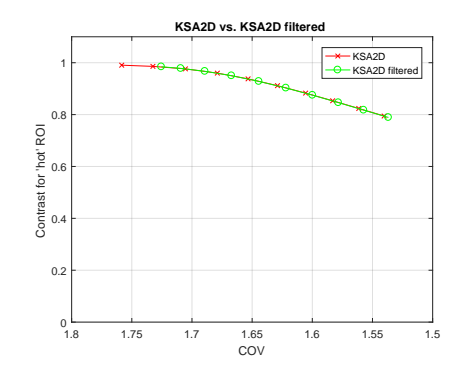
# 6.4.2.2 Contrast vs. CoV: the 10 different postfilters at the highest noise level data are the parameters

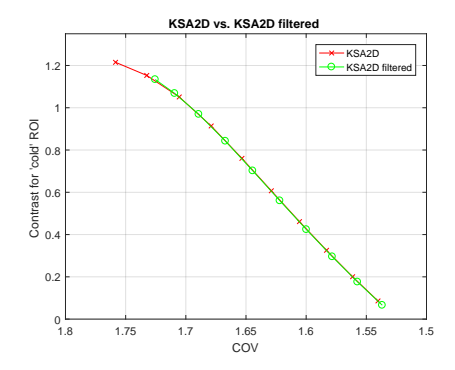
Due to SRT2DSPECT's inherent noise, it is necessary that it is filtered.



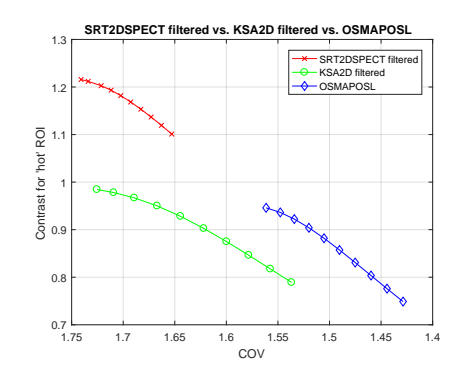


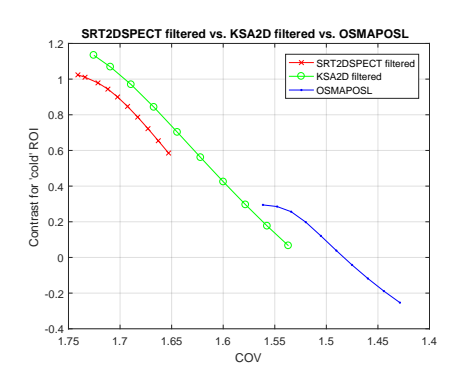
Applying to KSA2D its filter with parameter 0.5,





we get





For the hot region, the KSA2D algorithm gives the best results. SRT2DSPECT highly overestimates the contrast while exhibiting the same noise levels as KSA2D. OSMPOPOSL provides slightly lower contrast than KSA2D, but with significantly less noise. For the cold region, we observe that SRT2DSPECT produces the best contrast, although with slightly higher noise compared to KSA2D. KSA2D yields higher-than-expected contrast for the initial sigmas, resulting in an illusionary contrast (as all values above 1 for the 'cold' ROIs formula). OSMAPOSL, on the other hand, provides very low contrast, rendering its reduced noise irrelevant.

As [77] uses the uniform NEMA phantom, while we use an anatomically realistic phantom, it would be difficult to compare our results with theirs.

#### **6.4.3** Computational Complexity

OSMAPOSL being an iterative algorithm won't be compared with the analytic algorithms for speed. Let us assume  $sx \sim sy \sim sp \sim sth \sim N \in \mathbb{N}$ , where sp is the number of tangential positions, sth is the number of views, and sx,sy are the number of points in x,y coordinates, respectively. Then KSA2D is of order of computational complexity  $O(N^3)$  [76], and SRT2DSPECT is  $O(N^4)$ .

# **Chapter 7**

# Implementation of a 3D PET analytic reconstruction algorithm in STIR and its performance evaluation

In Software for Tomographic Image Reconstruction (STIR), an object-oriented library implemented in C++ for 3D Positron Emission Tomography (PET) and Single Photon Emission Computed Tomography (SPECT) reconstruction, we implement a 3D Direct Fourier Method (DFM3D). We compare it in terms of speed and image quality, in particular contrast for both 'hot' and 'cold' Regions of Interest (ROIs), with the prevailing analytic reconstruction algorithm Filtered Backprojection 3D Reprojection (FBP3DRP) included in STIR. Both algorithm have the same order of computational complexity, but FBP3DRP has better image quality.

# 7.1 Prerequisites

## **7.1.1 3D Geometry**

#### 7.1.1.1 Physical scanner (discrete data)

A PET scanner consists of gamma-ray detectors arranged in the circumference of a circle. The scanner measures emissions along lines connecting pairs of detectors. We call such a line LOR (Line of Response). We symbolize the angle of an LOR with the x axis with  $\theta$ . Typically we have the same number of LORs for each angle  $\theta$ .

We symbolize them with  $n_{\rm rad}$  (or sp) and call them *number of tangential positions*. We symbolize the number of angles  $\theta$  with  $n_{\rm ang}$  (or sth) and call them *number of views*. Theoretically a scanner with N number of detectors can have N/2 number of tangential positions and N/2 number of views (since the LOR connecting the pair (i, j) of detectors with the pair (j, i) is the same), but this can vary vastly.

In the three dimensional (3D) case the physical arrangement of the detectors is exactly the same as in the two dimensional (2D), but now measurements across different rings are allowed. This improves the quality of the image, as we are able to capture more photons, but complicates the reconstruction process. To characterize the projection data (Line of Responses or LORs) in the 3D case, we introduce two additional quantities related to the axial direction of the scanner, namely segments and axial positions. We say that an LOR belongs to the *segment s* if the ring difference of the detectors is s. Therefore a scanner with r rings can have 2r - 1 number of segments ranging from -r + 1 to r - 1. The other necessary quantity to uniquely characterize an LOR is the *axial position*, we say that an LOR has axial position a if the average ring of the detectors is a. Therefore segment s can have r - |s| number of axial positions. Note that axial positions are not integers but multiples of 0.5, this does not pose any problem since we are never going to use this notation in practice.

#### 7.1.1.2 Rotated coordinate system (mathematical formulation)

Standard coordinate system is oriented in the scanner so that the *z*-axis is the axis of rotation of the cylindrical detector system, and the origin is at the center of the scanner. As in the 2D case, we will introduce a rotated coordinate system  $(\rho, \alpha, \tau)_{(\theta, \phi)}$  in order to align the LORs with the  $\tau$ -axis.  $(\rho, \alpha, \tau)_{(\theta, \phi)}$  shall be an orthonormal rotation of the standard coordinate system along the angles  $(\theta, \phi)$ .

We define  $\theta$  to be the angle which the vector makes with the *xy*-plane (since *z*-axis is normal to the *xy*-plane,  $\theta$  is complementary with the angle between the vector and *z*-axis), and  $\phi$  to be the angle from the *y*-axis to the component of the vector lying in the *xy*-plane. Obviously we associate  $\theta$  with the segments and  $\phi$  with the views.

Since the LORs are undirected we can assume that  $\phi < \pi$ . If it is necessary to

change the direction of the LOR we can always take

$$\theta' = -\theta$$

For a given LOR direction  $(\theta, \phi)$  we define a coordinate system  $(\rho, \alpha, \tau)$  according to the following rules:

- 1. The vectors  $\rho$ ,  $\alpha$  and  $\tau$  are orthonormal.
- 2. The origin of  $(\rho, \alpha, \tau)$  is at the origin of (x, y, z) space.
- 3.  $\tau$  is parallel to the LOR direction described by  $(\theta, \phi)$ .
- 4.  $\rho$  lies in the xy-plane, and coincident with the x-axis when  $\phi = 0$ .

These conditions uniquely describe the  $(\rho, \alpha, \tau)_{(\theta, \phi)}$  coordinate system. The relationship between (x, y, z) and  $(\rho, \alpha, \tau)_{(\theta, \phi)}$  can be seen in Figure 7.1.

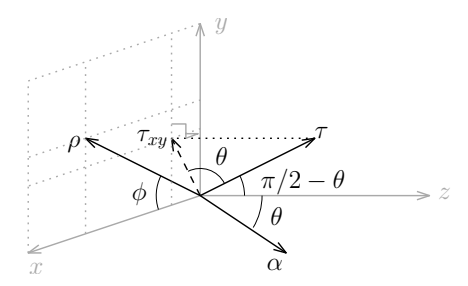


Figure 7.1: Standard (grey) and rotated coordinate systems

The transformation from (x, y, z) to  $(\rho, \alpha, \tau)_{(\theta, \phi)}$  to is given by

$$\begin{bmatrix} \rho \\ \alpha \\ \tau \end{bmatrix} = \begin{bmatrix} -\sin\phi & \cos\phi & 0 \\ -\sin\theta\cos\phi & -\sin\theta\sin\phi & \cos\theta \\ \cos\theta\cos\phi & \cos\theta\sin\phi & \sin\theta \end{bmatrix} \begin{bmatrix} x \\ y \\ z \end{bmatrix}, \tag{T1}$$

and for the transformation to (x, y, z) we have

$$\begin{bmatrix} x \\ y \\ z \end{bmatrix} = \begin{bmatrix} -\sin\phi & -\sin\theta\cos\phi & \cos\theta\cos\phi \\ \cos\phi & -\sin\theta\sin\phi & \cos\theta\sin\phi \\ 0 & \cos\theta & \sin\theta \end{bmatrix} \begin{bmatrix} \rho \\ \alpha \\ \tau \end{bmatrix}.$$
 (T2)

#### 7.1.1.3 Data alignment

In 2D geometry we know that tangential positions are not equidistant. In the three dimensional case, an additional phenomenon is observed. In the previous section we associated a segment s with the angle  $\theta$  that the LORs form with the xy-plane. However this is only valid for the tangential position 0 ( $\rho = 0$ ). As we move towards the boundary of the scanner ( $\rho \to R$  or  $\rho \to -R$ ) angles  $\theta$  become larger.

In Figure 7.2 we can see the LORs for segment 1 ( $\theta = \theta_1$ ) and a particular view  $\phi$  and axial position  $\alpha$ . As we can see the angle formed with the blue plane (xz-axis) becomes steeper as the tangential positions  $\rho$  grow. Also observe that only half of the LORs between detectors of these two rings are drawn, since LORs are undirected the other half is stored to segment -1 ( $\theta = -\theta_1$ ).

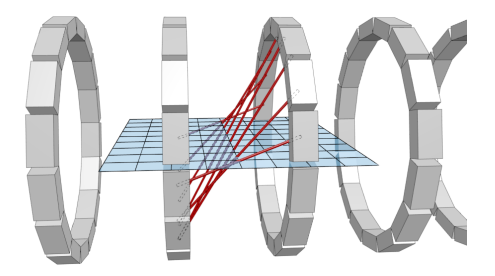


**Figure 7.2:** LORs (in red) for  $\theta = \theta_1$ ,  $\alpha = -0.5$ ,  $\phi = 0$  and various tangential positions, xz-axis in blue

In practice, PET scanners store data based on ring differences ( $\delta = z_1 - z_2$ ) and azimuthal angles ( $\phi$ ). Here,  $z_1$  and  $z_2$  are the positions of two detectors along the axial (z) direction of the scanner, corresponding to different detector rings. The scanner measures LORs (Lines of Response) directly between detector pairs, and the data comes as sinograms in  $\delta$ ,  $\phi$  coordinates.

We symbolize the activity distribution by f(x,y,z) and refer to it as *image*.

We symbolize the emissions measured by the scanner along the LOR with angles  $(\theta, \phi)$  and tangential/axial positions  $(\rho, \alpha)$  with  $g(\rho, \alpha; \theta, \phi)$  and refer to them as *projections*. For a particular angle  $(\theta, \phi)$  we call  $g(\rho, \alpha)$  *projection plane*. The Radon transform gives

$$g(\rho, \alpha; \theta, \phi) = \int_{-\infty}^{\infty} f(x, y, z) d\tau.$$
 (7.1)

The goal of 3D-PET is to reconstruct the activity image f(x, y, z) using the measured radionuclide emissions along LORs  $g(\rho, \alpha; \theta, \phi)$ , i.e. calculate f given its 3D Radon transform g.

#### 7.1.2 Projection-slice theorem

The main tool for many analytical reconstruction algorithms is the projection-slice theorem or Fourier slice theorem (FST). In its 3D version it states that the three-dimensional Fourier transform of a function f restricted to a plane passing through the domain origin is equal to the two-dimensional Fourier transform of a plane consisting of projections with direction parallel to the normal of the original plane (the 3D Radon transform with direction the normal of the original plane).

In particular, let  $F(k_x, k_y, k_z)$  be the three-dimensional Fourier transform of f(x,y,z) (the 'k' symbol indicates that these variables lie in the frequency domain -and are usually integers), and consider a plane formed by a parallel set of LORs with direction  $(\theta,\phi)$ . Using the rotated coordinate system  $(\rho,\alpha,\tau)$  defined above, the Radon transform (projection plane) is defined by (7.1).

It is easy to prove the theorem if we expand the Fourier transforms (to save space we omit the usage of  $\delta$  function). Projection plane  $g(\rho, \alpha; \theta, \phi)$  has two-dimensional Fourier transform

$$G(k_{\rho}, k_{\alpha}; \theta, \phi) = \int \int g(\rho, \alpha; \theta, \phi) \exp(-2\pi i (k_{\rho}\rho + k_{\alpha}\alpha)) d\rho d\alpha$$

Substituting g with the line integral (7.1) we get

$$G(k_{\rho},k_{\alpha};\theta,\phi) = \int \int \int \int f(x,y,z) \exp(-2\pi i (k_{\rho}\rho + k_{\alpha}\alpha)) d\rho d\alpha d\tau.$$

This volume integral over  $(\rho, \alpha, \tau)$  space is converted to (x, y, z) space by using the transform (T1)

$$G(k_{\rho}, k_{\alpha}; \theta, \phi) = \int \int \int \int f(x, y, z) \exp(-2\pi i (k_{\rho}(x\cos\phi + y\sin\phi) + k_{\alpha}(-x\sin\theta\sin\phi + y\sin\theta\cos\phi + z\cos\theta))) dx dy dz$$

By rearranging the terms we get

$$G(k_{\rho}, k_{\alpha}; \theta, \phi) = \int \int \int \int f(x, y, z) \exp(-2\pi i (x(k_{\rho}\cos\phi - k_{\alpha}\sin\theta\sin\phi) + y(k_{\rho}\sin\phi + k_{\alpha}\sin\theta\cos\phi) + z(k_{\alpha}\cos\theta)))) dx dy dz,$$

which happens to be the three-dimensional Fourier transform of f

$$F(k_x, k_y, k_z) = \int \int \int \int f(x, y, z) \exp(-2\pi i(xk_x + yk_y + zk_z)) dz dy dz,$$

if we define

$$\begin{bmatrix} k_x \\ k_y \\ k_z \end{bmatrix} = \begin{bmatrix} -\sin\phi & -\sin\theta\cos\phi \\ \cos\phi & -\sin\theta\sin\phi \\ 0 & \sin\theta \end{bmatrix} \begin{bmatrix} k_\rho \\ k_{\alpha^*} \end{bmatrix}. \tag{P1}$$

Note that this transform is identical to (T2) if we set  $\tau$  equal to zero.

### 7.2 3D Direct Fourier Method

The strategy for the image reconstruction, similarly to the 2D case, is to fill the Fourier space  $F(k_x, k_y, k_z)$  of f by calculating the Fourier transform of  $g(\rho, \alpha)$  for all available planes  $(\theta, \phi)$  and then to calculate the inverse 3D Fourier transform of F.

As we can see from equations (P1), x, y and z are randomly scattered in the 3D domain. As we are interested in finding the values of the image in a regular grid  $(x_i, y_j, z_k)$  of the 3D domain, we must perform interpolation on the data  $(k_x, k_y, k_z)$  given by FST in the Fourier domain. A full 3D interpolation is time consuming and requires large amount of memory, therefore we would like to reduce the 3D interpolation to 2D interpolations (with *number of rings* multitude). Let us note that

FST clearly takes viewgrams and not sinograms as input.

#### 7.2.1 Modified coordinate system

An important observation in [83] is that we can reduce the interpolation in two dimensions if we change the  $(\rho, \alpha)$  coordinate system. In particular if we apply the transformation

$$\alpha^{\star} = \frac{\alpha}{\cos \theta},$$

the Fourier transform of  $g(\rho, \alpha^*)$  becomes

$$G(k_{\rho}, k_{\alpha^{*}}) = \cos \theta \, G(k_{\rho}, k_{\alpha} \cos \theta),$$

and the samples of  $P(k_{\rho},k_{\alpha^{\star}})$  obtained from its Discrete Fourier Transform are located at values of  $k_{\alpha}^{\star}$  at

$$k_{\alpha}^{\star} = \frac{k_{\alpha}}{\cos \theta}.$$

As a result of shearing of  $\alpha$  coordinate, the samples obtained by the FST are given by

$$\begin{bmatrix} k_x \\ k_y \\ k_z \end{bmatrix} = \begin{bmatrix} -\sin\phi & -\tan\theta\cos\phi \\ \cos\phi & -\tan\theta\sin\phi \\ 0 & 1 \end{bmatrix} \begin{bmatrix} k_\rho \\ k_{\alpha^*} \end{bmatrix}.$$
 (P2)

For the the  $k_z$  component we have

$$k_z = k_{\alpha^*},$$

and no interpolation has to be performed in that direction. Therefore only twodimensional interpolation is needed for the components  $(k_x, k_y)$ , considerably improving the speed of the algorithm. In the particular case of data from a cylindrical scanner, the partition along the  $k_y$ -direction has grid spacing  $k_v/cos(\theta)$  (i.e. vectors  $(k_u, k_v)$  of projected space need to be simply orthogonal, and not necessarily orthonormal, and consequently  $k_v$  does not coincide with grid spacing of z). Therefore in [83] the last equation becomes  $z = k_v$ , i.e. it is independent of the angles  $\theta$  and  $\phi$ and so we can reduce the 3D interpolation to 2D interpolations in the xy planes. The projection planes measured by the scanner are naturally sheared by a factor of  $\cos\theta$ , so no processing is required to produce the sheared  $(\rho,\alpha^*)$  coordinate system. In fact, it would be necessary to perform an interpolation to force the data to the orthonormal  $(\rho,\alpha)$  coordinates. This is demonstrated in Figure 7.3. For the direct plane projections  $(\theta=0)$  the distance between the LORs along the  $\alpha$  direction is equal to the ring spacing  $\Delta\alpha$ , while for the rest segments LORs distance is  $\Delta\alpha\cos\theta$ , i.e. as  $\theta$  increases LORs distance along  $\alpha$  axis decreases. [83]

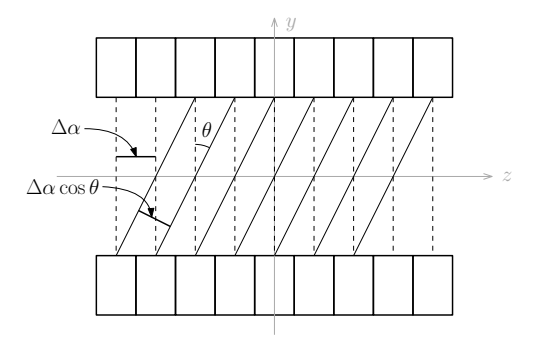


**Figure 7.3:** dashed line: segment 0 ( $\theta = 0$ ), solid line: segment -2 ( $\theta > 0$ )

#### 7.2.2 Inverse Distance Weighting

As we have seen earlier, samples provided by FST are scattered along each slice. The most important part of the algorithm is the interpolation of the Fourier samples on a uniform grid, which will enable us to use the inverse DFT to acquire the original image f.

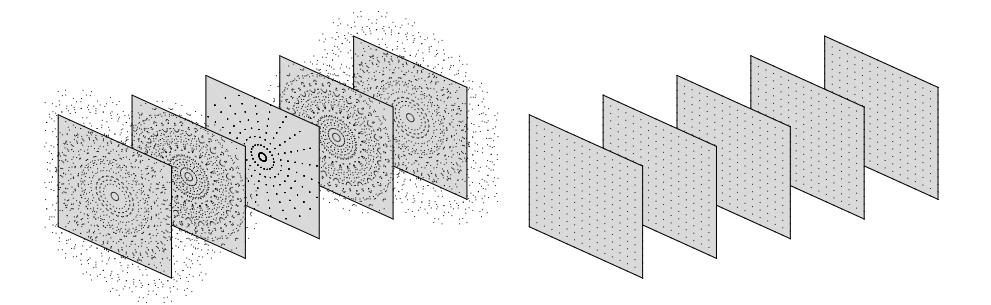


**Figure 7.4:** The figure on the left depicts the samples provided by the Projection-slice theorem, and the one on the right the uniform grid upon which the samples must be interpolated

For example, in Figure 7.4 on the left we can see the Fourier samples available for a scanner with 9 segments, 5 axial positions, 9 views and 16 tangential positions (or simply 5 rings and 32 detectors per ring, with a restriction on the number of views for better visualisation), and on the right we can see the grid upon which the samples must be estimated.

The procedure we are going to follow to achieve this is called *Inverse Distance Weighting* (IDW), as presented in [84]. The foundational principle of the IDW method is that the influence exerted on an interpolated sample should be stronger

from proximal neighbors than from those at a distance. This leads to the value at the target location being calculated as the weighted average of the values from neighboring locations, with the weight applied inversely proportional to the distance between the interpolated point and the surrounding samples. IDW interpolation for the required sample  $(x_i, y_i)$  is given by

$$F(x_i, y_i) = \sum_{j=1}^{N} w_j F(x_j^*, y_j^*), \text{ with } w_j = \frac{h_j^{-p}}{\sum_{k=1}^{N} h_k^{-p}},$$

where  $F(x_j^{\star}, y_j^{\star})$  are the available spectral samples provided by FST,  $w_j$  the associated weight,  $h_j$  represents the distance from the j-th neighboring sample to the point of interpolation, with N denoting the total count of neighboring samples contained within a pre-specified neighbourhood.

A large neighbourhood contains more frequency samples and therefore provides more accurate interpolation. However, more samples slow down the algorithm. Selection of the neighbourhood can be performed in two ways: the neighbourhood can be selected to have specified length L or specified number of neighbours N. The latter one provides more accurate results in the border region of the scanner where sample density is low, but is quite slow and requires us to save the neighbourhoods on the disc. Therefore we will use the fixed length method.

## 7.3 3D Direct Fourier Method (DFM3D)

We implement in STIR [68] the reconstruction algorithm DFM3D, which recovers the missing data and performs 3D reconstruction.

#### 7.3.1 Outline of the algorithm

The algorithm combines [85] and [84] in the following steps:

- Step 1 Reconstruct an initial estimate of the image using the available projections from the direct plane (segment 0) by use of 2D-DFM (for each sinogram) [potentially any 2D reconstruction algorithm can be used here]:
  - 1a. Pad tangential positions with zeroes.

- *1b.* Use Fast Fourier Transform (FFT) for each view, and place the data accordingly to the 2D space using FST.
- 1c. Use IDW (2D) to interpolate the data to a rectangular grid.
- 1d. Use Inverse Fast Fourier Transform (IFFT) 2D to reconstruct the slice.

#### Step 2 Reprojection.

- 2a If you decide to keep all reprojected data, pad axial positions accordingly.
- **2b** Forward project the initial image to calculate the projections for the axial positions not measured by the scanner.
- Step 3 From the measured and calculated data use 3D-DFM to reconstruct the image:
  - *3a.* Use FFT 2D for each viewgram (using the desired oversampling) and place the data accordingly in the 3D Fourier space using FST.
  - **3b.** Use IDW (2D) to interpolate the available samples onto the uniform grid.
  - *3c.* Use IFFT 3D on the interpolated samples (and extract the required values if oversampling is used).

Step 3 is the 3D equivalent of Step 1. Step 1 is elaborated in another paper of ours [82], which uses Gridding Method [69] in place of IDW.

STIR's FBP3DRP follows the same procedure, but instead of DFM uses FBP [86]. Furthermore, it is not handy to directly transfer FBP3DRP's missing data compensation method in any algorithm that is not based on backprojection, as the backprojection symmetries permeate the code (principally through the RelatedViewgrams class [87]).

#### 7.3.2 Data requirements

The present form of the algorithm poses the following requirements on the form of the input data:

i) Each segment s should have *number of rings*-|s| axial positions (for other forms of the axial position vector, the algorithm may or may not work).

- ii) The data need to be arc-corrected, as the formulae work for uniform partition of tangential positions; otherwise interpolation would be necessary.
- iii) Tangential positions should be even (in the case of STIR implementation, for the library's FFT function).
- iv) Number of rings should be even (in the case of STIR implementation, for the library's FFT function).

#### 7.3.3 Implementation of the algorithm

Note that we take the grid spacing along the first direction to be the one in x-direction, and the grid-spacing along the second direction to be the same with the z-direction.

#### 7.3.3.1 Oversampling

As we have seen in the 2D case, due to the finite extent of the discrete Fourier transform, artifacts are introduced in the reconstructed image. These artifacts can be reduced by increasing the sampling density in the Fourier domain. This process is referred to as "oversampling". When more samples are available in the Fourier domain, interpolation yields more accurate results.

Fourier domain oversampling is easily achieved by zero-padding, i.e. extending the projection data by adding elements containing zeroes. Due to the sheared axial coordinate system oversampling is only necessary along the  $\rho$  direction (no interpolation is performed in  $\alpha$  direction). Fourier domain oversampling by a factor of s is achieved by adding  $(s-1)N_x$  zeroes along  $\rho$  dimension, forming the padded projection plane  $g^*(\rho, \alpha^*; \theta, \phi)$  which is  $sN_x \times N_z$  in size (where  $N_x$  is the number of tangential positions and  $N_z$  the number of axial positions). We set the transform of the padded projections to be

$$G^{\star}(k_{\rho}, k_{\alpha^{\star}}; \theta, \phi) = \frac{1}{s}G(\frac{k_{\rho}}{s}, k_{\alpha^{\star}}; \theta, \phi),$$

the term 1/s is added to compensate for the s-fold increase in the amount of data placed in the Fourier domain, so that image recovery is independent of the degree of oversampling used.

The amount of artifacts present in the reconstructed image is directly related to the size of the imaged object. Artifacts increase as the object becomes larger, which in turn needs larger oversampling to be compensated for. Oversampling by a factor s will increase the running time of the algorithm roughly by a factor of s, therefore there is a strong motivation to use as little oversampling as possible. As we can see by experiments, 2-fold oversampling is sufficient in most cases. If the activity is confined to the center of the field of view, it may be possible to produce reasonable images without oversampling. On the other hand, if a substantial portion of the activity is in the periphery, 4-fold oversampling may be required.

Padding with respect to z axis is not mandatory. However, to utilize all of the missing data we could pad to  $2 \times number\ of\ rings$ , i.e. use two times more tangential positions, and fill with zeroes the extra ones. This reduces artifacts. The change in formula is the aforementioned.

#### 7.3.3.2 Step 2: Reprojection

We use forward projection to calculate the integral of f (the image) along the LORs not measured by the scanner.

STIR, of course, has built in function for performing forward projection based on Siddon's algorithm [80], however, one could easily create a custom-made such function, by using trapezoidal quadrature to calculate the integral of f, and trilinear interpolation [88] to estimate the value of f in the quadrature nodes. Of course, for speed's shake it is crucial one does not do full forward projection, but only with respect to the missing LORs; that's why we name the procedure reprojection. Let us note that except for the standard reprojection in the spatial domain, reprojection can take place in the Fourier domain, with apparent speed improvement [83]. For compatibility with STIR's 'forward\_project' one must use bin size = z voxel size/2.

Let us underline that FST requires that each segment number has constant number of axial positions (i.e. for each  $\theta$  constant number of v's); however, reprojection assigns to each segment  $|segment\ number| + number\ of\ rings$  axial positions, i.e. increases number of axial positions. We can either set a constant number of axial positions (equal to the number of rings  $num\_rings$ ), keep the required axial positions

generated by forward\_project and discard the rest, or pad our data to  $2 \times number$  of rings and therefore fit all the axial positions created by forward\_project (using zeroes for the axial positions not generated by forward projecting) (Step 2a). However, depending on whether a segment is even or odd, its partition will differ; for odd segments there is an axial position passing through the center of the scanner, but not in the even ones. Padding for odd number of axial positions doesn't yield as good results as for the even case.

#### 7.3.3.3 Step 2b and 3b: IDW

We implement the first method IDW method by specifying a predefined length (IDWa) instead of the number of neighbours, because it is faster. In order to improve the running time further, instead of iterating over the interpolation points, we iterate over the sample points and we assign the contribution onto nearby interpolation points. The results of IDWa are not lesser in quality than Matlab's built-in griddata function.

#### 7.3.3.4 Step 3a: 3D interpolation turned to 2D

Let us note that partition for *x* is essentially non-uniform, but as STIR automatically arc-corrects data we can regard it as uniform.

#### 7.3.3.5 Noise filter

As STIR's FBP3DRP has an enhanced variant beyond the Ramp filter (the latter being an integral component of the mathematical formulation of FBP), we also added the option of the Hanning filter [89] for DFM3D. To implement the Hanning filter over a three-dimensional dataset, we begin by creating three distinct Hanning sequences, one for each dimension, custom-fit to its length. We compute each element in these sequences with the formula  $0.5(1-\cos(2\pi n/(N-1)))$ , where 'n' marks the current position within the sequence, and 'N' signifies the total length of that dimension. We then adjust each point in our three-dimensional data array by multiplying it with the corresponding values from each dimension's Hanning sequence. The effect of applying the Hanning filter in this manner is to gradually reduce the contributions of data points at the edges of each dimension, which mitigates abrupt changes at the

boundaries that can introduce artifacts into frequency analysis.

# 7.4 'Artificial scanner' as a means of extrapolation of missing data

#### 7.4.1 Missing data

In order to calculate the Fourier transform of g used in FST, all non-zero projections  $g(\rho, \alpha)$  must be known. However, since the scanner has finite axial extent, measurements are not available for all axial positions  $\alpha$ . For example, as we can see in Figure 7.5, considering the projections for segment 2 of the scanner, only 3 axial positions can be measured and 4 more have to be somehow calculated.

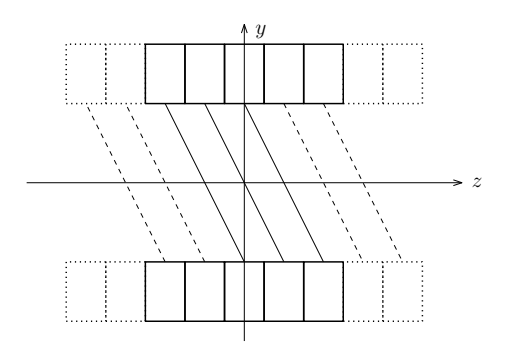


Figure 7.5: LORs for segment 2, solid line: measured, dashed line: missing

In particular let us consider a scanner with r rings (numbered from  $-\lfloor r/2 \rfloor$  to  $\lfloor r/2 \rfloor$ ). For the segment s, projections along r + |s| axial positions have non-zero values (i.e. axial positions  $-\lfloor r/2 \rfloor - |s|/2 \ldots \lfloor r/2 \rfloor + |s|/2$ ) but only r - |s| are measured by the scanner (i.e. axial positions  $-\lfloor r/2 \rfloor + |s|/2 \ldots \lfloor r/2 \rfloor - |s|/2$ ), therefore projections along 2|s| axial positions have to be estimated.

In order to estimate missing projections, we notice that for the segment s=0 all axial positions are known, therefore we could use FST. Furthermore since  $\theta=0$ , this reduces to the standard two-dimensional case. Therefore we can reconstruct an initial estimation of the image f by using the available data from segment zero and then forward-project this image to acquire the necessary projections.

Initial image estimation can be reconstructed by means of standard 2D PET in each axial position of segment zero (i.e. in each ring). Forward-projection is simply

the evaluation of a standard line integral, which can be performed using a simple quadrature rule.

Therefore a required projection is given by

$$g(\boldsymbol{\rho}, \boldsymbol{\alpha}; \boldsymbol{\theta}, \boldsymbol{\phi}) = \int f(x, y, z) d\tau,$$

where (x, y, z) are given by (T2) in relation to  $(\rho, \alpha, \tau)$ . By discretizing the above integral we get

$$g(\boldsymbol{\rho}, \boldsymbol{\alpha}, \boldsymbol{\theta}, \boldsymbol{\phi}) = \sum_{i=1}^{n} f(x(\tau_i; \boldsymbol{\rho}, \boldsymbol{\alpha}, \boldsymbol{\theta}, \boldsymbol{\phi}), y(\tau_i; \boldsymbol{\rho}, \boldsymbol{\alpha}, \boldsymbol{\theta}, \boldsymbol{\phi}), z(\tau_i; \boldsymbol{\rho}, \boldsymbol{\alpha}, \boldsymbol{\theta}, \boldsymbol{\phi})) \, \delta \tau.$$

Since f is know in a grid  $(x_i, y_j, z_k)$ , a trilinear interpolation is performed to evaluate it for the required (x, y, z). (In particular we are interested in the tube integral of f; this can be simply achieved by multiplying the above quantity by  $\delta \rho \delta \alpha$ .)

#### 7.4.2 Artificial scanner

Skipping the missing data extrapolation procedure is possible only for the special cases that there are no missing data, as in the data depicted in Fig. 7.6.

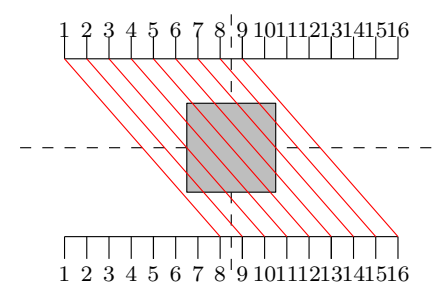


Figure 7.6: No missing data case

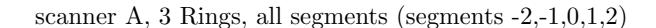
We can exploit a method to forward-project the initial image –such as Ray-Tracing– if we utilize existing tomographic software such as STIR, or even a general mathematical package such as MATLAB's radon function. In order to do so, we need to construct an artificial scanner which will be able to calculate our missing projections.

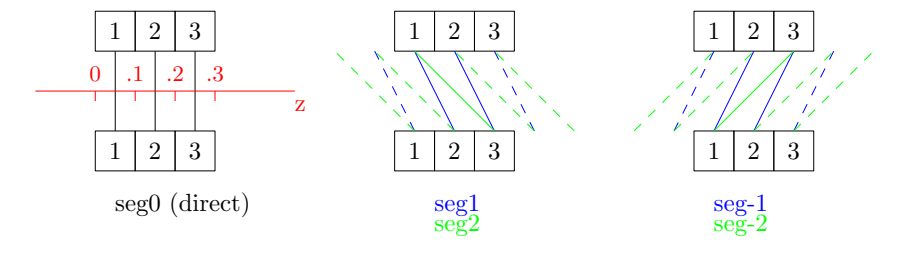
For the example in Fig. 7.6, we can create a simple scanner, i.e. 128 tangential positions, 64 views, 16 rings and maximum ring difference 15 (segments =

 $-15\dots 15$ ), and in general the default settings of create\_projdata\_template. The image is a simple cube spanning  $[-R/2,R/2]\times[-R/2,R/2]$  (R is the ring radius) in the axial direction, and rings 7–10 in the transaxial direction. Note that we are forced to set z\_voxel\_size := ring\_spacing/2, thus despite the cube spanning slices 5–12 in the original image, it spans only rings 7–10 after the projection. However, in the particular case that segment s has number of rings-|s| axial positions, we skip steps 1 and 2 of the algorithm by constructing an 'artificial scanner' as follows.

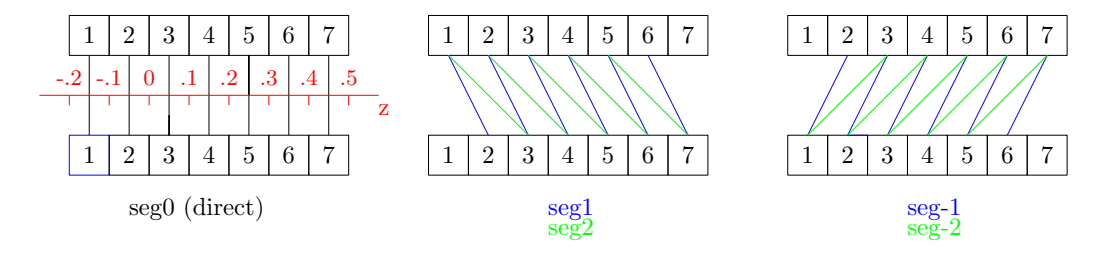
Let us assume we have a scanner with N rings, and we want to reconstruct missing data for this scanner. This scanner has 2N-1 segments. For each segment k, only N-k sinograms are measured and therefore k sinograms have to be extrapolated.

The easiest way to extrapolate the missing data is to construct an artificial scanner with (N-1)+N+(N-1)=3N-2 rings. By associating the (1...N) rings of the original scanner with the rings (N...2N-1) of the artificial scanner, rings (1...N-1) can be used to extrapolate the missing sinograms of negative segments (-N...-1) of the original scanner, and rings (2N...3N-2) can be used to extrapolate the missing sinograms of positive segments (1...N) of the original scanner.





scanner B, 7 Rings, 5 segments (segments -2,-1,0,1,2)





If scanner A has N rings, scanner B must have 2\*N+1 rings and then  $ring_{\text{scannerA}} = ring_{\text{scannerB}} - N + 1$ 

Figure 7.7: Artificial vs. real scanner

In Figure 7.7 observe that the sinogram of segment (set of sinograms with the same ring difference) k and axial position a (LOR starts in ring a and ends in ring  $a+segment\ number$ ) of the original scanner is actually the sinogram of segment k and axial position N+a-1 of the artificial scanner. Therefore we can extract the required sinograms from the artificial scanner.

The difficult part of the artificial scanner coding is finding the correspondence between the indices of the original and the artificial scanner.

After reading the STIR data vector, we want to transform it into a 4D array, that will allow us to make easy use of the data. STIR stores the data (measured values along LORs) as a 4-dimensional array. The first dimension corresponds to the tangential position, the second to the axial position, the third to the view and the

fourth to the segment. Let sp:=number of tangential positions, sa:=number of axial positions for segment 0 (number of rings), sth:=number of views and sphi:=number of segments. We cannot use the same array as in STIR because we have to include the missing data. STIR array has variable number of axial positions for each segment. After we include the missing data, the number of axial positions will be fixed (and equal to the ring number), therefore we will read and store the data into a 4-dimensional array with fixed dimensions (sp,sa,sth,sphi).

We will present a simplified version of the method, as would apply in case we were able to use a Matlab's "cell" array, which allows its elements to be of different type. So, we create cell data to save data for each segment, as each segment has different number of axial positions, and therefore arrays cannot be used.

We construct a vector *axial*, which indicates the number of axial positions for each segment; in particular, in its k-th position, we place the number of axial positions of segment k - sa.

We indicate the index of a segment with *iphi*, and the index of an axial position with *ia*.

For the segments with negative index, sinogram with iphi, ia of the initial scanner corresponds to iphi, ia + iphi - 1 of the artificial scanner.

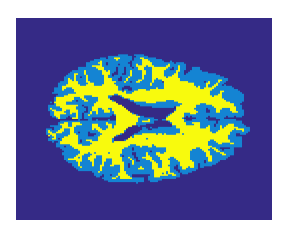
For the segments with positive index, sinogram *iphi*, *ia* is in positions *iphi*, *iphi*+ *ia* of the artificial scanner.

It is important to note that the artificial scanner works even when there is a jump in the central segment's axial position number, instead of the typical incremental increase/decrease relative to its prior and following segments, respectively. In such a case, it only necessitates a suitable increase in the padding of the axial positions.

## 7.5 Comparison of algorithms

#### 7.5.1 Phantom and data creation

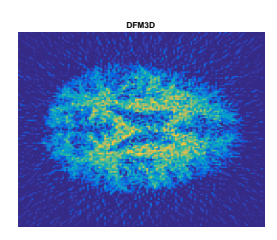
We will be performing comparisons with a phantom that was downloaded from Brainweb; it is Subject 04 Discrete Model, with x-y-z dimensions  $362 \times 434 \times 362$ , saved as unsigned byte 0 to 255. [90] Essentially this is MRI data, but was turned into PET data, by applying one value to each ROI with Matlab.



**Figure 7.8:** Brainweb brain phantom

Scanner interfiles and sinograms (with the addition of Poisson noise) were created in STIR; the latter together with the parameter files and the reconstructed images via a bass script allowing automation of the procedure. For sinogram creation fwdtest with type 'Matrix' and 'matrix type := ray tracing' were used (otherwise projecting image using fwdtest with type 'Ray Tracing' some of the direct sinograms might swap parts -issue related to the symmetries used). Assuming that the number of tangential positions is even, DFM3D code should work for every scanner.

We will compare DFM3D with STIR's FBP3DRP.



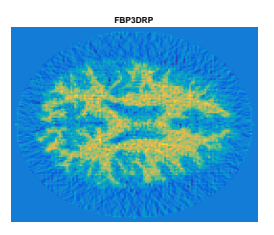


**Figure 7.9:** Reconstructed images of DFM3D and FBP3DRP with a 0.1 Poisson noise scaling factor.

#### 7.5.2 Image Quality Metrics

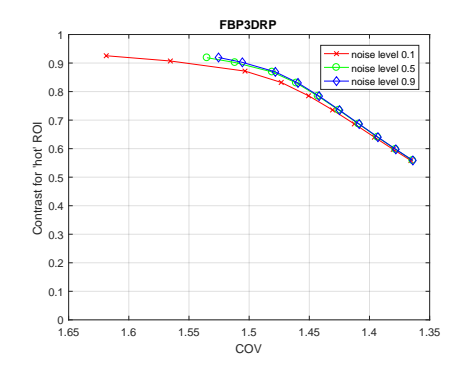
To adjust the NEMA standard test for the Brainweb phantom, we regard the 'hot sphere' as the ROI with a value of 4, the 'cold sphere' as the ROI with a value of 0, and the 'background' as the ROI with a value of 1.

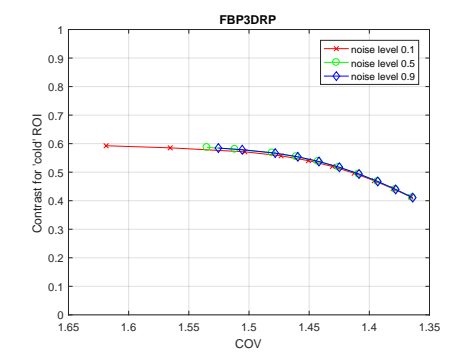
For details regarding how ROIs are chosen and the contrast metrics, refer to Section 5.4.2, which describes the methodology applied for 2D PET. The same approach is followed here, adjusted for the specific characteristics of the Brainweb phantom used in 3D PET.

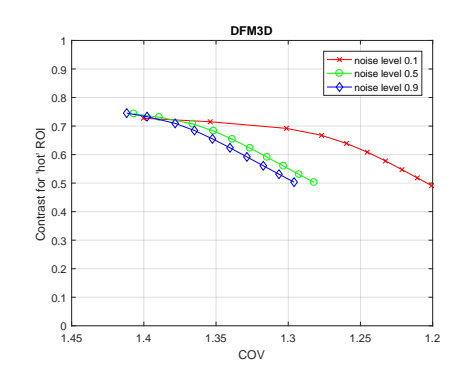
For STIR, to generate different levels of Poisson noise, the forward-projected sinograms were scaled with factors of 0.1, 0.5, and 0.9 before calling a Poisson random number generator.

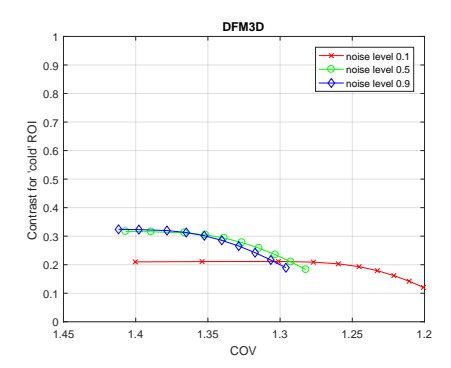
#### 7.5.2.1 Noise Sensitivity and Algorithm Behavior

DFM3D does not become less sensitive to noise as the image gets more blurred/smoothed. This behavior could potentially suggest non-linearity of noise propagation; it must be further investigated.





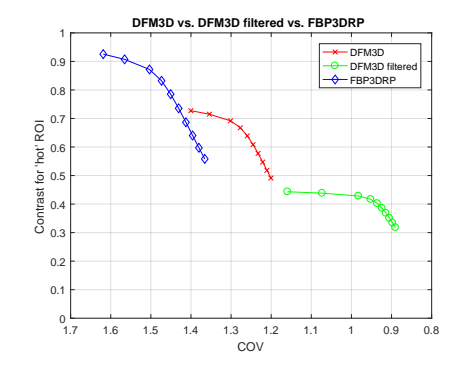


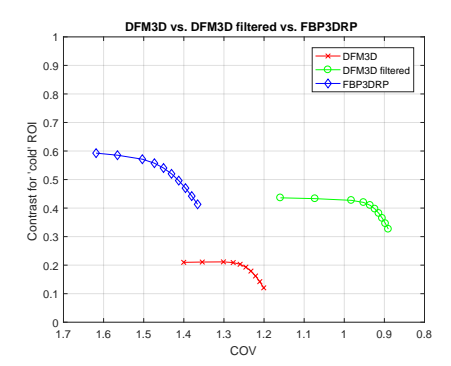


## 7.5.2.2 Contrast vs. CoV: the 10 different postfilters at the highest noise level data are the parameters

Although DFM3D demonstrates convergence of the values at the three noise levels when the postfilter is strongest, which would potentially be a hint for linearity of noise propagation, further investigation is required to determine the nature of the algorithm. This is necessary because its curve patterns differ significantly from those in previous chapters, and most importantly, its behavior with respect to the automated Hanning filter is unique. Specifically, the filter increases the contrast for the 'cold' ROI, but decreases it for the 'hot' ROI.

In any case, FBP3DRP exhibits superior contrast overall (though with slightly noisier images), particularly for the 'cold' ROI.





## 7.5.3 Complexity of DFM3D versus FBP3DRP

Let us assume  $sphi \sim sa \sim sp \sim sth \sim N \in \mathbb{N}$ , where sphi is the number of segments, sa the number of axial positions, sp the number of tangential positions, sth the number of views, then the order of computational complexity of both DFM3D and

FBP3DRP is  $O(N^4 \log_2 N)$  (the filtering has the bulk of the calculations for the later).

## **Bibliography**

- [1] M. I. Belishev. On an approach to multidimensional inverse problems for the wave equation. *Sov. Math. Dokl.*, 36:481–484, 1988.
- [2] M. I. Belishev. Boundary control and wave fields continuation. *LOMI Preprint*, *P-1-90*, 1990. In Russian.
- [3] M. I. Belishev and A. P. Kachalov. Boundary control and quasiphotones in the problem of reconstruction of a riemannian manifold via dynamical data. *Zapiski Nauch. Semin. POMI*, 203:21–51, 1992. In Russian; Engl. Transl.: J. Math. Sci., 79 no 4 (1996).
- [4] M. I. Belishev and Ya. V. Kurylev. To the reconstruction of a Riemannian manifold via its spectral data (BC-method). *Commun. Part. Diff. Eqns*, 17:767–804, 1992.
- [5] M. I. Belishev and Ya. V. Kurylev. Nonstationary inverse problem for the multidimensional wave equation 'in the large'. *Zapiski Nauch. Semin. LOMI*, 165:21–30, 1987. In Russian; Engl. Transl.: J. Sov. Math., 50 no 6 (1990).
- [6] A. Katchalov, Y. Kurylev, and M. Lassas. *Inverse Boundary Spectral Problems*. Chapman and Hall/CRC Monographs and Surveys in Pure and Applied Mathematics vol 123, Boca Raton, FL, 2001.
- [7] M. I. Belishev. On Kac's problem of the determination of shape of a domain from the spectrum of the Dirichlet problem. *Zapiski Nauch. Semin. POMI*, 173:30–41, 1988. In Russian; Engl. Transl.: J. Sov. Math., 55 (1991).

- [8] M. I. Belishev. Boundary control method and inverse problems of wave propagation. 1:340–345, 2006.
- [9] S. A. Avdonin and M. I. Belishev. Dynamical inverse problem for the Schrödinger equation (the BC-method). *Proc. St-Petersburg Math. Soc.*, 10:3–18, 2004. In Russian; Engl. Transl.: American Mathematical Society Translation Series vol 2 (2005).
- [10] S. Avdonin, S. Lenhart, and V. Protopopescu. Determining the potential in the Schrödinger equation from the Dirichlet to Neumann map by the boundary control method. *J. Inverse Ill-Posed Problems*, 13:317–330, 2005.
- [11] M. I. Belishev. The Calderon problem for two-dimensional manifolds by the BC-method. *SIAM J. Math. Anal.*, 35(1):172–182, 2003.
- [12] Xiaochun Liu and Bert-Wolfgang Schulze. *Boundary value problems with global projection conditions*. Springer International Publishing, 2018.
- [13] Stephan Rempel and B.-W. Schulze. Index theory of elliptic boundary problems. *Mathematische Monographien*, 55, 1982.
- [14] B.-W. Schulze. *Boundary value problems and singular pseudo-differential operators*. Interscience Series of Texts, Monographs, and Tracks, 1998.
- [15] V. E. Nazaikinskii, A. Y. Savin, B. W. Schulze, and B. Y. Sternin. *Elliptic theory on singular manifolds*. Chapman and Hall/CRC, 2005.
- [16] Gohar Harutyunyan and Bert-Wolfgang Schulze. *Elliptic Mixed, Transmission and Singular Crack Problems*, volume 4. European Mathematical Society, 2007.
- [17] L. B. de Monvel. Boundary problems for pseudo-differential operators. *Acta Mathematica*, 126(1):11–51, 1971.
- [18] M. F. Atiyah, V. K. Patodi, and I. M. Singer. Spectral asymmetry and Riemannian geometry. I. *Mathematical Proceedings of the Cambridge Philosophical Society*, 77(1):43–69, January 1975.

- [19] M. F. Atiyah, V. K. Patodi, and I. M. Singer. Spectral asymmetry and Riemannian geometry. II. *Mathematical Proceedings of the Cambridge Philosophical Society*, 78(3):405–432, November 1975.
- [20] M. F. Atiyah, V. K. Patodi, and I. M. Singer. Spectral asymmetry and Riemannian geometry. III. *Mathematical Proceedings of the Cambridge Philosophical Society*, 79(1):71–99, January 1976.
- [21] M. G. Krein. Determination of the density of an inhomogeneous string from its spectrum. *Doklady Akad. Nauk. SSSR*, 76:345–348, 1951. In Russian.
- [22] M. G. Krein. On inverse problems for an inhomogeneous string. *Doklady Akad. Nauk. SSSR*, 82:669–672, 1951. In Russian.
- [23] A. Blagovestcenskii. The local method of solution of the non-stationary inverse scattering problem for an inhomogeneous string. *Trudy Mat. Inst. Steklova*, 115:28–38, 1971. In Russian.
- [24] M. I. Belishev. An approach to multidimensional inverse problems for the wave equation. *Dolkl. Akad. Nauk SSSR*, 297:524–527, 1987. Engl. Transl.: Soviet Math. Dokl. 36 (1988), 481-484.
- [25] M. I. Belishev and Ya V. Kurylev. Nonsteady inverse problem for the multidimensional wave equation "in the large". *Journal of Soviet Mathematics*, 50(6):1944–1951, 1990.
- [26] Alexander Kachalov, Yaroslav Kurylev, and Matti Lassas. *Inverse boundary spectral problems*. Chapman and Hall/CRC, 2001.
- [27] A. Blagovestcenskii. *The nonselfadjoint inverse matrix boundary problem* for a hyperbolic differential equation, pages 38–62. Izdat. Leningrad Univ., Leningrad, 1971. In Russian.
- [28] M. I. Belishev and A. S. Blagovestchenski. *Multidimensional analogs of the Gel'fand-Levitan-Krein equations in inverse problems for the wave equation*, pages 50–63. Nobosibirsk: Nauka, 1992. In Russian.

- [29] Hiroshi Isozaki and Yaroslav Kurylev. *Introduction to Spectral Theory and Inverse Problem on Asymptotically Hyperbolic Manifolds*. 2011. arXiv preprint arXiv:1102.5382.
- [30] Mikhail I. Belishev. The Calderon problem for two-dimensional manifolds by the BC-method. *SIAM J. Math. Anal.*, 35(1):172–182, 2003.
- [31] Mikhail I. Belishev and Naoki Wada. A C\*-algebra associated with dynamics on a graph of strings. *Journal of the Mathematical Society of Japan*, 67(3):1239–1274, 2015.
- [32] M. I. Belishev and M. N. Demchenko. Elements of noncommutative geometry in inverse problems on manifolds. *Journal of Geometry and Physics*, 78:29–47, 2014.
- [33] M. Belishev, M. Demchenko, and A. Popov. Noncommutative geometry and the tomography of manifolds. *Transactions of the Moscow Mathematical Society*, 75:133–149, 2014.
- [34] Mikhail Igorevich Belishev. On algebras of three-dimensional quaternionic harmonic fields. *arXiv preprint arXiv:1611.08523*, 2016.
- [35] M. I. Belishev. A unitary invariant of a semi-bounded operator in reconstruction of manifolds. *Journal of Operator Theory*, pages 299–326, 2013.
- [36] M. Belishev and S. Simonov. Wave model of the Sturm–Liouville operator on the half-line. *St. Petersburg Mathematical Journal*, 29(2):227–248, 2018.
- [37] Mikhail I. Belishev. Boundary control and tomography of Riemannian manifolds (the BC-method). *Russian Mathematical Surveys*, 72(4):581, 2017.
- [38] V. E. Nazaikinskii, B.-W. Schulze, and B. Y. Sternin. *Quantization Methods* in the Theory of Differential Equations. CRC Press, 2002.
- [39] Chris Heunen et al. A topos for algebraic quantum theory. *Comm. Math. Phys.*, 291:63–110, 2009.

- [40] Chris Heunen et al. The Gelfand spectrum of a noncommutative C\*-algebra: a topos-theoretic approach. *Journal of the Australian Mathematical Society*, 90(1):39–52, 2011.
- [41] David Dos Santos Ferreira et al. The linearized Calderón problem in transversally anisotropic geometries. *International Mathematics Research Notices*, 2020(22):8729–8765, 2020.
- [42] Guillaume Bal. Mathematical Tools for Imaging and Inverse Problems. 2024. Available at https://www.stat.uchicago.edu/guillaumebal/PAPERS/Mathematical\_Tools.pdf.
- [43] V. E. Nazaikinskii, A. Y. Savin, B. W. Schulze, and B. Y. Sternin. Elliptic theory on singular manifolds. *Chapman and Hall/CRC*, 2005.
- [44] B.-W. Schulze, B. Sternin, and V. Shatalov. *Differential equations on singular manifolds: Semiclassical theory and operator algebras*, volume 15. Wiley-VCH, 1998.
- [45] L. Hörmander. *The analysis of linear partial differential operators*, volume Vols. 1-4. Springer-Verlag, New York, 1983/85.
- [46] B.-W. Schulze. *Pseudo-differential operators on manifolds with singularities*. Elsevier, 1991.
- [47] Mikhail Semenovich Agranovich and Marko Iosifovich Vishik. Elliptic problems with a parameter and parabolic problems of general type. *Uspekhi Matematicheskikh Nauk*, 19(3):53–161, 1964.
- [48] Thomas Krainer and Bert-Wolfgang Schulze. On the inverse of parabolic systems of partial differential equations of general form in an infinite spacetime cylinder. pages 93–278, 2002.
- [49] Anna Kirpichnikova and Yaroslav Kurylev. Inverse boundary spectral problem for riemannian polyhedra. *Mathematische Annalen*, 354(3):1003–1028, 2012.

- [50] B.-W. Schulze. Pseudo-differential operators on manifolds with singularities. 1991.
- [51] Bert-Wolfgang Schulze. The Mellin pseudo-differential calculus on manifolds with corners. In *Symposium "Analysis on Manifolds with Singularities"*, *Breitenbrunn*. Vieweg+ Teubner Verlag, Wiesbaden, 1992.
- [52] B.-Wolfgang Schulze. Operators with symbol hierarchies and iterated asymptotics. *Publications of the Research Institute for Mathematical Sciences*, 38(4):735–802, 2002.
- [53] Gohar Harutyunyan and Bert-Wolfgang Schulze. Elliptic mixed, transmission and singular crack problems. *European Mathematical Society*, 4, 2007.
- [54] D. Calvo, C.-I. Martin, and B.-W. Schulze. Symbolic Structures on Corner Manifolds (Microlocal Analysis and Asymptotic Analysis). *Kyoto*, 1397:22– 35, 2004.
- [55] M. I. Belishev. Recent progress in the boundary control method. *Inverse Problems*, 23(5):R1, 2007.
- [56] L. C. Evans. *Partial differential equations*, volume 19. American Mathematical Society, 2022.
- [57] Partha Roy Chaudhuri. Modern Optics. 2018. Retrieved from https://archive.nptel.ac.in/courses/115/105/115105104/.
- [58] S. Huang. Mathematical models of wavelength division multiplexing devices. 2000. Doctoral dissertation, Texas Tech University.
- [59] B. P. Singh and K. C. Rustagi. *NonLinear Optics*. 2015. Retrieved from https://archive.nptel.ac.in/courses/115/101/115101008/.
- [60] Nachiketa Tiwari. *Sound Propagation Through Media*. 2014. Retrieved from https://archive.nptel.ac.in/courses/112/104/112104176/.

- [61] W. H. Press. *Numerical recipes 3rd edition: The art of scientific computing*. Cambridge University Press, 2007.
- [62] A. Ticknor, R. Easton, and H. Barrett. Two-dimensional Radon-Fourier transformer. In *Optical Engineering*, volume 24, page 240182, 1985.
- [63] G. Zeng and G. Gullberg. Can the backprojection filtering algorithm be as accurate as the filtered backprojection algorithm? In *Proceedings of 1994 IEEE Nuclear Science Symposium NSS'94*, volume 3, pages 1232–1236, 1994.
- [64] K. Hanson. On the Optimality of the Filtered Backprojection Algorithm. *Journal of Computer Assisted Tomography*, 4:361–363, 1980.
- [65] R. Gordon. A tutorial on art (algebraic reconstruction techniques). *IEEE Transactions on Nuclear Science*, 21:78–93, 1974.
- [66] N. Laird, N. Lange, and D. Stram. Maximum likelihood computations with repeated measures: Application of the EM algorithm. *Journal of the American Statistical Association*, 82:97–105, 1987.
- [67] M. Hudson and R. Larkin. Accelerated image reconstruction using ordered subsets of projection data. *IEEE Transactions on Medical Imaging*, 13(4):601– 609, 1994.
- [68] K. Thielemans, C. Tsoumpas, S. Mustafovic, T. Beisel, P. Aguiar, N. Dikaios, and M. W. Jacobson. STIR: software for tomographic image reconstruction release 2. *Physics in Medicine and Biology*, 57(4):867, 2012.
- [69] H. Schomberg and J. Timmer. The gridding method for image reconstruction by Fourier transformation. *IEEE Transactions on Medical Imaging*, 14(3):596–607, 1995.
- [70] A. S. Fokas, A. Iserles, and V. Marinakis. Reconstruction algorithm for single photon emission computed tomography and its numerical implementation. *Journal of The Royal Society Interface*, 3(6):45–54, 2006.

- [71] G. A. Kastis, D. Kyriakopoulou, A. Gaitanis, Y. Fernández, B. F. Hutton, and A. S. Fokas. Evaluation of the spline reconstruction technique for PET. *Medical Physics*, 41(4):042501, 2014.
- [72] S. Treitel. The complex Wiener filter. *Geophysics*, 39:169–173, 1974.
- [73] J. C. Principe, B. De Vries, and P. G. de Oliveira. The gamma-filter-a new class of adaptive IIR filters with restricted feedback. *IEEE Transactions on Signal Processing*, 41(2):649–656, 1993.
- [74] T. Nodes and N. Gallagher. Median filters: Some modifications and their properties. *IEEE Transactions on Acoustics, Speech, and Signal Processing*, 30:739–746, 1982.
- [75] National Electrical Manufacturers Association. Performance measurements of positron emission tomographs, 2007. NEMA Standards Publication NU 2-2007.
- [76] L. A. Kunyansky. A new SPECT reconstruction algorithm based on the Novikov explicit inversion formula. *Inverse problems*, 17(2):293, 2001.
- [77] N. E. Protonotarios, A. S. Fokas, K. Kostarelos, and G. A. Kastis. The attenuated spline reconstruction technique for single photon emission computed tomography. *Journal of the Royal Society Interface*, 15(148):20180509, 2018.
- [78] R. G. Novikov. An inversion formula for the attenuated X-ray transformation. *Arkiv för matematik*, 40(1):145–167, 2002.
- [79] A. S. Fokas and R. G. Novikov. Discrete analogues of đ-equation and of Radon transform. *Comptes rendus de l'Académie des sciences. Série 1, Mathématique*, 313(2):75–80, 1991.
- [80] M. L. Egger, C. Joseph, and C. Morel. Incremental beamwise backprojection using geometrical symmetries for 3D PET reconstruction in a cylindrical scanner geometry. *Physics in Medicine and Biology*, 43(10):3009, 1998.

- [81] L. Marple. Computing the discrete-time "analytic" signal via FFT. *IEEE Transactions on signal processing*, 47(9):2600–2603, 1999.
- [82] Implementation of 2 analytic 2D PET reconstruction algorithms in stir and their performance evaluation. To be submitted.
- [83] C. W. Stearns, D. A. Chesler, and G. L. Brownell. Accelerated image reconstruction for a cylindrical positron tomograph using fourier domain methods. *IEEE Transactions on Nuclear Science*, 37(2):773–777, 1990.
- [84] Y. Li, A. Kummert, F. Boschen, and H. Herzog. Analysis on Fourier-based inversion methods for 3D-PET reconstruction. In *Multidimensional (nD)*Systems, 2007 International Workshop on, pages 75–81. IEEE, 2007.
- [85] S. Matej and R. M. Lewitt. 3D-FRP: Direct Fourier reconstruction with Fourier reprojection for fully 3-D PET. *IEEE Transactions on Nuclear Science*, 48(4):1378–1385, 2001.
- [86] PDF file with (somewhat incomplete) documentation on the STIR implementation of the 3DRP algorithm. Available via: http://stir.sourceforge.net.
- [87] PARAPET Deliverable 4.1: PARAPET building blocks documentation. Available via: http://stir.sourceforge.net.
- [88] Trilinear interpolation. Retrieved from https://en.wikipedia.org/wiki/Trilinear\_interpolation.
- [89] Alan V. Oppenheim. *Discrete-time signal processing*. Pearson Education India, 1999.
- [90] C. A. Cocosco, V. Kollokian, R. K. S. Kwan, G. B. Pike, and A. C. Evans. Brainweb: Online interface to a 3D MRI simulated brain database. *NeuroImage*, 1997.
- [91] M. I. Belishev. The Calderon problem for two-dimensional manifolds by the BC-method. *SIAM Journal on Mathematical Analysis*, 35(1):172–182, 2003.

- [92] Jennifer L. Mueller and Samuli Siltanen. The D-bar method for electrical impedance tomography—demystified. *Inverse Problems*, 36(9):093001, 2020.
- [93] S. Ahn and J. A. Fessler. Globally convergent image reconstruction for emission tomography using relaxed ordered subsets algorithms. *IEEE Transactions on Medical Imaging*, 22(5):613–626, 2003.
- [94] Y. Li, A. Kummert, and H. Herzog. Direct Fourier method in 3D PET using accurately determined frequency sample distribution. In *Conference proceedings:... Annual International Conference of the IEEE Engineering in Medicine and Biology Society. IEEE Engineering in Medicine and Biology Society. Annual Conference*, volume 1, pages 3787–3790, 2005.
- [95] B.-W. Schulze, B. Sternin, and V. Shatalov. Structure rings of singularities and differential equations. *Differential Equations, Asymptotic Analysis, and Mathematical Physics*, pages 325–347, 1996.
- [96] K. Yosida. Functional Analysis. Springer-Verlag, Berlin, 1968.
- [97] T. Kato. *Perturbation theory for linear operators*, volume 132. Springer Science & Business Media, 2013.
- [98] J. L. Lions and E. Magenes. *Non-homogeneous boundary value problems and applications: Vol. 1*, volume 181. Springer Science & Business Media, 2012.
- [99] David Gilbarg and Neil S. Trudinger. *Elliptic Partial Differential Equations* of Second Order, volume 224. Springer, 1977.
- [100] Nikolai Nikolaevich Tarkhanov. Harmonic integrals on domains with edges. 2004.
- [101] Martijn Caspers et al. Intuitionistic quantum logic of an n-level system. *Foundations of Physics*, 39(7):731–759, 2009.
- [102] Yu. Egorov and B.-W. Schulze. *Pseudo-Differential Operators, Singularities, Applications*. Birkhäuser, Boston–Basel–Berlin, 1997.

- [103] Nguyen Huu Phuong. FIR FILTER DESIGN: THE WINDOW DESIGN METHOD. Retrieved from http://cnx.org/contents/2YEHwQYh@1/FIR-FILTER-DESIGN-THE-WINDOW-D, n.d.
- [104] L. S. Graham, F. H. Fahey, M. T. Madsen, A. van Aswegen, and M. V. Yester. Quantitation of SPECT performance: report of task group 4, nuclear medicine committee. *Medical physics*, 22(4):401–409, 1995.